Technische Universität München
TUM School of Natural Sciences

Investigation and Engineering of Propagating Spin Waves in Yttrium Iron Garnet Films

Franz M. Vilsmeier

Vollständiger Abdruck der von der TUM School of Natural Sciences der Technischen Universität München zur Erlangung eines Doktors der Naturwissenschaften (Dr. rer. nat.) genehmigten Dissertation.

Vorsitz: Prof. Dr. Johannes Knolle

Prüfende der Dissertation:

1. Prof. Dr. Christian Back
2. Prof. Dr. Rudolf Gross

Die Dissertation wurde am 28.10.2024 bei der Technischen Universität München eingereicht und durch die TUM School of Natural Sciences am 02.12.2024 angenommen.

Abstract

This thesis investigates various aspects of spin wave propagation in 200 nm thick yttrium iron garnet (YIG) films, focusing on both the fundamental characteristics of spin waves and their manipulation.

A key topic is the phenomenon of spin wave caustics, which arise due to anisotropies in the dispersion relation of in-plane magnetized YIG films. These caustics manifest as caustic spin wave beams (CSWBs) within the material. A theoretical model to characterize and classify their properties is established and probed experimentally by Time-Resolved Magneto-Optical Kerr Effect (TR-MOKE) microscopy. The excitation of CSWBs is demonstrated using different excitation approaches, and reasonable agreement between theory and experiment is observed. Additionally, the reflection of CSWBs is investigated, revealing deviations from Snell's law.

The second set of experiments focuses on the hybridization of zeroth-order Damon-Eshbach (DE) modes with first-order perpendicular standing spin waves (PSSWs) in a trapezoidal-shaped magnonic waveguide, also utilizing TR-MOKE microscopy. The findings reveal that the mode hybridization increases spin wave attenuation and, when combined with geometry-induced demagnetizing effects, allows for active control of spin wave propagation distance within the waveguide. Micromagnetic simulations support these experimental observations. Furthermore, all-electrical spin wave spectroscopy, performed with a Vector Network Analyzer (VNA), demonstrates the feasibility of active transmission control between microstrips along the waveguide geometry.

In the final set of experiments, spin wave propagation across a ring-shaped magnonic waveguide is studied using super-Nyquist sampling MOKE (SNS-MOKE) microscopy, a modification of TR-MOKE microscopy. Scattering and complex interference within the ring structure lead to frequency-dependent transmission across the ring in both Backward-Volume and Damon-Eshbach geometries, offering insights into potential bandpass filtering applications.

Kurzfassung

Diese Dissertation untersucht verschiedene Aspekte der Spinwellenausbreitung in 200 nm dicken Yttrium-Eisen-Granat (YIG)-Filmen, wobei der Fokus sowohl auf den grundlegenden Eigenschaften von Spinwellen als auch auf deren Manipulation liegt.

Ein zentrales Thema ist das Phänomen der Spinwellen-Kaustiken, die durch Anisotropien in der Dispersionsrelation von in der Ebene magnetisierten YIG-Filmen entstehen. Diese Kaustiken manifestieren sich als kaustische Spinwellenstrahlen (CSWBs) im Material. Zur Charakterisierung und Klassifizierung ihrer Eigenschaften wird ein theoretisches Modell entwickelt und experimentell mittels zeitaufgelöster magneto-optischer Kerr-Effekt (TR-MOKE) Mikroskopie untersucht. Die Anregung von CSWBs wird durch verschiedene Anregungsmethoden demonstriert, und es zeigt sich eine gute Übereinstimmung zwischen Theorie und Experiment. Zudem wird die Reflexion von CSWBs untersucht, wobei Abweichungen vom Snelliusschen Gesetz festgestellt werden.

Im zweiten Teil der Experimente wird die Hybridisierung von nullter Ordnung Damon-Eshbach (DE)-Moden mit erster Ordnung senkrecht stehenden Spinwellen-Moden (PSSWs) in einem trapezförmigen magnonischen Wellenleiter untersucht, ebenfalls unter Verwendung der TR-MOKE Mikroskopie. Die Ergebnisse zeigen, dass die Moden-Hybridisierung die Dämpfung von Spinwellen erhöht. In Kombination mit geometrieabhängigen Demagnetisierungseffekten wird eine aktive Steuerung der Ausbreitungsdistanz der Spinwellen im Wellenleiter gezeigt. Diese experimentellen Beobachtungen werden durch mikromagnetische Simulationen unterstützt. Darüber hinaus zeigen elektrische Spinwellen-Spektroskopie-Experimente, die mit einem Vektornetzwerkanalysator (VNA) durchgeführt wurden, dass die elektrische Transmission zwischen Mikrostreifen-Antennen entlang des trapezförmigen magnonischen Wellenleiters aktiv kontrolliert werden kann.

Im letzten Experiment wird die Spinwellenausbreitung in einem ringförmigen magnonischen Wellenleiter untersucht, wobei die Super-Nyquist-Sampling MOKE (SNS-MOKE) Mikroskopie, eine Modifikation der TR-MOKE Mikroskopie, angewendet wird. Streuung und komplexe Interferenzen in der Ringstruktur führen zu einer frequenzabhängigen Transmission hinter dem Ring, sowohl in der Backward-Volume- als auch in der Damon-Eshbach-Geometrie. Diese Ergebnisse bieten Einblicke in mögliche Implementierungen magnonischer Elemente als Bandpassfilter.

Contents

Introduction

In recent years, the rapid expansion of machine learning and artificial intelligence technologies has significantly increased the demand for advanced computing and data processing capabilities [1]. As this surge continues, energy consumption is expected to rise substantially, particularly with conventional charge-based processing methods [1]. As a result, there is a growing need to explore alternative low-energy processing solutions. One promising approach is magnonics, a field that has garnered considerable interest and has been the subject of numerous reviews in recent years [1–6].

Magnonics focuses on the study and manipulation of spin waves, which are collective excitations in magnetically ordered materials. The quantum counterpart of these excitations, known as a magnon, obeys Bose-Einstein statistics. The concept of magnons was first introduced by Felix Bloch in 1930, explaining the temperature-dependent magnetization in ferromagnets [7]. Since then, the study of spin waves has steadily evolved with notable contributions by Holstein and Primakoff [8], Dyson [9], Herring and Kittel [10, 11], and Brockhouse [12], leading to the establishment of magnonics as a distinct research field. In magnonics, spin waves serve as the fundamental information carriers with the goal of transmitting, processing, and storing information [4]. With their potential to operate at small wavelengths down to 50 nm [13], and across frequency ranges from GHz to hundreds of THz [6], magnonics offers a powerful and versatile platform to perform various computing and logic operations. Among others, several notable concepts have already been realized, including magnonic crystals [2, 3, 14–18], which exploit periodic structures to create bandgaps in the spin wave spectrum, as well as interference-based logic gates [19–21], non-boolean processing [22], and wave-based neuromorphic computing [23–25].

This thesis investigates various aspects of spin wave propagation in 200 nm thick Yttrium Iron Garnet (YIG) films. YIG is a ferrimagnetic insulator and has emerged as the material of choice within the magnonics community due to its low magnetic damping [6]. The primary experimental tool employed is Time-Resolved Magneto-Optical Kerr Effect (TR-MOKE) microscopy, which allows for detailed observation of spin wave dynamics. Additionally, propagating spin wave spectroscopy is utilized, and micromagnetic simulations often accompany the experiments.

A significant focus of this thesis lies in the fundamental exploration of spin wave caustics, which refer to the focussing of spin waves due to their inherent anisotropic propagation characteristics, leading to the formation of beam-like features [26–46]. These caustic spin wave beams are of particular interest, since they concentrate energy along specific trajectories, resulting in high amplitudes, strong directionality, and steering capabilities. A deeper understanding of the fundamentals of these beams is valuable, as they arise in various contexts and hold promise for future applications [47–49].

Beyond spin wave caustics, this thesis also explores more application-oriented aspects of magnonics. In 200 nm thick YIG films, hybridization effects with higher order perpendicular standing spin wave (PSSW) modes occur. This hybridization, along with geometric considerations and magnetic dipole-induced edge effects, can be leveraged to control spin wave propagation in trapezoidal-shaped magnonic waveguides. Furthermore, the thesis investigates propagation in a ring-shaped magnonic waveguide, which, due to interference effects, is suggested to serve as bandpass filters [50–52].

This thesis is structured into four main parts:

Part I establishes the theoretical and experimental framework for the research. Chapter 1 introduces the fundamental concepts of micromagnetism and the theory of dipole-exchange spin waves. Chapter 2 details the methods employed throughout this thesis, including micromagnetic simulations and the experimental techniques of TR-MOKE and all-electrical broadband spin wave spectroscopy. Chapter 3 theoretically explores the effects of PSSWs on spin wave propagation in full films and magnonic waveguides.

Part II delves into spin wave caustics and caustic spin wave beams in in-plane magnetized magnetic films. To this end, Chapter 4 introduces the concept of spin wave caustics, develops a model, and conducts a systematic theoretical investigation of caustic points and their properties. Chapter 5 outlines the experimental design to investigate caustic spin wave beams, while Chapter 6 discusses the experimental results, which include the general characteristics of caustic spin wave beams, a comparison with the theoretical model, and a detailed examination of their reflection properties.

Part III is dedicated to the experimental evaluation of thickness mode hybridization effects in trapezoidal-shaped magnonic waveguides. Chapter 7 outlines the motivation and experimental design, while Chapter 8 presents the experimental results. This includes demonstrating active control of the spin wave propagation distance and subsequent electrical transmission control between microstrip antennas.

Part IV explores spin wave propagation in a ring-shaped magnonic waveguide, which is proposed as a potential bandpass filter. Chapter 9 motivates this investigation and details the experimental design. Chapter 10 presents the experimental results, focussing on the propagation and filtering characteristics in two magnetic geometries: the Backward-Volume and the Damon-Eshbach configuration.

Part I.

Preliminaries

1. Theory of Dipole-Exchange Spin Waves

Spin waves are collective excitations of magnetic moments within a magnetic material. The quasiparticles corresponding to these excitations are known as magnons. Conceptually, spin waves can be understood as fluctuations of spin propagating through a material, wherein neighboring magnetic moments precess coherently while maintaining a defined phase relation and a defined wave vector $\boldsymbol{k}$. A schematic representation of this situation is sketched in Fig. 1.1. Spin waves are closely related to the phenomenon of ferromagnetic resonance (FMR), which describes the resonant absorption of electromagnetic energy by a ferromagnetic material [53–55]. FMR constitutes itself as uniform precession of magnetic moments; i.e., the special case of a wave with a wave vector magnitude of $k = 0$.

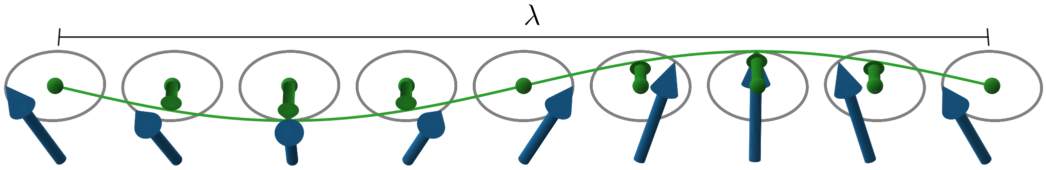

Figure 1.1. Schematic of a spin wave. Neighboring magnetic moments (blue arrows) precess around their equilibrium with a fixed phase lag. The precession amplitude component (depicted in green) changes harmonically with a wavelength λ. Adapted from [56].

The dominant interactions governing spin waves depend on their length scale. In the long-wavelength regime ($k \lesssim 10\,\mu\mathrm{m}^{-1}$), magnetic dipolar interactions are the primary contribution, whereas, in the short-wavelength regime ($k \gtrsim 100\,\mu\mathrm{m}^{-1}$), the exchange interaction becomes dominant. In the intermediate regime, both interactions need to be considered. This regime is referred to as the dipole-exchange regime [56].

Historically, spin waves were first described in 1930 by Bloch in a microscopic model [7]. Landau and Lifshitz developed a macroscopic theory where they formulated an equation of motion for the magnetization, which is represented by a smooth continuous vector field. This approach is referred to as micromagnetism [56, 57]. The Landau Lifshitz equation of motion has been employed for a variety of applications in the field of micromagnetism. Notably, in the long-wavelength limit, it was used to solve for dipolar, or magnetostatic, spin wave modes in confined ferromagnets [58–60].

The primary focus of this thesis is the investigation of spin waves up to the dipole-exchange regime. The subsequent sections aim to provide a comprehensive overview of the fundamental basics of spin waves. The discussions include the concept of micromagnetism, magnetization dynamics, the spin wave dispersion relation $\omega(\boldsymbol{k})$, which defines the relation between the angular frequency ω and the wave vector $\boldsymbol{k}$, and the excitation of spin waves in a magnetic material.

1.1. Micromagnetism

In the field of micromagnetism, the magnetization is described by a smooth continuous vector field $\boldsymbol{M}(\boldsymbol{r},t)$. This field is characterized by length scales much larger than those observed at the atomic scale and exists up to a material-specific critical temperature T_C. It may be defined as the sum of individual magnetic moments $\boldsymbol{\mu}$ per unit volume V:

$$\boldsymbol{M}(\boldsymbol{r},t) = \frac{\sum_V \boldsymbol{\mu}}{V}. \tag{1.1}$$

While quantum mechanics fundamentally governs the existence of magnetic moments and their long-range ordering arising from exchange interaction, the introduction of $\boldsymbol{M}(\boldsymbol{r},t)$ allows for a macroscopic description of the magnetization within a classical framework.

The equilibrium position of the magnetization is then determined by Brown's equation [57]:

$$\boldsymbol{M} \times \boldsymbol{H}_\mathrm{eff} = 0. \tag{1.2}$$

Essentially, the magnetization aligns along an effective field $\boldsymbol{H}_\mathrm{eff}$, which incorporates all the relevant magnetic field contributions. This effective field can be derived by letting the free energy density F vary with respect to $\boldsymbol{M}$ [61]:

$$\boldsymbol{H}_\mathrm{eff} = -\frac{1}{\mu_0}\frac{\delta F}{\delta \boldsymbol{M}}, \tag{1.3}$$

where $\mu_0 = 4\pi \times 10^{-7}\,\mathrm{VsA^{-1}\ m^{-1}}$ denotes the permeability of vacuum.

In this work, three contributions to the free energy density [62] are relevant to the experiments. First, the Zeeman energy density

$$F_\mathrm{Zee} = -\mu_0 \boldsymbol{M} \cdot \boldsymbol{H}_\mathrm{ext} \tag{1.4}$$

describes the effect of an external magnetic field $\boldsymbol{H}_\mathrm{ext}$ on the magnetization, as a collinear orientation is energetically favourable.

The exchange energy density [56, 63]

$$F_\mathrm{ex} = \frac{A}{M_\mathrm{S}^2}\left(\left(\frac{\partial M_x}{\partial x}\right)^2 + \left(\frac{\partial M_y}{\partial y}\right)^2 + \left(\frac{\partial M_z}{\partial z}\right)^2\right) \tag{1.5}$$

describes the tendency of the magnetization to align uniformly. Here, A and M_S correspond to material-specific parameters known as the exchange stiffness constant and the saturation magnetization, respectively.

The final contributor to the free energy density considered is the demagnetizing energy density. For the spin waves studied in this work, this is the dominant contribution, and it is given by:

$$F_\mathrm{dem} = -\frac{1}{2}\mu_0 \boldsymbol{M} \cdot \boldsymbol{H}_\mathrm{dem}. \tag{1.6}$$

Eq. (1.6) arises from long-range magnetic dipole interactions, which depend on the sample geometry and reduce the effective field inside the magnetic material. This will be an important effect in some of the presented experiments. While for ellipsoidal-shaped samples, the demagnetizing field can be expressed as [64, 65]

$$\boldsymbol{H}_{\text{dem}} = -\frac{1}{\mu_0}\mathbb{N}\boldsymbol{M}, \tag{1.7}$$

with the demagnetizing tensor $\mathbb{N}$, calculating $\boldsymbol{H}_{\text{dem}}$ for arbitrary shapes is typically nontrivial. An often-used approximation is based on determining microscopic dipolar fields from individual magnetic moments over a discretized sample geometry. This computation can be performed using software packages such as MUMAX3 [66].

Note that the competition between exchange and demagnetizing energy introduces a characteristic exchange length [64, 67]

$$l_{\text{ex}} = \sqrt{\frac{2A}{\mu_0 M_{\text{S}}^2}}. \tag{1.8}$$

This length scale determines the range over which the exchange interaction becomes dominant, and the magnetization can be assumed to be uniform.

Taking all free energy density contributions into account, Eq. (1.3) defines an effective magnetic field

$$\boldsymbol{H}_{\text{eff}} = \boldsymbol{H}_{\text{ext}} + \boldsymbol{H}_{\text{ex}} + \boldsymbol{H}_{\text{dem}}, \tag{1.9}$$

where

$$\boldsymbol{H}_{\text{ex}} = l_{\text{ex}}^2 \boldsymbol{\nabla}^2 \boldsymbol{M} \tag{1.10}$$

describes the exchange field. While further contributions, such as magneto-crystalline anisotropies or strains, may add to the effective field, these can be disregarded in this context, as they play only a minor role in the experiments.

1.2. Magnetization Dynamics

If the magnetization is not aligned parallel with the effective magnetic field, a torque is exerted on the magnetization causing it to undergo a precessional motion around the effective magnetic field until it reaches equilibrium.

A description of these dynamics is provided by the Landau-Lifshitz-Gilbert (LLG) equation which tracks the temporal and spatial evolution of the magnetization. It is given by [68]

$$\frac{\partial}{\partial t}\boldsymbol{M} = \underbrace{-\gamma\mu_0(\boldsymbol{M}\times\boldsymbol{H}_{\text{eff}})}_{\text{precession}} + \underbrace{\frac{\alpha}{M_{\text{S}}}\left(\boldsymbol{M}\times\frac{\partial \boldsymbol{M}}{\partial t}\right)}_{\text{damping}}. \tag{1.11}$$

where, $\gamma = \left|\frac{ge}{2m_{\text{e}}}\right|$ denotes the gyromagnetic ratio with e, the electron charge, m_{e} the mass of the electron, and g the Landé factor. The dimensionless damping parameter α determines the strength of the dissipation term, which drives the magnetization towards the effective field unless an external stimulus preserves the precession. As equation 1.11 assumes the magnetization to preserve its length, the spiral trajectory of $\boldsymbol{M}$ occurs on a spherical surface. An illustration of the precessional and damping torques is shown in Fig. 1.2.

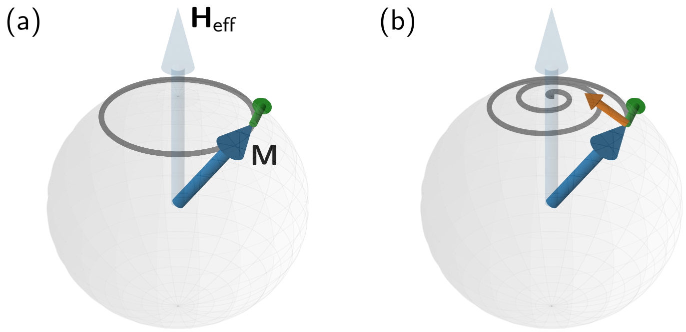

Figure 1.2. Trajectory of the magnetization. (a) The first term of the Landau-Lifshitz-Gilbert (LLG) equation exerts a torque (green arrow) on $\boldsymbol{M}$ (dark blue arrow) which causes a precessional motion of the magnetization around $\boldsymbol{H}_{\text{eff}}$ (light blue arrow). (b) The additional damping torque (orange) drives the magnetization into a spiral motion towards $\boldsymbol{H}_{\text{eff}}$.

The LLG can be solved assuming harmonic time-dependence with angular frequency, $\omega = 2\pi f$. To facilitate this, the magnetization is decomposed into a dynamic part $\boldsymbol{m}(\boldsymbol{r},t) = \boldsymbol{m}_0(\boldsymbol{r})\mathrm{e}^{\mathrm{i}(\omega t)}$ which varies with time and space and a static, uniform part $\boldsymbol{M}_0$. Furthermore, only small deviations around the equilibrium position are assumed, i.e., small precession angles, such that $m \ll M_0$ and $M_0 = M_{\mathrm{S}}$. In a coordinate system aligned with the magnetization (see Fig 1.3), this can be expressed as [56]

$$\boldsymbol{M}(\boldsymbol{r},t) = \boldsymbol{M}_0 + \boldsymbol{m}(\boldsymbol{r},t) = \begin{pmatrix} M_{\mathrm{S}} \\ m_y \\ m_z \end{pmatrix}. \tag{1.12}$$

Analogously, the magnetic field is divided into a static and a dynamic part and can be written as $\boldsymbol{H}_{\text{eff}} = H\boldsymbol{e}_x + h_y\boldsymbol{e}_y + h_z\boldsymbol{e}_z$ [56].

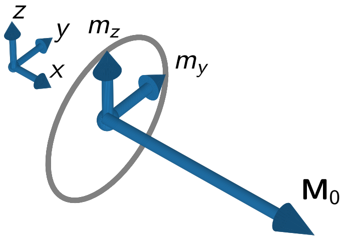

Figure 1.3. Decomposition of magnetization into static part $\boldsymbol{M}_0$ and the dynamic components m_y and m_z. The coordinate system xyz is aligned with the magnetization. Adapted from [56].

Solving the LLG equation 1.11 with the discussed assumptions and only keeping terms linear in $\boldsymbol{m}$ and $\boldsymbol{h}$, yields the so-called linearized LLG equation [56, 69]:

$$\mathrm{i}\omega \begin{pmatrix} m_y \\ m_z \end{pmatrix} = \begin{pmatrix} -\gamma\mu_0(-Hm_z + M_\mathrm{S}h_z) + \mathrm{i}\alpha m_z\omega \\ -\gamma\mu_0(Hm_y + M_\mathrm{S}h_y) + \mathrm{i}\alpha m_y\omega \end{pmatrix}. \tag{1.13}$$

1.3. Spin Wave Dispersion Relation

Spin waves arise as collective low-energy spin excitations that emerge in magnetically ordered materials. As neighboring magnetic moments precess with a finite phase lag, this introduces a spatial component to the magnetization dynamics. The behavior of spin waves is fully characterized by their dispersion relation $\omega(\boldsymbol{k})$, which governs essential properties, including the angular precession frequency ω and the wavelength for a given direction of propagation.

In the following, the dispersion relation in an isotropic ferromagnetic film based on the model established by Kalinikos and Slavin [70] is discussed. In this framework, the coordinate system uvw is introduced where a soft ferromagnetic film is considered which is infinitely extended in the uv-plane and has a finite thickness L along the w-direction. The film is assumed to be magnetized to saturation by a static external magnetic field $\boldsymbol{H}_\mathrm{ext}$ in an arbitrary direction. The v-direction is chosen to coincide with the propagation direction of a spin wave of the form

$$\boldsymbol{m}(v,w,t) = \boldsymbol{m}(w)\mathrm{e}^{\mathrm{i}(\omega t - k_v v)}. \tag{1.14}$$

A sketch of the geometry is shown in Fig. 1.4(a).

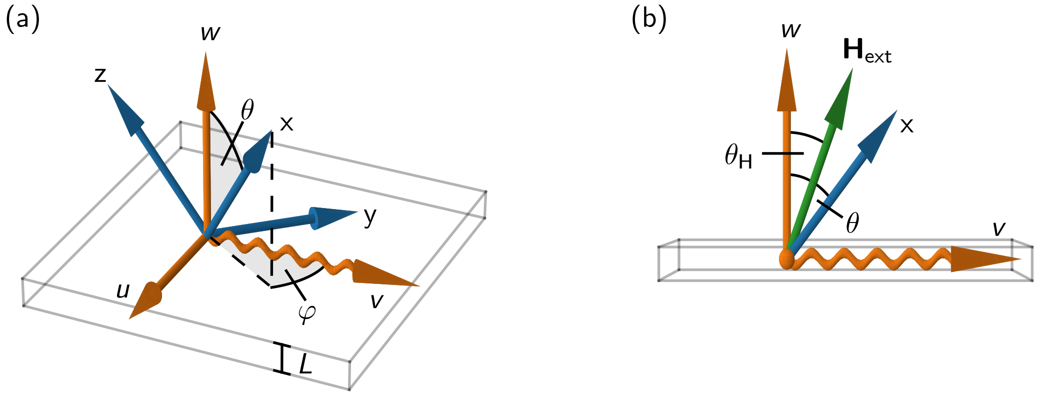

Figure 1.4. Definition of coordinate systems. (a) The angles φ and θ establish a link between the coordinate systems uvw and xyz. The direction of spin wave propagation is chosen to align with the v-axis. The effective field and the equilibrium magnetization are always directed along the x-direction. (b) The external magnetic field forms an angle θ_H with the w-axis.

For convenience, we introduce another coordinate system xyz, which is linked to the laboratory frame uvw via the azimuthal angle φ between v and x, as well as rotation around the u-axis by an angle θ. The xyz-frame is selected such that the internal effective field, $\boldsymbol{H}_{\text{eff}} = H\hat{\boldsymbol{x}}$, and, according to Eq. (1.2), the static equilibrium magnetization are always aligned along the x-axis. For a given external magnetic field strength H_{ext} and direction θ_{H} (see Fig. 1.4(b)), the value for H and the direction θ can be determined by solving Eq. (1.3) for a thin film. This procedure yields the system of equations

$$H = H_{\text{ext}} \cos(\theta - \theta_{\text{H}}) - M_{\text{S}} \cos^2(\theta) \tag{1.15a}$$

$$0 = H_{\text{ext}} \sin(\theta - \theta_{\text{H}}) - M_{\text{S}} \cos(\theta) \sin(\theta). \tag{1.15b}$$

To solve for the spin wave modes and determine the dispersion relation, Kalinikos and Slavin employed mixed surface pinning conditions. Pinning conditions describe how a spin wave behaves at a boundary, establishing the necessary boundary conditions for the spin wave modes [71, 72]. Specifically, totally unpinned surface states refer to the condition where magnetic moments at the surface are free to precess without restriction, while pinned surface states imply that the moments are constrained [73]. In practice, partially pinned states or a mixture of pinning conditions at the top and bottom surface may occur [56, 74]. For thin YIG films, the surface states are often considered to be unpinned [75, 76]. This assumption will be adopted in the following discussions.

Applying zeroth-order perturbation theory, the dispersion relation for dipole-exchange spin waves with totally unpinned surface states is then given by [70]:

$$\omega_n^2 = \left(\omega_{\text{H}} + l_{\text{ex}}^2 k_n^2 \omega_{\text{M}}\right) \left(\omega_{\text{H}} + l_{\text{ex}}^2 k_n^2 \omega_{\text{M}} + \omega_{\text{M}} F_{nn}\right), \tag{1.16}$$

where

$$\omega_{\text{H}} = \gamma \mu_0 H, \tag{1.17}$$

$$\omega_{\text{M}} = \gamma \mu_0 M_{\text{S}}, \tag{1.18}$$

$$F_{nn} = P_{nn} + \sin^2\theta \left(1 - P_{nn}\left(1 + \cos^2\varphi\right) + \omega_{\text{M}} \frac{P_{nn}\left(1 - P_{nn}\right)\sin^2\varphi}{\omega_{\text{H}} + l_{\text{ex}}^2 k_n^2 \omega_{\text{M}}}\right), \tag{1.19}$$

and

$$\begin{aligned} P_{nn} &= \frac{k_v^2}{k_n^2} - \frac{k_v^4}{k_n^4} F_n \frac{1}{1 + \delta_{0n}}, \\ F_n &= \frac{2}{k_v L}\left(1 - (-1)^n \mathrm{e}^{-k_v L}\right). \end{aligned} \tag{1.20}$$

Here, the eigenmode orders $n = 0, 1, 2, \ldots$ refer to the various standing wave patterns that emerge due to confinement across the thickness of the ferromagnetic film. These modes are referred to as perpendicular standing spin waves (PSSW) and arise in addition to the in-plane propagating wave vector. The wavelength of each PSSW mode is quantized according to

$$\lambda_{\text{PSSW}} = \frac{2L}{n}, \tag{1.21}$$

such that $k_n = \sqrt{k_v^2 + \left(\frac{n\pi}{L}\right)^2}$. The influence of higher-order modes on the dispersion relation and spin wave propagation characteristics is examined in more detail in Chapter 3 as they play a crucial role in some of the conducted experiments.

In the subsequent discussion, the dispersion relation will be investigated in the thin film approximation [77], where no amplitude nodes across the film thickness are considered. This simplification disregards higher-order PSSW modes but still provides a sufficiently accurate model for film thicknesses comparable to the exchange length of the magnetic material.

Furthermore, the group velocity $\boldsymbol{v}_{\mathrm{g}}$, i.e., the speed and direction of energy propagation, can be determined from the dispersion relation [78]:

$$\boldsymbol{v}_{\mathrm{g}} = \frac{\partial \omega}{\partial \boldsymbol{k}}. \tag{1.22}$$

This equation implies that, in general, the group velocity and the wave vector may not be collinear. It is also important to note that ω is a complex number when considering damping. The imaginary part $\mathrm{Im}(\omega)$ then introduces a characteristic damping time $\tau = \frac{1}{\mathrm{Im}(\omega)}$. Consequently, an attenuation length for propagating spin waves can be defined as the product of the group velocity and the damping time:

$$L_{\mathrm{att}} = v_{\mathrm{g}} \tau. \tag{1.23}$$

1.3.1. In-Plane Dispersion Relation in the Thin Film Approximation

In the experiments presented in this thesis, the external magnetic field is exclusively chosen such that it lies in the film plane, i.e. $\theta_{\mathrm{H}} = 90°$. In this case $\theta = \theta_{\mathrm{H}} = 90°$, and the internal field simplifies to $H = H_{\mathrm{ext}}$ (cf. Eq. (1.15)).

Considering the thin film approximation, the in-plane dispersion relation can then be expressed in the form [26]

$$\begin{aligned} \omega^2 = \ & \omega_{\mathrm{M}}^2 \left(\frac{\omega_{\mathrm{H}}}{\omega_{\mathrm{M}}} + l_{\mathrm{ex}}^2 k^2 \right) \left(\frac{\omega_{\mathrm{H}}}{\omega_{\mathrm{M}}} + l_{\mathrm{ex}}^2 k^2 + 1 \right) \\ & - \omega_{\mathrm{M}}^2 P(kL) \left(\frac{\omega_{\mathrm{H}}}{\omega_{\mathrm{M}}} + l_{\mathrm{ex}}^2 k^2 + 1 - P(kL) \right) \cos^2(\varphi) \\ & + \omega_{\mathrm{M}}^2 P(kL)(1 - P(kL)), \end{aligned} \tag{1.24}$$

where

$$P(x) = 1 - \frac{1 - e^{-x}}{x}. \tag{1.25}$$

The in-plane dispersion relation exhibits an anisotropic behaviour that depends on the direction of the wave vector. Fig 1.5(a) showcases a contour plot of the dispersion relation for typical YIG material parameters with 200 nm thickness under an applied magnetic field of $\mu_0 H = 20\,\mathrm{mT}$. From hereon forward, typical YIG parameters refer to $M_{\mathrm{S}} = 1.4 \cdot 10^5\,\frac{\mathrm{A}}{\mathrm{m}}$, $A = 3.7 \cdot 10^{-12}\,\frac{\mathrm{J}}{\mathrm{m}}$, $\gamma = 176\,\frac{\mathrm{GHz}}{\mathrm{T}}$. The iso-frequency curves (black contour levels) exhibit pronounced anisotropy at lower frequencies. As the frequency increases, however, they become progressively more isotropic as the exchange regime becomes dominant. The anisotropic behavior will play a critical role in the experiments involving caustic spin wave beams in Part II.

Two primary geometries with a smooth transition between them can be distinguished by varying the angle of the external magnetic field, φ. In the Damon-Eshbach (DE) geometry,

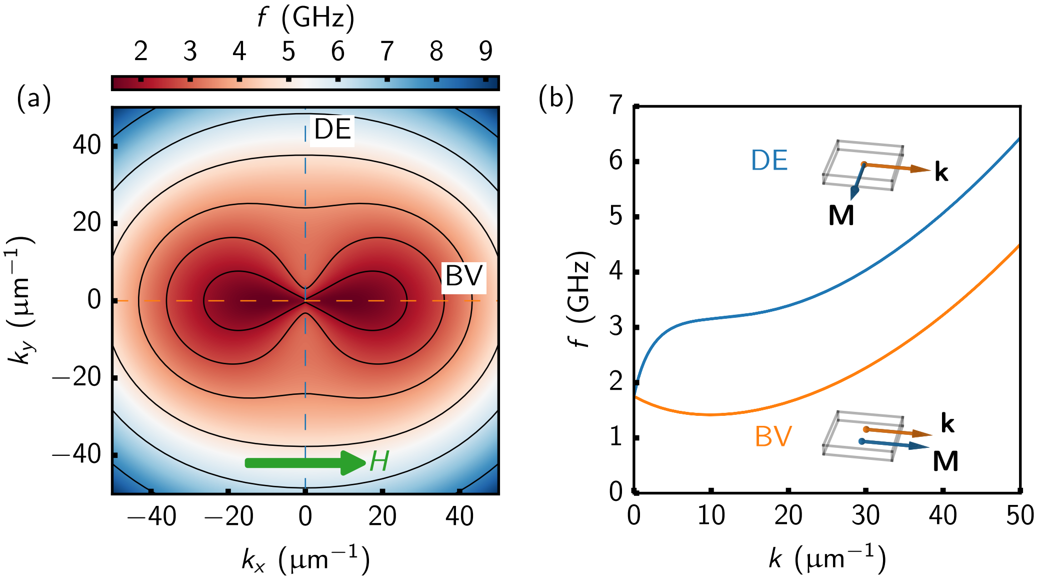

Figure 1.5. Full film dispersion relation with a external magnetic field of $\mu_0 H_{\mathrm{ext}} = 20\,\mathrm{mT}$ applied in the plane of the film. (a) Contour plot of spin wave manifold. The iso-frequency curves (black lines) display anisotropic behavior. (b) Dispersion relations for Damon-Eshbach (DE) and Backward-Volume (BV) spin wave modes. The following parameter values were used in Eq. (1.24): $M_{\mathrm{S}} = 1.4 \cdot 10^5\,\frac{\mathrm{A}}{\mathrm{m}}$, $A_{\mathrm{ex}} = 3.7 \cdot 10^{-12}\,\frac{\mathrm{J}}{\mathrm{m}}$, $\gamma = 176\,\frac{\mathrm{GHz}}{\mathrm{T}}$, $L = 200\,\mathrm{nm}$.

$\boldsymbol{k} \perp \boldsymbol{M}$ ($\varphi = 90°$) holds [59], while the Backward-Volume (BV) geometry is characterized by $\boldsymbol{k} \parallel \boldsymbol{M}$ ($\varphi = 0°$). The dispersion relations for these two modes are shown in Figure 1.5(b). For DE modes, the group velocity and the wave vector are collinear [78]. On the other hand, BV modes can exhibit a negative group velocity in the dipolar regime.

DE spin waves notably exhibit a localization of amplitude at the top or the bottom of the film, depending on the propagation direction, a feature not observed in BV modes. Due to this characteristic, DE modes are also referred to as magnetostatic surface spin waves. The amplitude nonreciprocity stems from the spatial distribution of the dynamic dipolar field induced by the spin wave, and its symmetry can be inverted by reversing the direction of the external magnetic field. For a more in-depth explanation, Refs. [79, 80] are recommended.

In the simplest case, neglecting exchange interactions, the amplitude decays exponentially from the surface of the film, defining a characteristic thickness scale $L_{\mathrm{char}} = 1/k$, over which the amplitude decreases to 1/e if its initial value [73, 79]. It should be noted that when exchange interactions are considered, the modal profile may deviate from this exponential decay [79, 81]. For wavenumbers between $0.5\,\mu\mathrm{m}^{-1}$ and $10\,\mu\mathrm{m}^{-1}$, corresponding to a characteristic thickness ranging from 0.1-2 µm, amplitude non-reciprocity is observed in YIG films of 200 nm thickness. Fig. 1.6 illustrates an example of the modal profile $|m_z|$ of the dynamic out-of-plane component m_z, obtained using the micromagnetic modeling software TETRAX [82] (see Methods Section 2.1.1), for both the DE and BV mode in a 200 nm thick YIG film. The DE mode exhibits a significantly stronger localization near the bottom surface of the film than at the top.

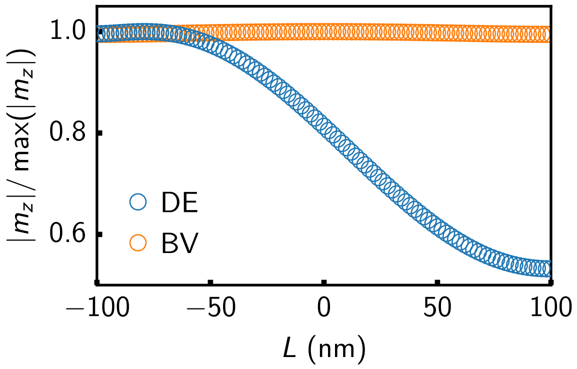

Figure 1.6. Numerically obtained mode profile of the dynamic magnetization component m_z across the film thickness L of DE (blue) and BV (orange) mode in a 200 nm thick YIG film. A magnetic field of $\mu_0 H = 5\,\mathrm{mT}$ field is applied, with $k = 0.9375\,\mu\mathrm{m}^{-1}$ for each mode. The amplitude of the DE mode is more pronounced at the bottom surface of the film.

1.3.2. Out-of-Plane Dispersion Relation in the Thin Film Approximation

In the case where the external magnetic field is applied perpendicular to the film plane, i.e. $\theta_\mathrm{H} = 0°$, the direction of the magnetization is given by $\theta = \theta_\mathrm{H} = 0°$ and the internal magnetic field by $H = H_\mathrm{ext} - M_\mathrm{S}$ (cf. Eq. (1.15)). In this configuration, spin wave propagation can only occur if the external magnetic field overcomes the saturation magnetization of the material.

The dispersion relation for an out-of-plane magnetic field then reads:

$$\omega^2 = \omega_\mathrm{M}^2 \left(\frac{\omega_\mathrm{H}}{\omega_\mathrm{M}} + l_\mathrm{ex}^2 k^2\right)\left(\frac{\omega_\mathrm{H}}{\omega_\mathrm{M}} + l_\mathrm{ex}^2 k^2 + P(kL)\right). \tag{1.26}$$

In contrast to the in-plane dispersion relation, Eq. (1.26) solely depends on the magnitude of the wave vector, not on its direction. As a result, the iso-frequency lines in the contour plot of Fig. 1.7(a) are circular, and spin wave propagation is fully isotropic. The dispersion relation along any of these directions is depicted in Fig. 1.7(b). Spin waves in this configuration are known as Forward-Volume (FV) modes. Notably, the group velocity is always aligned with the wave vector in the FV geometry [78].

1.4. Excitation of Propagating Spin Waves

Up to this point, the discussion has centered on the propagation characteristics of spin waves, without addressing how they are initially generated within magnetic materials. While thermal excitation is always present to some extent, several additional mechanisms are recognized for inducing spin wave emission. These mechanisms include optical pump techniques [83–85], parametric pumping [86–89], emission from spin-transfer-torque and spin-torque nanooscillators [90–95], as well as vortex cores [96] and domain walls [97] serving as spin wave emitters.

The most widely employed approach involves utilizing high-frequency magnetic fields generated by microwave transducers connected to a microwave generator [2, 98–101]. These transducers serve as antennas, typically designed as microstrip lines or shorted coplanar

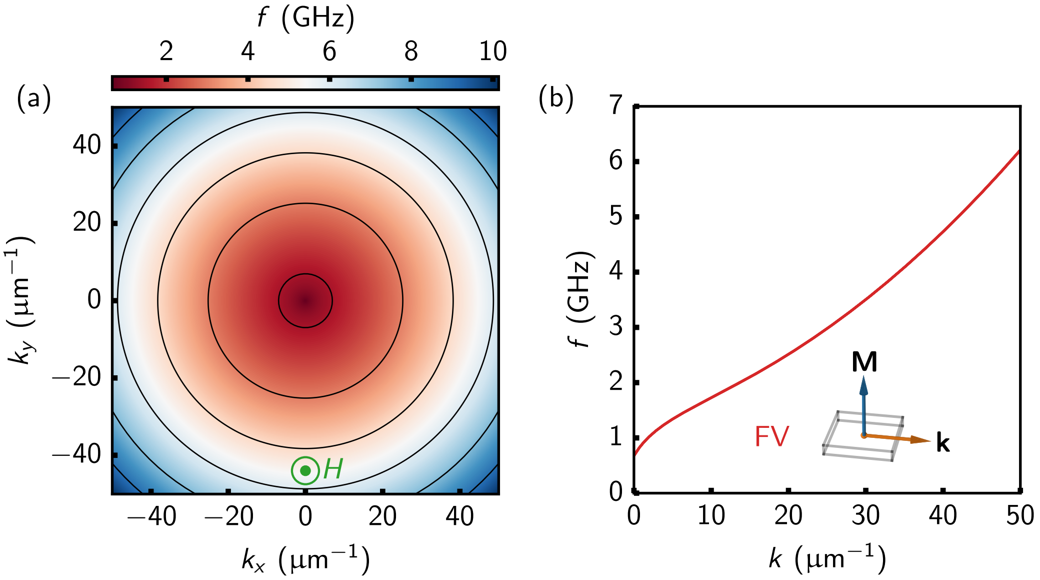

Figure 1.7. Full film dispersion relation with a magnetic field of $\mu_0 H_{\text{ext}} = 200\,\text{mT}$ applied out of the plane of the film. (a) Contour plot of spin wave manifold. Here, the iso-frequency curves (black lines) display isotropic behavior. (b) Dispersion relation of Forward-Volume (FV) mode.

waveguides (CPWs). The current lines generate a spatially inhomogeneous Oersted field that couples inductively to the magnetization [56] and results in spin wavefronts that align approximately parallel to the conductor [102]. Both CPW and microstrip line excitation are employed in the experiments, as illustrated in Fig. 1.8. Similarly, spin waves can be electrically detected using the same process in reverse.

For efficient excitation, two factors have to be considered. On the one hand, the dispersion relation dictates the propagation characteristics in the film at a given frequency and a given effective magnetic field. On the other hand, the excitation efficiency of a wavenumber strongly depends on the dimensions of the transducer lines, as they only efficiently excite spin wavelengths in the order of their size. Only if those two conditions match sufficiently, spin wave propagation can be induced efficiently.

For simplicity, we consider the current lines to be of infinite length and the current distribution to be uniform within the signal and ground lines. Note that, in reality, the current distribution is not uniform and must be determined numerically [103]. Given these assumptions, the induced Oersted field of one current line can be calculated using the two-dimensional Biot-Savart law [56, 64]:

$$\mu_0 \boldsymbol{h}_{\text{ext}} = \frac{1}{2\pi} \frac{\boldsymbol{I} \times \boldsymbol{r}}{r^2}. \tag{1.27}$$

Here, $\boldsymbol{h}_{\text{ext}}$ denotes the excitation field, $\boldsymbol{I}$ the current flowing through one current line, and $\boldsymbol{r}$ the vector from the current element to the observation point.

Figs. 1.9(a) and (c) show the resulting spatial profiles along the propagation direction

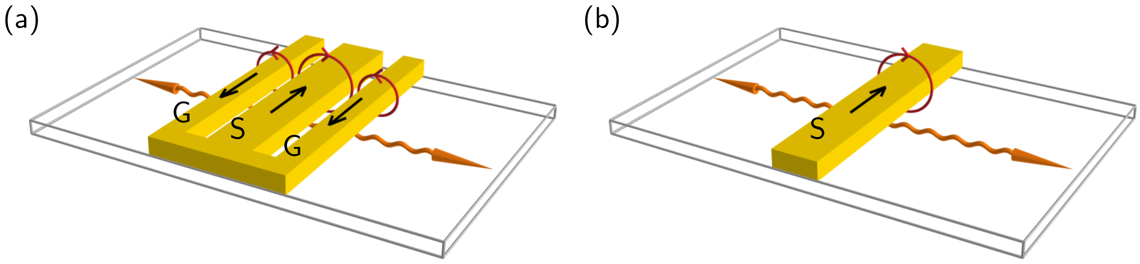

Figure 1.8. Schematic of current line designs and spin wave excitation. (a) Sketch of spin wave excitation by a shorted coplanar waveguide. The waveguide consists of one signal line (S) and two ground lines (G). The microwave current (black arrows) running through the current lines induces an Oersted field (red circles), resulting in the generation of spin waves (orange arrows). (b) Sketch of spin wave excitation by a microstrip. Here, the antenna consists only of one signal line exciting spin wave propagation.

of the in-plane component h_v and the out-of-plane component h_w of the induced Oersted field for a CPW and a microstrip line design. The calculated data shown in Figs. 1.9(a) and (b), related to a CPW, is obtained by superposition of the individual current lines. The wave vectors that the antenna structures can excite in the v-direction are determined through the fast Fourier transform of the in-plane excitation field. Figs 1.9(b) and (d) exhibit the corresponding excitation spectra for different dimensions of CPWs and microstrip. The dimensions of the CPW are given by its signal line width w_{sig}, its ground line width w_{gr} and its gap w_{gap} between the signal and the ground line. The microstrip dimensions are defined solely by their signal line width. It can be seen that a CPW structure allows for a certain wavenumber selectivity, while a microstrip line excites a broader range of wave vectors with strong efficiency at the FMR mode.

Similar principles apply to the excitation of PSSWs. These modes become observable with a nonuniform excitation field along the film thickness [104]. Even though the excitation field decays over much longer lengths in the w-direction compared to the v-direction [56, 105], the inhomogeneity is substantial enough to couple with PSSW modes in a 200 nm thick film.

One final subtlety we want to address is the non-reciprocity in excitation amplitude. It is important to note that this non-reciprocity is distinct from the non-reciprocal surface localization of DE modes; instead, it originates from the geometry of the excitation field with respect to the magnetization. For a more detailed and comprehensive understanding, the article by Devolder [106] is highly recommended.

Due to the antisymmetric out-of-plane component, the helicity of the excitation field depends on the wave vector direction and may enhance or suppress spin wave generation depending on the helicity mismatch with the magnetization precession. The following steps are typically undertaken to derive the helicity mismatch.

First, $\boldsymbol{h}_{\mathrm{ext}}$ is introduced into the LLG equation 1.13 in a suitable coordinate system, which is then recast to the form $\boldsymbol{m} = \boldsymbol{\chi}\boldsymbol{h}_{\mathrm{ext}}$, yielding the susceptibility tensor $\boldsymbol{\chi}$. The excitation

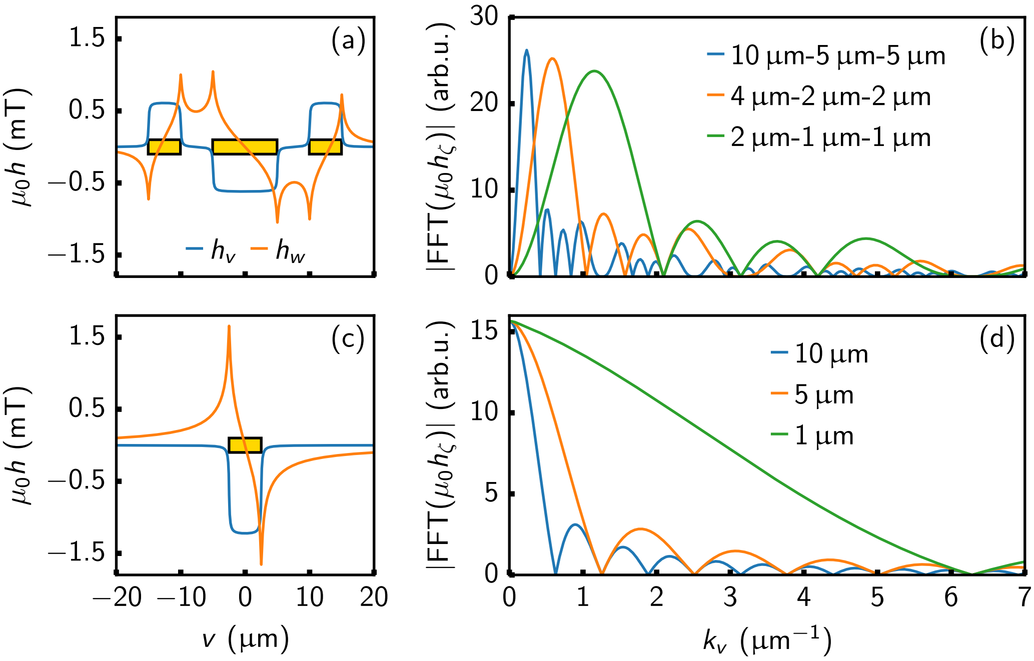

Figure 1.9. Induced Oersted fields and excitation efficiency of current line designs. (a) Spatial profile of in-plane (h_v) and out-of-plane (h_w) components of the Oersted field for a coplanar waveguide (CPW) with $w_{\mathrm{sig}} = 10\,\mu\mathrm{m}$, $w_{\mathrm{gr}} = 5\,\mu\mathrm{m}$ and $w_{\mathrm{gap}} = 5\,\mu\mathrm{m}$. (b) Excitation spectra for different CPW dimensions in the format w_{sig}-w_{gr}-w_{gap}. (c) Spatial profile of in-plane and out-of-plane components of Oersted field for microstrip with $w_{\mathrm{sig}} = 5\,\mu\mathrm{m}$. (d) Excitation spectra for different microstrip widths.

response of the magnetization is given in Fourier space by:

$$\tilde{\boldsymbol{m}} = \tilde{\boldsymbol{\chi}}\tilde{\boldsymbol{h}}_{\mathrm{ext}}, \tag{1.28}$$

where the tilde overscript denotes Fourier space, and $\tilde{\boldsymbol{\chi}}$ represents the complex-valued susceptibility tensor in Fourier space. The tensor $\tilde{\boldsymbol{\chi}}$ can be expressed in the form:

$$\tilde{\boldsymbol{\chi}} = \chi_{\mathrm{max}} \begin{pmatrix} 1 & -\mathrm{i}\epsilon \\ \mathrm{i}\epsilon & 1 \end{pmatrix}, \tag{1.29}$$

where χ_{max} is a constant value and ϵ the precession ellipticity.

Eq. 1.28 can now be solved depending on the static external magnetic field angle to give the magnetization response and is found to depend on the external magnetic field angle as $\sin(\varphi)$. For the condition

$$\sin(\varphi_{\mathrm{MM}}) = -\epsilon\,\mathrm{sgn}(k), \tag{1.30}$$

where sgn denotes the signum function, the response vanishes completely, indicating maximal helicity mismatch.

2. Methods

In the realm of spin waves, various experimental techniques are employed to study their properties and dynamics. Brillouin light scattering (BLS) [107–110] and TR-MOKE microscopy [111–115] have established themselves as standard techniques for magneto-optically probing spin waves, offering both temporal and spatial resolution. In this thesis, TR-MOKE microscopy serves as the primary experimental tool.

BLS, which operates in the frequency domain, relies on the inelastic scattering of photons from spin waves, resulting in the creation or annihilation of magnons. TR-MOKE, on the other hand, operates in the time domain and exploits the Magneto-Optical Kerr Effect (MOKE) to observe magnetization dynamics [116]. Additionally, BLS has the advantage of being able to detect incoherent excitations; however, recording spatial maps is usually very time-consuming. Both techniques are tabletop systems that provide resolution in the dipolar regime.

Higher spatial resolution is offered by time-resolved Scanning Transmission X-ray Microscopy [117–120], which provides magnetic contrast through x-ray magnetic circular dichroism. However, it requires X-rays from a synchrotron source.

In the context of electrical detection, propagating spin wave spectroscopy has emerged as a prominent method [4, 106, 121–125]. This technique is based on inductive coupling between the spin wave stray field and current lines.

Furthermore, experiments are frequently complemented by micromagnetic simulations [66, 82, 126, 127] to validate and better understand the experimental results. Micromagnetic solvers like MUMAX3 [66] are heavily adopted for this purpose. Recently, TETRAX has emerged as another powerful tool for micromagnetic modeling.

This chapter provides an overview of the main simulation and experimental methods used in this thesis. It begins with an overview of the simulation software used, followed by a detailed discussion of the experimental techniques, specifically TR-MOKE microscopy, and all-electrical spin wave spectroscopy.

2.1. Micromagnetic Simulation Software

2.1.1. TetraX

TETRAX is an open-source software package for finite-element method (FEM) micromagnetic modeling of magnetization statics and dynamics [82, 127]. In the FEM approach, the magnetic medium is divided into finite-sized elements, typically of triangular shapes. For each element, the linearized LLG equation 1.13 is formulated, and the system can be solved within a dynamic matrix approach. TETRAX incorporates several FEM dynamic-matrix approaches [69, 128] to numerically calculate normal modes and their associated frequencies for various geometries, including full films, magnonic waveguides with arbitrary cross-section, and nanotubes. A detailed description and verification of the implementation can be found in [82]. TetraX provides detailed analysis tools within a Python environment, particularly through interaction with Jupyter notebooks. Comprehensive documentation and examples are available at `https://tetrax.readthedocs.io`. Within the scope of this thesis, TetraX was mainly used to derive spin wave dispersion relations and mode profiles numerically.

2.1.2. mumax3

mumax3 is an open-source GPU-accelerated software package designed to model space- and time-dependent magnetization dynamics [66]. It employs finite difference discretization of space within a regular grid of orthorhombic cells. The LLG equation is solved on this grid using the Runga-Kutte method for time evolution, assuming that the magnetization is in the center of each cell and considering interactions between cells [56]. The initial static magnetization and effective field can be evaluated by ignoring the precessional term in the LLG equation. A detailed report about the design and verification of mumax3 can be found in [66]. A detailed documentation is provided at `https://mumax.github.io`. This work mainly utilized mumax3 for effective magnetic field calculations and simulated maps of spin wave propagation.

2.2. Time-Resolved Magneto-Optical Kerr Effect Microscopy

In basic MOKE experiments, linearly polarized light is incident on the surface of a magnetic material. Upon reflection, the polarization state is changed. The reflected light then passes through an analyzer, typically a polarizer or Wollaston prism, and is captured by a detector, which then provides a representation of the material's magnetization. Such techniques are widely used for imaging static magnetization and domain walls, as well as measuring hysteresis loops in different magnetization configurations [129–133].

For the study of magnetization dynamics, such as spin waves, TR-MOKE microscopy is widely used [111–115]. TR-MOKE is an optical pump-probe technique. In the presented experiments, spin waves are coherently excited (pumped) by a microwave source with frequency f (cf. Sec. 1.4) and stroboscopically probed by a femtosecond laser pulse train at a repetition rate $f_{\text{rep}} = 80\,\text{MHz}$. Since the laser pulses ($\sim$150 ps) are much shorter than one excitation period, one distinct phase of the dynamic magnetization is probed. The relative phase between the laser pulses and the microwave excitation is kept fixed. Utilizing polar MOKE enables direct access to the dynamic out-of-plane component. In the standard TR-MOKE measurement, this implies that the driving frequency is always an integer multiple of the laser repetition rate. Recent advances, however, have shown to overcome this restriction with a technique framed super-Nyquist sampling MOKE (SNS-MOKE) [134].

In the following, the fundamental aspects of TR-MOKE microscopy are explained. Similar descriptions can be found in [56, 79, 116, 135]. First, the basics of MOKE are introduced, followed by an overview of the experimental setup and the standard measurement principle. Lastly, the concept of SNS-MOKE and its advantages are explored and discussed.

2.2.1. Magneto-Optical Kerr Effect

MOKE describes the change in polarization of light upon reflection from a magnetic material. It is closely related to the Faraday effect, which describes polarization changes during transmission through a magnetic material [56, 64, 65]. When linearly polarized light is incident on a magnetic film, the reflected light exhibits intensity and polarization changes depending on the geometry [79]. Three main geometries are distinguished [64]:

- Polar MOKE: the magnetization is oriented perpendicular to the film surface. It is characterized by a change of rotation of polarization and an ellipticity of the reflected beam. Polar MOKE is suitable to examine samples with an out-of-plane magnetization component.
- Longitudinal MOKE: the magnetization lies in the film plane parallel to the plane of incidence. Here, a rotation of polarization and a slight ellipticity of the reflected beam are observed.
- Transverse MOKE: the magnetization also lies in the film plane but is oriented perpendicular to the plane of incidence. A change of intensity upon reflection is observed.

In the experiments, only polar MOKE is exploited. Here, the change of polarization is directly proportional to the change in the dynamic out-of-plane magnetization component. To be more specific, when the beam is incident perpendicular to the magnetic film plane, only the polar MOKE configuration is accessed, providing sensitivity exclusively to the out-of-plane component of the magnetization dynamics. In other configurations, a mixture of MOKE effects is measured.

At the microscopic level, MOKE arises from spin-orbit interaction [64]. Macroscopically, the MOKE is described by the permittivity tensor $\boldsymbol{\epsilon}$, which represents a material's response to an electric field [56]. In the presence of spin-orbit coupling, for a film with out-of-plane magnetization, the permittivity tensor reads [64]

$$\boldsymbol{\epsilon} = \epsilon_0 \epsilon_\mathrm{r} \begin{pmatrix} 1 & \mathrm{i}Q & 0 \\ -\mathrm{i}Q & 1 & 0 \\ 0 & 0 & 1 \end{pmatrix}, \tag{2.1}$$

where ϵ_0 and ϵ_r are vacuum and relative permittivity, and Q is the magneto-optic parameter, which is a complex material parameter. The off-diagonal tensor entries contribute to the magneto-optic effect, inducing different complex refractive indices for left- and right-handed circularly polarized light [64, 65, 79], i.e.

$$n_\pm \simeq \epsilon_\mathrm{r}^{1/2} \left(1 \pm \frac{1}{2} Q\right). \tag{2.2}$$

Consequently, left- and right-handed circularly polarized light propagates with different velocities and attenuates differently [65]. As a result, linearly polarized light - a superposition of left- and right-handed circularly polarized light - exhibits polarization rotation and ellipticity upon reflection.

2.2.2. Fundamental Components and Concept of Scanning Time-Resolved Kerr Microscopy

Two slightly different configurations of the TR-MOKE setup were employed in the experiments. In one configuration, the sample is exposed to a frequency-doubled femtosecond laser with a center wavelength of 400 nm laser, while in the other configuration, it is exposed to a femtosecond laser with a center wavelength of 800 nm. These configurations differ in spatial resolution, the penetration depth into the magnetic material, and the magneto-optic constants, i.e., the magnitude of polarization rotation by reflection at a magnetic surface. However, since we are primarily interested in an absolute signal, these differences can be somewhat disregarded - although better spatial resolution can be beneficial in certain cases. For simplicity, only the 400 nm case will be discussed further.

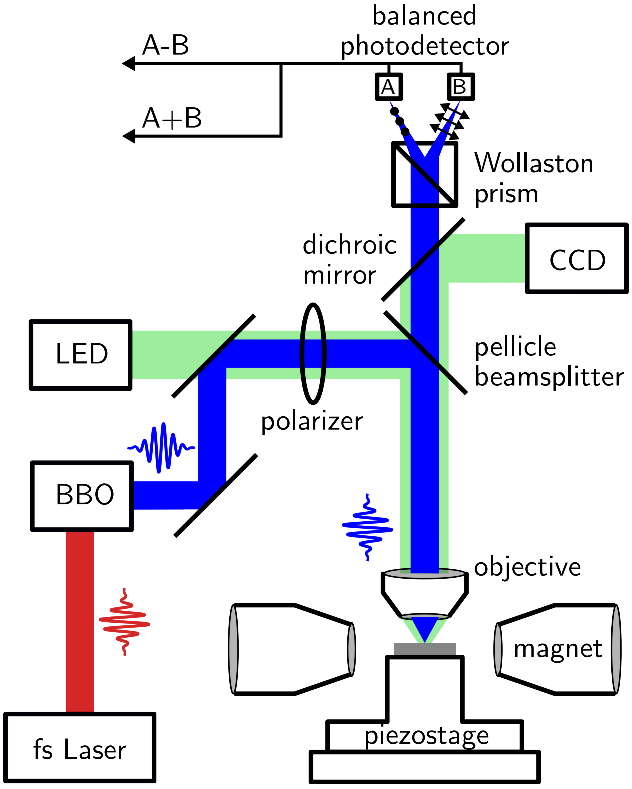

Figure 2.1. Schematic of optical and mechanical components of scanning time-resolved magneto-optical Kerr effect (TR-MOKE) microscopy. The dynamic out-of-plane magnetization component is detected by exploiting the polar MOKE. The sample (grey rectangle) is situated on a piezostage inbetween the two pole shoes of an electromagnet. Further details are provided in the text.

A schematic of the optical and mechanical components of the scanning TR-MOKE is depicted in Fig. 2.1. A mode-locked *Coherent Mira 900* laser system is used as a light source. It provides femtosecond (fs) laser pulses with a repetition rate $f_{\text{rep}} = 80\,\text{MHz}$ at a central wavelength $\lambda_\mathrm{c} \sim 800\,\mathrm{nm}$. The laser wavelength is frequency doubled to $\lambda_\mathrm{c} \sim 400\,\mathrm{nm}$ after passing a nonlinear barium borate crystal. Subsequently, the polarization of the laser light is fixed by a polarizer and reflected towards the sample by an 8:92 (transmission:reflection) pellicle beamsplitter. An objective lens with a numerical aperture of $NA = 0.7$ focuses the laser on the sample, giving a theoretical maximum spatial resolution of $d_\mathrm{res} = \frac{\lambda_\mathrm{c}}{2 \cdot NA} \approx 286\,\mathrm{nm}$. Upon reflection at the magnetic surface, a change of polarization is induced by the polar MOKE, where the magnitude of the polarization rotation is directly proportional to the changes in the dynamic out-of-plane component of the magnetization, i.e., the spin wave amplitude. A Wollaston prism splits the reflected signal into two beams with orthogonal polarization components, which are detected by a balanced photodetector consisting of two photodiodes with photocurrents A and B, respectively. The difference A-B between the photocurrents, generated by the two independent photodiodes, yields a representation of the change in magnetization, the Kerr signal. The sum A+B of the diode signals is proportional to the sample's reflectivity and is usually used to normalize the Kerr signal. Furthermore, the sample is mounted onto a xyz-piezostage. This allows for spatial scans of the relative laser position in the sample plane, giving a 2D map of the Kerr signal and the topography. During the measurement, an external magnetic bias field in the plane of the sample can be applied by means of a rotatable electromagnet.

An additional green LED light source illuminates the sample. It is decoupled from the laser beam path via a dichroic mirror and directed towards a CCD camera, where a real-time wide field microscopic sample image is captured. It is used as a reference to actively stabilize the laser focus and position. This is important to compensate for thermal drifts in a lengthy series of measurements. Between measurements, the piezostage is actively adjusted to align the current CCD image with a reference image [56].

At the core of the TR-MOKE lies the synchronization of the laser pulses with the rf excitation. For this purpose, a *Synchrolock* module is used, which actively stabilizes the laser repetition rate to 80 MHz via a feedback loop consisting of a fast photodiode and an adjustable piezo-controlled mirror inside the laser cavity. Moreover, the internal quartz oscillator of the *Synchrolock* serves as a master clock and provides a 10 MHz reference signal to a *R&S SMA100B* signal generator. This ensures a constant phase relation between laser pulses and rf source but also requires the excitation frequency to be an integer multiple of the repetition rate, i.e., $f = \nu f_\mathrm{rep}$, $\nu \in \mathbb{Z}$.

Lock-in detection is employed to increase the sensitivity of the measurement. For this purpose, the driving rf frequency is frequency-mixed with an additional rectangular kHz signal provided by a low-frequency signal generator. This effectively causes a phase modulation of the rf signal by 180°at the given kHz frequency. After amplification (accounting for mixer conversion losses), the modulated signal is applied to an rf antenna placed atop the sample surface. The Kerr signal from the detector is fed to the lock-in detector and demodulated at the reference frequency given by the low-frequency signal generator. The X-channel of the lock-in [136] gives a signal proportional to the dynamic out-of-plane magnetization component.[1] For a comprehensive overview of the principles of lock-in detection, Ref. [136] is

---

[1] The phase between reference and input signal is chosen such that the entire signal is captured in the X-channel.

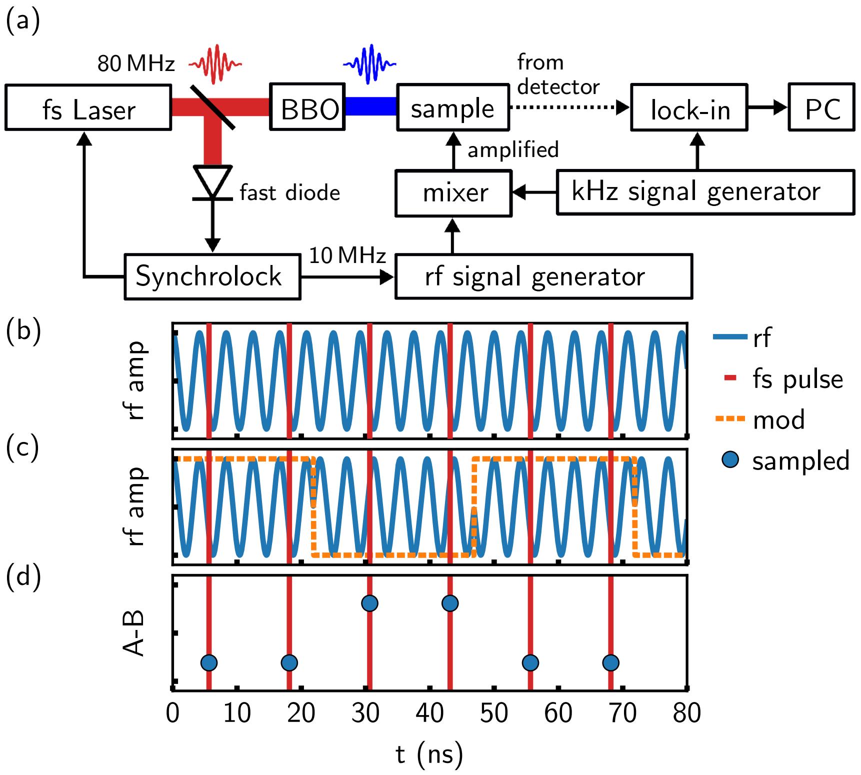

Figure 2.2. Principle of synchronization and modulation. In (a), essential components for synchronization and modulation are depicted. (b) demonstrates the probing of the synchronized rf signal (blue lines) with the laser pulses (red vertical lines). (c) illustrates the kHz modulation signal (orange dashed lines) and the rf signal after the phase modulation, while (d) displays the magnetization values sampled by the laser spot (blue dots) and detected by the lock-in. Adapted from [56].

recommended. An illustration of the synchronization and modulation procedure is given in Fig. 2.2.

It is worth noting that the measured Kerr amplitude doesn't represent the absolute amplitude of spin wave precession. It only reflects the amplitude at the given fixed relative phase between the laser pulses and excitation. To reconstruct the absolute amplitude, an additional out-of-phase measurement 90°shifted to the initial phase needs to be conducted. Taking the square root of the sum of the squares of in-phase and out-of-phase signals yields the absolute signal.

2.2.3. Super-Nyquist Sampling MOKE

A more recent modified version of TR-MOKE microscopy, termed *super-Nyquist sampling* MOKE (SNS-MOKE) or *undersampling*, exploits the effect of aliasing in undersampled signals [21, 134, 137].

When detuning the excitation frequency such that

$$f = \nu f_{\mathrm{rep}} + \epsilon, \tag{2.3}$$

where ν is an integer and ϵ non-zero, lower frequency aliases at integer multiples of ϵ occur in the sampled signal. These aliases preserve signal amplitude and relative phase relation between the laser pulses and the synchronized rf-excitation. Effectively, the dynamic response of the magnetization is down-converted coherently to an alias frequency and can be detected by lock-in demodulation at the frequency ϵ. As a result, SNS-MOKE does not require active modulation of the excitation frequency and permits detection of the dynamic out-of-plane magnetization component at almost arbitrary excitation frequencies. Furthermore, the in-phase and out-of-phase components of the dynamic magnetization are detected in the X- and Y-channel [136] of the lock-in in only one measurement, reducing measurement time by a factor of two. An illustration of the components and the measurement principle is depicted in Fig. 2.3.

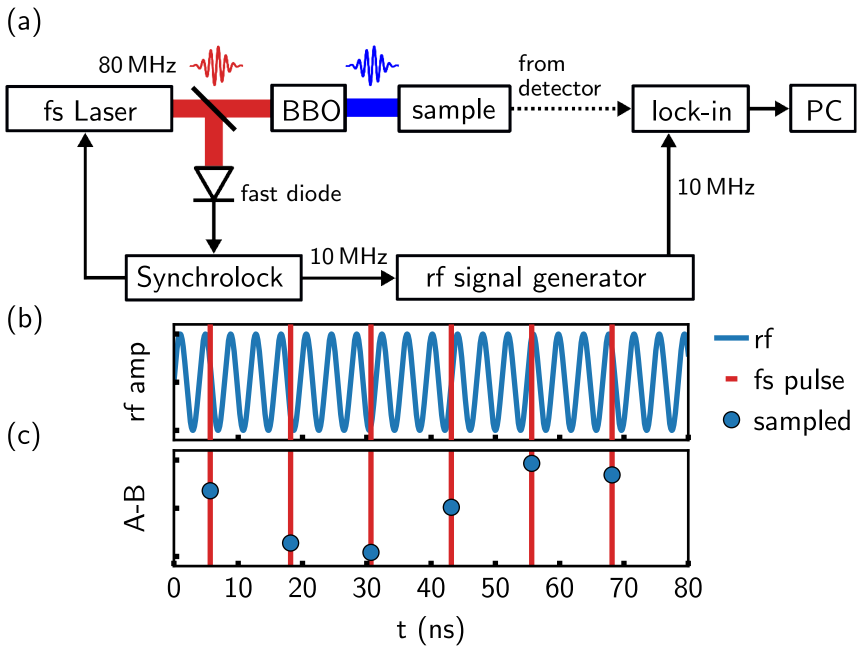

Figure 2.3. Schematic of super-Nyquist sampling MOKE (SNS-MOKE). (a) depicts the necessary components for the SNS technique. Mixer, low-frequency signal generator, and additional amplifier are not required. (b) and (c) illustrate the formation of an alias at lower frequency for an undersampled signal. This alias is detected by the lock-in. Adapted from [56].

During the measurement, the laser pulses, the excitation source for the magnetization dynamics, and the lock-in demodulator must maintain a constant phase relation. However, in our specific case, the sine output level of the 10 MHz reference signal from the *Synchrolock* module is not compatible with the 10 MHz reference input of the *Zurich Instruments HF2LI* lock-in detector.[2] To overcome this issue, the reference output of the synchronized *R&S SMA100B* was utilized instead, as it provides the necessary output level[3] (cf. Fig 2.3(a)). Furthermore, the aliasing band for undersampled signals extends from 0 Hz to half the sampling rate, meaning that signals expressed as in (2.3) can be down-converted to the interval $-f_{\text{rep}}/2 < \epsilon < f_{\text{rep}}/2$[56]. Given a laser repetition rate of 80 MHz, the lock-in and photodiodes should ideally be able to work up to at least 40 MHz. In our experimental configuration, this requirement is satisfied, as the lock-in can demodulate from DC to 50 MHz and the photodetector has a bandwidth of 40 MHz.

2.3. All-Electrical Spin Wave Spectroscopy

In the all-electrical spin wave spectroscopy experiments, two antennas, deposited on top of the magnetic film and connected to separate ports of a Vector Network Analyzer (VNA) with a common ground, are operated in parallel. One antenna acts as the excitation source, while the other serves to detect the electrical signal induced by the spin waves (cf. Chapter 1.4) [106, 121–125]. The VNA injects an rf signal into the outgoing port j and detects the magnitude and phase of the response in port k. The output of the VNA is quantified in terms of a scattering matrix S_{jk} with

$$S_{jk} = \frac{V_j^{\text{in}}}{V_k^{\text{out}}} = \frac{|V_j^{\text{in}}|}{|V_k^{\text{out}}|} \cdot e^{i\Delta\phi}, \qquad j,k \in \{1,2\}. \tag{2.4}$$

The diagonal scattering parameters S_{11} and S_{22} represent the reflection of the signal at the corresponding port, while S_{21} and S_{12} describe the transmission from port 1 to port 2 and vice versa. Fig 2.4 shows an illustration of the measurement technique.

Two different modes of operation are employed for the spin wave spectroscopy experiments presented in this work. In the broadband spin wave spectroscopy measurements, the external magnetic field is set to a fixed value, and the VNA sweeps the frequency of the outgoing port across a specified range. However, a frequency-dependent background occurs in the detected scattering parameters due to direct antenna-to-antenna coupling. To improve contrast, a high-field subtraction method is applied. Additional reference data $S_{jk,\text{ref}}$ is recorded at high external magnetic field, and the obtained absolute values of the reference data are subtracted from the absolute values of the scattering parameters at the field of interest. The spectra are then presented in terms of the processed data, i.e., $|\Delta S_{jk}| = |S_{jk}| - |S_{jk,\text{ref}}|$. The second mode of operation is the continuous wave (CW) mode. Here, the VNA frequency remains fixed for a chosen measurement time while the external magnetic field is swept. It provides less noisy data by increasing the number of statistical samples, and no reference data is recorded.

---

[2] The *Zurich Instruments HF2LI* Clock-In requires a signal of at least 2 V_{pp}.

[3] 14 dBm (3.17 V_{pp}) sinusoidal output.

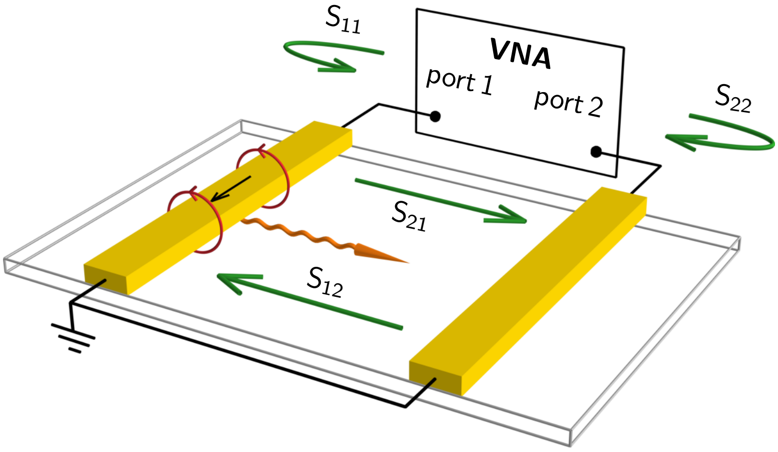

Figure 2.4. Schematic of all-electrical spin wave spectroscopy. One antenna operates as the excitation source, while the other detects electrical response induced by the propagating spin waves. The vector network analyzer (VNA) can detect the reflection parameters S_{11} and S_{22} and the transmission parameters S_{21} and S_{12}.

3. Effect of Hybridization of PSSW Modes on Spin Wave Propagation

When the magnetic film thickness increases, the first-order perturbation theory by Kalinikos and Slavin (KS) given in Eq. (1.16) becomes less reliable. In such cases, it becomes necessary to account for PSSWs to accurately capture spin wave propagation. This chapter discusses the effect of PSSWs on spin wave propagation in more detail on the basis of micromagnetic simulations. Note that while higher perturbation orders in the KS model address these effects as well, they require significantly more computation time [34]. Understanding the resulting phenomena is essential for the experiments presented within the scope of this thesis, particularly in Part III. The chapter begins by exploring the fundamental principles in a full film and then extends the discussion to magnonic waveguides of finite width.

3.1. Full Film Considerations

Using Eq. (1.16) by Kalinikos and Slavin (KS) [70], the full film dispersion relations of the first three eigenmodes in the totally unpinned case are derived in zeroth-order perturbation theory. Fig. 3.1(a) shows the results in the DE ($\varphi = 90°$, cf. Fig. 1.5) and BV ($\varphi = 0°$, cf. Fig. 1.5) geometry for a 200 nm thick YIG film with an external magnetic field of $\mu_0 H = 32\,\mathrm{mT}$, along with the corresponding thickness profiles. It can be observed that the $n = 0$ DE mode and the $n = 1$ PSSW mode intersect in the dipolar regime in the DE geometry, while no mode crossing occurs in the BV geometry.

In this context, it should be pointed out that higher-order PSSWs ($n \geq 1$) in the DE geometry lack surface character and are technically not DE modes but exhibit volume character [60]. For simplicity, however, these modes will be referred to as higher-order PSSW modes in the DE geometry.

Fig 3.1(b) compares the analytic solutions to micromagnetic simulations of the $n = 0$ and the $n = 1$ modes in the DE geometry utilizing TetraX [82]. Going above the dipolar regime, the analytical solution tends to overestimate the frequency compared to the micromagnetic solution. A key feature in the micromagnetic simulations is the lifting of the wavenumber degeneracy at the points of mode intersection, resulting in the formation of an anticrossing for the $n = 0$ DE mode and the $n = 1$ PSSW mode. This is particularly visible in the zoomed inset of Fig. 3.1(b).

This avoided crossing is a result of the interaction between the two modes, leading to a dipole-dipole hybridization of the dispersion branches [70]. In this region, the dispersion relation is flattened, and thus, the group velocity for propagating spin waves approaches zero (cf. Eq. (1.22)) [34]. As a result, the attenuation length of spin wave propagation is

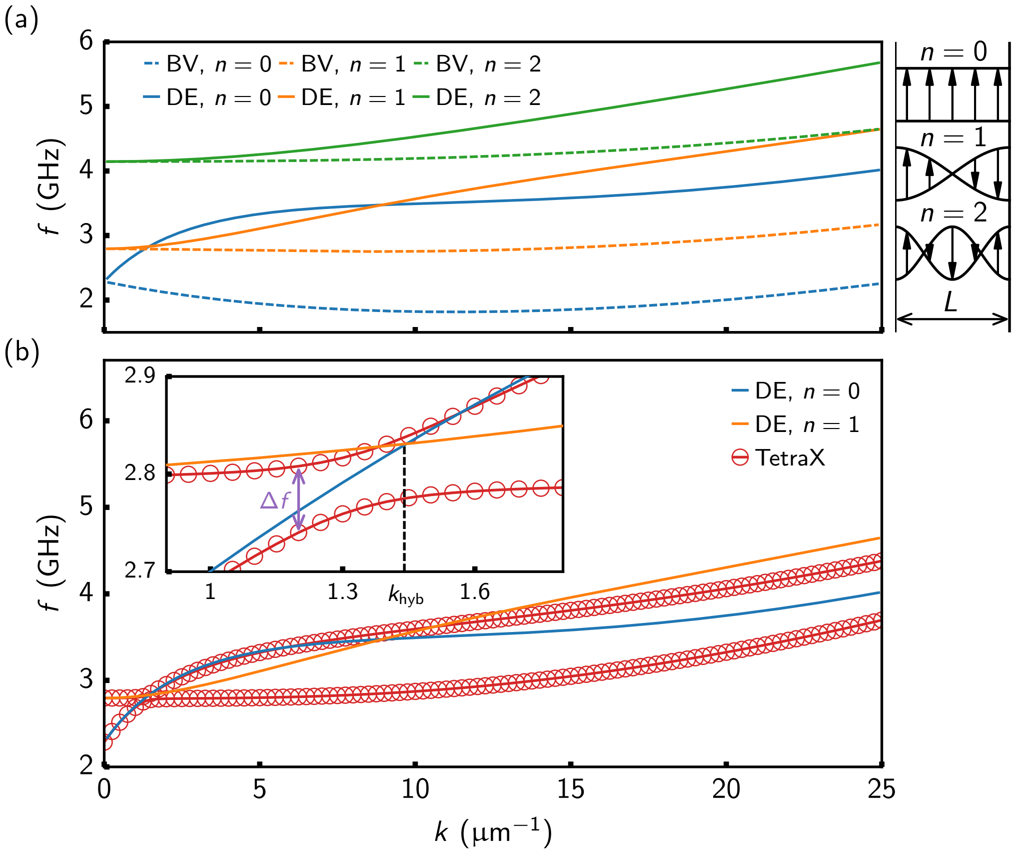

Figure 3.1. Dispersion relation considering PSSWs in 200 nm YIG with an external magnetic field of $\mu_0 H = 32\,\mathrm{mT}$. (a) shows the solutions from the zeroth-order perturbation model by Kalinikos and Slavin (KS) along with the corresponding thickness profiles. The spin wave modes in the DE geometry cross each other. In (b), the KS model for $n = 0$ and $n = 1$ is compared to micromagnetic solutions by TetraX. An avoided crossing occurs, particularly visible in the zoomed inset. Δf (purple arrow) gives a measure for the strength of the hybridization. k_{hyb} denotes the degenerate wavenumber.

considerably reduced (cf. Eq. (1.23)), giving rise to a spin wave stop band where spin wave propagation is effectively suppressed [34]. Note that the avoided crossing with higher-order PSSWs occurs only in the dipolar regime.

In the following, some characteristics of the anticrossing in full YIG films in the DE geometry are discussed in more detail. To this end, the quantity Δf is introduced as the minimal gap between the upper and lower band determined by TetraX simulations. Δf serves as a qualitative measure of the coupling strength between the modes. Additionally, the wave vector of hybridization k_{hyb} is introduced as the intercept of the $n = 0$ and $n = 1$ modes derived from the KS zeroth-order perturbation model. The quantities Δf and k_{hyb} are illustrated in the inset of Fig. 3.1(a).

Fig. 3.2 displays the position and extent of Δf (marked with orange) for a 200 nm thick YIG film under several external magnetic field values in the DE geometry. Essentially, this figure serves as a phase map, showcasing the conditions under which propagation is suppressed due to the hybridization. As the external magnetic field increases, the hybridization condition shifts towards higher frequencies, and the stop band slightly broadens. The slight discontinuities in the stop band (e.g., at 2.1 GHz, 13 mT) are attributed to the limited k resolution of the numerically determined dispersion relation.

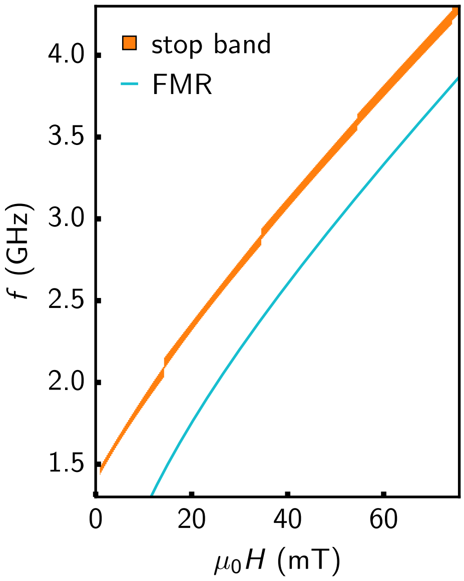

Figure 3.2. Frequency and field map showing the evolution of the spin wave stop band condition in the DE configuration for a 200 nm thick YIG film, computed by TetraX. The orange band highlights the conditions where the anticrossing occurs. The cyan-colored line depicts the FMR condition for comparison.

Given the significant influence of film thickness on the hybridization of PSSW modes, a brief discussion on this is provided in the following. Fig 3.3 shows the relationship between film thickness and both Δf and k_{hyb} at an external magnetic field of $\mu_0 H$ =32 mT. As film thickness decreases, both parameters exhibit an increasing trend. Notably, below a thickness of approximately 170 nm the dispersion branches no longer intersect. As the film thickness decreases, the mode spacing of the $n > 0$ modes increases, and the slope of the $n = 0$ mode decreases, leading to a critical thickness beyond which hybridization ceases to occur [70].

Fig 3.3(b) explores the dependence of k_{hyb} on the external magnetic field for various film thicknesses at a frequency of 2.8 GHz. Higher external magnetic field values correspond to increased k_{hyb}. Moreover, the external magnetic field also influences the existence of hybridization. A high external magnetic field flattens the $n = 0$ mode in the dipolar regime, and hence, the dispersion branches no longer cross each other. For example, with a 170 nm thick film, this occurs above magnetic fields of approximately 50 mT. In summary, this discussion demonstrates that the properties of the spin wave stop band can be tuned to some extent by adjusting the external magnetic field strength, the frequency, and the film thickness.

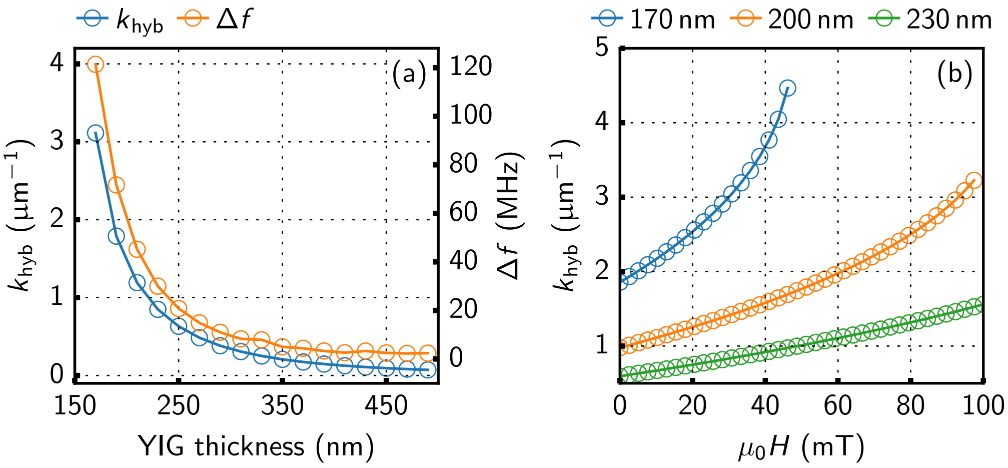

Figure 3.3. Some properties of hybridization characteristics. (a) Dependence of k_{hyb} and Δf on film thickness at an external magnetic field of 32 mT. Both parameters tend to decrease with increasing thickness. (b) Dependence of k_{hyb} on external magnetic field strength at a frequency of 2.8 GHz. k_{hyb} can be tuned within a specific range by changing the external magnetic field strength.

3.2. Effect of Waveguide Width on Hybridization

In a spin wave waveguide with finite width w_0, as sketched in Fig. 3.4(a), an additional quantization across the waveguide width occurs. The corresponding dispersion relation can be represented using Eq. (1.16) by letting $k_{\mathrm{v}} \mapsto \sqrt{k_{\mathrm{v}}^2 + \left(\frac{m\pi}{w_0}\right)^2}$ and $\varphi \mapsto \varphi - \arctan\left(\frac{m\pi}{k_{\mathrm{v}} w_0}\right)$ [138–140]. Here, $m = 0, 1, 2, ...$ represent the eigenmode orders across the width of the waveguide, and k_{v} denotes the wavenumber along the waveguide.

In a transversely magnetized waveguide in the DE-geometry ($\mathbf{k} \perp \mathbf{M}$), demagnetization effects become significant. Because of this, the non-uniform effective field $\mu_0 H_{\mathrm{eff}}$ needs to be considered in the dispersion relation in place of the externally applied magnetic field. Fig. 3.4(b) illustrates the effective magnetic field in x-direction, $\mu_0 H_{x,\mathrm{eff}}$, across a waveguide with a width of $w_0 = 6\,\mu\mathrm{m}$ under an applied magnetic field of $\mu_0 H = 32\,\mathrm{mT}$. While spin wave propagation in the center of the waveguide may assume a uniform field, at the edges, a strong reduction in the effective magnetic field occurs. To account for this strong reduction, an effective waveguide width w_{eff} is introduced in place of w_0. Various definitions exist for w_{eff} [89, 140]; here, we adopt the definition by Chumak [140]. According to this definition, w_{eff} is given by the distance of points across the width where the effective field is reduced by 10%. i.e., to the value $0.9 \cdot \mu_0 H_{\mathrm{eff}}^{\mathrm{max}}$.

To further quantify the effective field in the waveguide center and its effective width, micromagnetic simulations [66] were conducted on transversely magnetized waveguides under an external magnetic field of $\mu_0 H = 32\,\mathrm{mT}$. Figs. 3.5(a)-(b) illustrate the x-component of the effective field in the center and the ratio w_{eff}/w_0 as a function of waveguide width. The

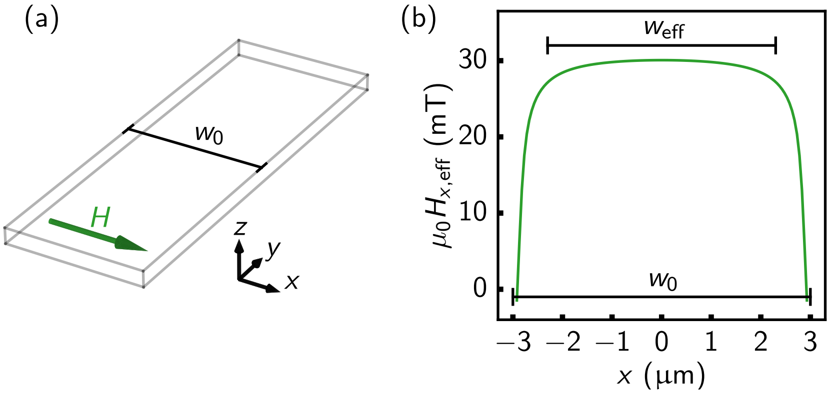

Figure 3.4. (a) Sketch of a magnonic waveguide with finite width w_0. (b) Effective magnetic field along the x-direction in a transversely magnetized magnonic waveguide with $w_0 = 6\,\mu\text{m}$ and $\mu_0 H = 32\,\text{mT}$. The difference between the actual waveguide width w_0 and the effective width w_{eff} is illustrated.

effective field exhibits a gradual decrease, showing reductions of up to 3 mT compared to the external magnetic field. The effective width is maximally reduced to about 65% of the actual waveguide width, permitting a rather broad region across the width of mostly uniform field and mode propagation.

In Fig. 3.5(c), the resulting analytical dispersion relations for several thickness ($n = 0$, $n = 1$) and width modes ($m = 0$, $m = 1$, $m = 2$) with $w_0 = 6\,\mu\text{m}$ are plotted along with the corresponding full film dispersion. In general, the reduced effective field causes a shift of the dispersion relation towards lower frequencies compared to the full film. Moreover, with increasing order of the width mode ($m = 1$, $m = 2$), the reduction in frequency in the dipolar regime becomes more pronounced. More notably, however, the $n = 0$ and $n = 1$ PSSW modes still intersect in the dipolar regime in the waveguide dispersion relations, facilitating a mode hybridization and corresponding stop band. Furthermore, as shown in Fig. 3.5(d), the finite waveguide width doesn't notably affect the higher-order PSSW ($n = 1$) aside from the reduction in the effective magnetic field.

Thus, it is concluded that the dominant effect of the width modulation on the hybridization is the reduced effective field and the resulting shift in the hybridization condition. This is especially the case for the $m = 0$ width mode, which should be the dominant mode in the experiments in Part III. In this Part, plane waves transitioning from the full film into a tapered waveguide geometry are investigated.

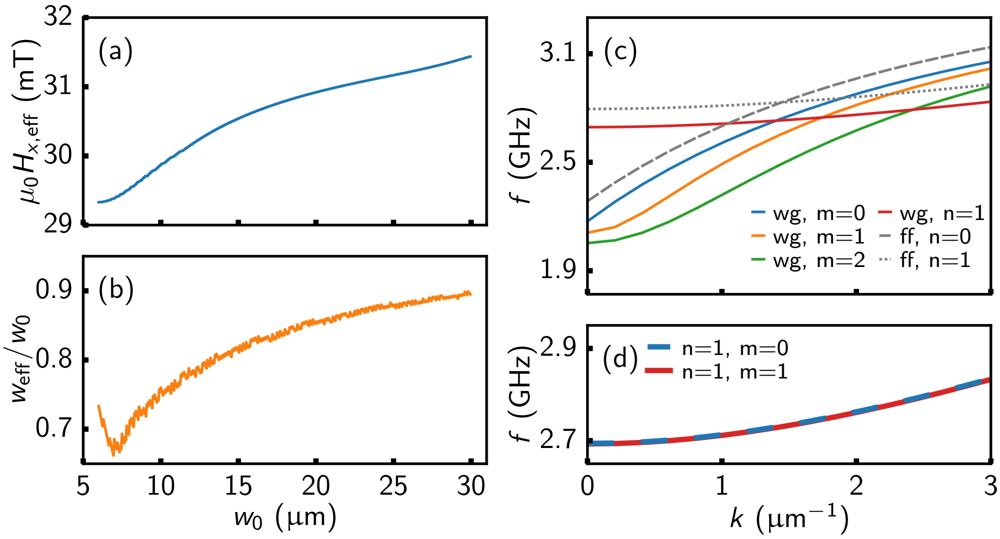

Figure 3.5. Effect of waveguide width on the dispersion relation. (a) x-component of the effective field in the center as a function of waveguide width w_0. (b) Ratio of effective width w_{eff} and actual width w_0. (c) Analytical dispersion relations of waveguide (wg) modes for $w = 6\,\mu\mathrm{m}$. Modes with $n = 0$ and $m = 0$ (blue), $n = 0$ and $m = 1$ (orange), $n = 0$ and $m = 2$ (green), and $n = 1$ and $m = 0$ (red) are depicted. For comparison, the full film (ff) modes with $n = 0$ and $n = 1$ are also shown. (d) Width modes with $n = 1$ and $m = 0$, and $n = 1$ and $m = 1$. The width mode has no significant impact on the higher-order PSSW.

Part II.

Caustic Spin Wave Beams

Many of the discussions and findings in this part are published in [26].

4. Model of Caustic Spin Wave Beams

In wave propagation, caustics refer to localized curves or patterns characterized by a significant increase in wave amplitude compared to their surroundings [26, 141]. The observation of caustic phenomena spans multiple fields, including optics and acoustics [141], dark matter physics [142, 143], and condensed matter physics [144–150]. Geometrically, caustics arise when rays intersect on a set of points, which can take the form of a single point, a line, or a surface.

In various wave fields, like optics and acoustics, caustic patterns emerge due to the presence of inhomogeneities in the media, affecting the processes of refraction and reflection [141, 151]. For instance, a cusp-like caustic pattern may form when rays are reflected on a curved surface, as illustrated in Fig 4.1.

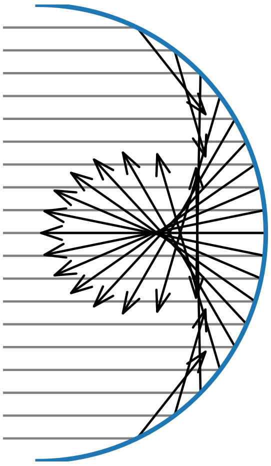

Figure 4.1. Formation of a caustic pattern. After reflection from the curved surface (similar to a coffee cup), rays intersect on a defined set of points in space, forming a local cusp-like pattern of higher intensity.

In thin ferromagnetic films[1], the formation of spin wave caustics is inherently different. Instead of arising from inhomogeneities within the film, spin wave caustics stem from anisotropies in the dispersion relation [26, 37]. These anisotropies can give rise to a stationary group velocity and, consequently, a fixed direction of energy flux around certain wave vectors [37]. As a result, well-defined propagation directions with enhanced amplitudes can manifest within the film [26]. Such beams will be referred to as caustic spin wave beams (CSWB) from this point forward.

In the context of phonons, the phenomenon of caustics arising from anisotropic propagation - referred to as ”focussing” - has been observed since 1969 [144, 145, 152–154]. In contrast,

---

[1] Where the film thickness is comparable to the exchange length of the magnetic material.

the discovery of caustics in thin ferromagnetic films was first reported approximately 20 years later [37]. Since then, multiple investigations have explored the facets of caustics in ferromagnetic films [27–36, 38–46].

Among others, these studies include caustic beams at the transitions from a magnetic waveguide to the full film [36, 43, 44], caustic beam emission from an antidot [27], caustic beams resulting from the collapse of spin wave bullets [45], the radiation of caustic waves from edge modes [46], all optical-excitation of caustic beams [32] and caustic-like emission at a 1D diffraction grating [34–36]. Recent advances have also demonstrated the shaping of caustic beams embedded within a near-field diffraction model [39, 155]. Other noteworthy contributions suggest unidirectional caustic beams induced by the distortion of the iso-frequency curve due to Dzyaloshinskii–Moriya interaction (DMI) [28, 38], and caustics due to dipole-dipole interactions in synthetic antiferromagnets [33]. Moreover, magnonic logic networks have been proposed [47, 48] and demonstrated [49], showing promise in leveraging the enhanced local amplitude and steering properties of CSWBs for computation.

Despite these advances, a systematic investigation of caustics and their properties in the context of thin magnetic films has been lacking, which could prove important for comprehending their potential applications. In the following sections, a comprehensive overview of the fundamental aspects of CSWBs is provided, followed by a systematic theoretical and experimental investigation of their properties.

4.1. General Considerations

Since the formation of caustics stems from anisotropy in the propagation characteristics, the subsequent discussion is focused solely on a thin film magnetized in the plane. In this configuration, the iso-frequency curves exhibit significant anisotropy. In contrast, the dispersion relation in the FV-geometry is fully isotropic (cf. Fig. 1.7), lacking the presence of spin wave caustics.

We examine the thin film dispersion relation given by Eq. (1.24), where an external magnetic field is applied in the film plane. At a given frequency, a fixed external magnetic field, and a given film thickness, the solution to Eq. (1.24) is the possibly empty set of accessible wave vectors $\boldsymbol{k}$ [26]. Under the constraint of fields below the FMR field, the dispersion relation always provides a non-empty solution. The corresponding iso-frequency curve then governs the properties of the spin waves, which are allowed to propagate under the given conditions. It is worth noting that in the literature, the iso-frequency curve is sometimes also referred to as the slowness curve [28, 45]. This is owed to the fact that k is proportional to the so-called slowness $\frac{1}{v_\mathrm{p}}$, where v_p denotes the phase velocity of propagating spin waves. Due to the symmetry of the cosine in the dispersion relation, it suffices to restrict the analysis to the quadrant $\varphi \in [0, \pi/2]$ as the remaining quadrants can be derived using mirror symmetry operations.

Fig. 4.2 depicts an exemplary iso-frequency curve for a typical YIG sample. Each point on this curve is characterized by a wave vector $\boldsymbol{k}$ with corresponding wavefront angle φ. Furthermore, since the group velocity is defined as the frequency gradient $\frac{\partial\omega}{\partial\boldsymbol{k}}$ (cf. Eq. (1.22)), it follows that $\boldsymbol{v}_\mathrm{g}$ is always perpendicular to the iso-frequency curve for any given $\boldsymbol{k}$. In this

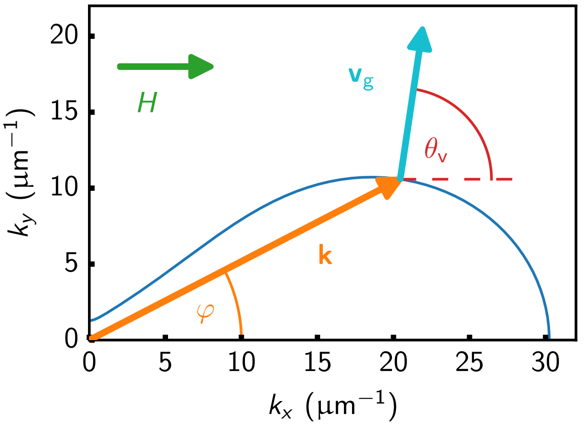

Figure 4.2. Iso-frequency curve for 200 nm YIG at $f = 2\,\text{GHz}$, $\mu_0 H = 10\,\text{mT}$. Any allowed propagating spin wave on the iso-frequency curve can be characterized by its wave vector $\boldsymbol{k}$ (orange arrow), its wavefront angle φ (orange), its group velocity $\boldsymbol{v}_\text{g}$ (cyan arrow), and its group velocity direction θ_V (red). H (green arrow) denotes the direction of the external magnetic field. Clearly, the wavefront angle and the group velocity direction are non-collinear.

context, we introduce θ_v as the angle between the group velocity and the external magnetic field. These geometric quantities will be of significance for our analysis. We further emphasize that phase and group velocity are not necessarily collinear; in fact, φ and θ_v may diverge significantly. Moreover, a small change in wave vector can result in a considerable change in group velocity direction.

4.2. Features of Spin Wave Caustics

The presence of anisotropy in the iso-frequency curve allows specific wave vectors to have a stationary group velocity, meaning that the group velocities around these wave vectors point in the same direction. Such a scenario on the iso-frequency curve is illustrated in Fig. 4.3 where several group velocities across the iso-frequency curve are depicted. This stationary group velocity results in a localized and enhanced energy density along a specific direction,

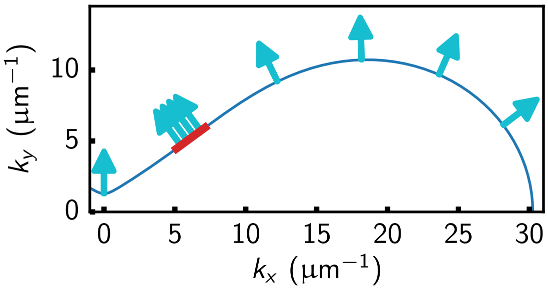

Figure 4.3. Group velocity directions (cyan-colored arrows) along an exemplary iso-frequency curve (blue curve). Within the red section of the iso-frequency curve, the group velocities point in the same direction.

which manifests in the formation of a caustic beam. The caustic beam consists of a range of wave vectors clustered around a carrier and exhibits a well-defined propagation direction [26, 37].

To identify caustic beams, the focus essentially lies in locating the local extrema of the group velocity direction, or in other words, undulation points on the iso-frequency curve. Consequently, the following condition must be satisfied for a caustic point k_c to exist:

$$\left.\frac{d\theta_\mathrm{v}}{dk}\right|_{k_\mathrm{c}} = 0. \tag{4.1}$$

The CSWB is then characterized by its carrier wavenumber k_c, its corresponding wavefront angle φ_c, and its beam direction $\theta_{\mathrm{v,c}}$. An exemplary schematic of a caustic beam profile emerging from a caustic point is illustrated in Fig. 4.4. Note that in reality, the beam also diverges depending on the position of the caustic point on the iso-frequency curve and the contributing group velocity directions.

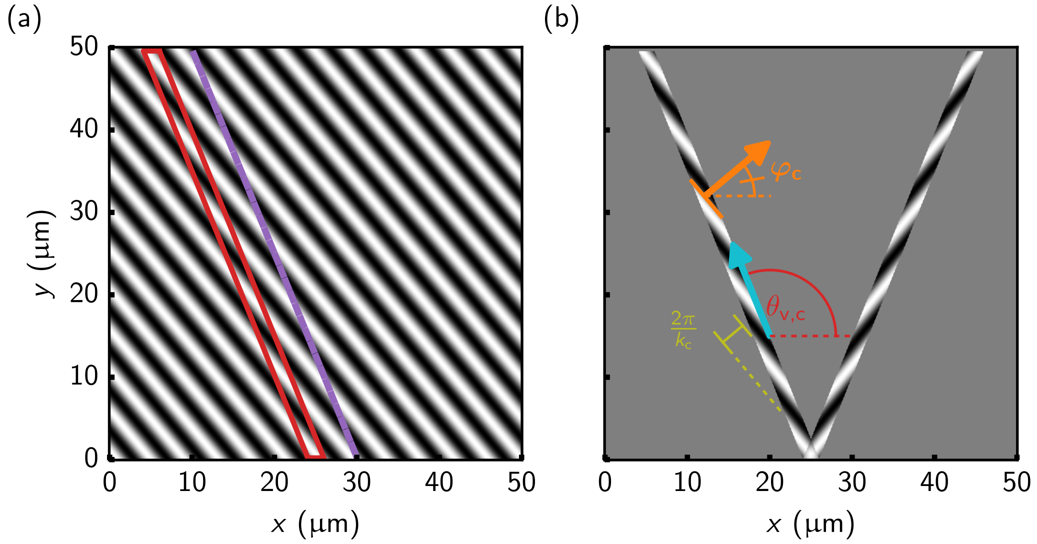

Figure 4.4. Schematic radiation pattern from a caustic point with $k_\mathrm{c} = 2\,\mu\mathrm{m}^{-1}, \varphi_\mathrm{c} = 40^\circ, \theta_{\mathrm{v,c}} = 112^\circ$. (a) Plane wave corresponding to the carrier wave. The red lines highlight the group velocity direction. The grey scale denotes the out-of-plane component of the magnetization. In Fig. 4.5, the profile along the purple line illustrates the apparent wavelength. (b) Exemplary caustic radiation pattern emitted from a point source. Two caustic beams corresponding to caustic points on the first and second quadrant of the iso-frequency curve are excited. As can be seen, group and phase velocity directions diverge significantly.

While the profile of a CSWB is beyond the scope of this work, it is important to note one subtle aspect. In the context of inhomogeneous media, the illumination profile is determined by considering phase variations and integrating across the entire k-space [26, 141, 151]. This approach is effective in isotropic media where the group and phase velocities align on the same

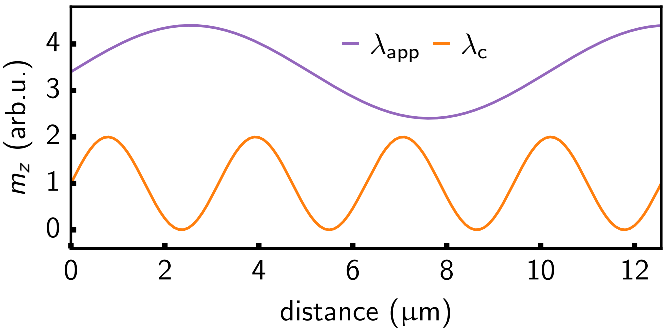

Figure 4.5. Depiction of apparent wavelength. The purple curve shows the profile extracted along the direction of the purple line in Fig. 4.4(a). The apparent wavelength may deviate significantly from the carrier wavelength (orange curve).

axis. However, in anisotropic media, the group velocity's non-collinear direction geometrically prevents a broad range of k-values from traveling from a point source to a distant point on the caustic. Hence, for spin wave caustics, only small, nearly straight parts of the iso-frequency curve contribute to the CSWB, naturally limiting the relevant wave vectors [26].

Another property useful to introduce is the apparent wavelength. The apparent wavelength can be defined as the projection of the carrier wavelength, λ_c, along the direction of the beam. Mathematically, it can be expressed as:

$$\lambda_{\mathrm{app}} = \frac{\lambda_{\mathrm{c}}}{\cos\left(\theta_{\mathrm{v,c}} - \varphi_{\mathrm{c}}\right)}, \qquad \text{or} \qquad k_{\mathrm{app}} = k_{\mathrm{c}} \cos\left(\theta_{\mathrm{v,c}} - \varphi_{\mathrm{c}}\right). \tag{4.2}$$

Since the iso-frequency curve allows for considerable discrepancies between φ_c and $\theta_{v,c}$, the apparent wavelength can take values much larger than λ_c. Combined with the beam's limited sharpness, this can result in limited wavefront information. In the extreme case, where $(\theta_{v,c} - \varphi_c) \rightarrow \frac{\pi}{2} + n \cdot \pi$ $(n \in \mathbb{Z})$, the beam may no longer carry any wavefront information at all. Moreover, notions such as propagation-induced phase and spectral breadth of the beam should be considered carefully [26]. Fig. 4.5 illustrates the discrepancy between the apparent wavelength and the carrier wavelength within the discussed radiation example.

4.3. Systematic Investigation of Caustic Points

In order to identify caustic points and their properties, a systematic investigation of the dispersion relation Eq. (1.24) is conducted. The objective is to parse the iso-frequency curve under varying magnetic fields and frequencies and locate caustic points that satisfy the condition specified in Eq. (4.1). The identified caustic points can then be represented and classified based on their properties k_c, φ_c and $\theta_{v,c}$.

To accomplish this task, a Python toolkit was developed to reconstruct the iso-frequency curve for different sets of experimental parameters, namely material parameters, magnetic field, and frequency. The toolkit further provides various functions and modules that facilitate the parsing and analysis of the iso-frequency curve data. We refer to the Supplementary Materials of [26] for a more comprehensive workflow description. However, it is important to note that even though the algorithms may be applied to magnetic fields above the respective

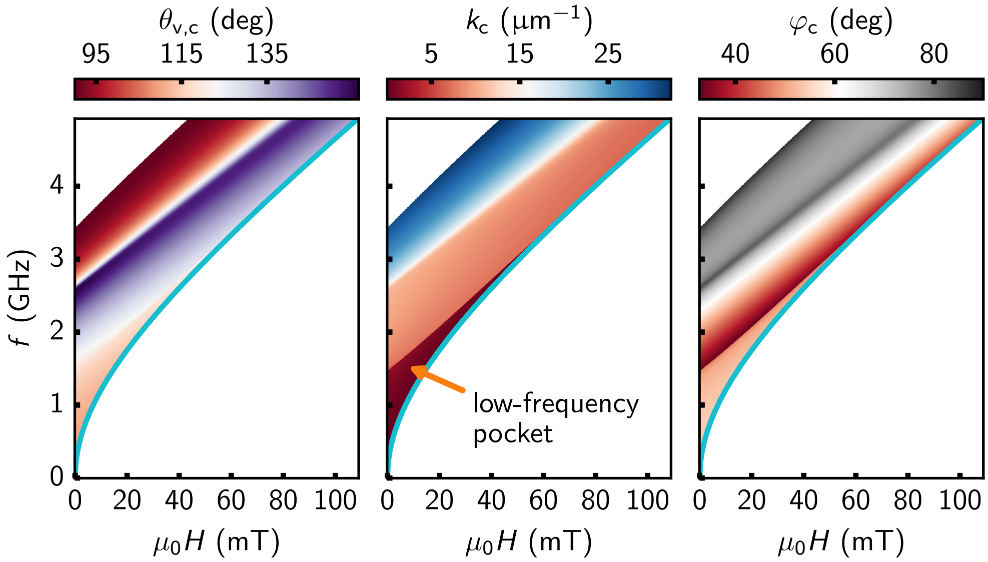

Figure 4.6. Frequency and field maps of caustic properties for a 200 nm thick YIG film. A low-frequency pocket emerges where k_c is relatively small. This region holds practical significance as it is readily accessible in experiments. A detailed description can be found in the text.

FMR magnetic field, the following analysis is restricted to magnetic fields only below the FMR condition.

Fig. 4.6 displays a set of frequency and field maps of caustic properties k_c, φ_c and $\theta_{v,c}$ for a 200 nm thick YIG film, generated using the Python toolkit. A band representing the existence of caustic points is depicted in all three maps. White space above this band indicates that no caustic points were found; white space below the band indicates that the condition was not investigated since those fields lie above the FMR field. The FMR condition is represented by a cyan-colored line.

Overall, a wide range of beam parameters is predicted, suggesting that CSWB properties can be tailored simply by adjusting the external magnetic field or the excitation frequency. Going down in frequency across the caustic band, $\theta_{v,c}$ exhibits a smooth increase, while k_c and φ_c decrease gradually. At lower frequencies, a sharp boundary occurs, marking a transition of the caustic wavenumber from the dipolar-exchange to the dipolar regime characterized by $k_c < 2\,\mu\text{m}^{-1}$. The wavefront angle also undergoes a jump towards higher angles, whereas the beam direction shows a more gradual transition towards lower values. Below this boundary line, the caustic properties appear to remain close to constant. This region will be referred to as the low-frequency pocket and holds significance in the later experiments, as wavelengths within this range can still be adequately excited and optically detected employing TR-MOKE microscopy.

The caustic properties strongly depend on the material parameters of the investigated film. For example, Fig. 4.7 presents the frequency and field maps of the caustic wavenumber for

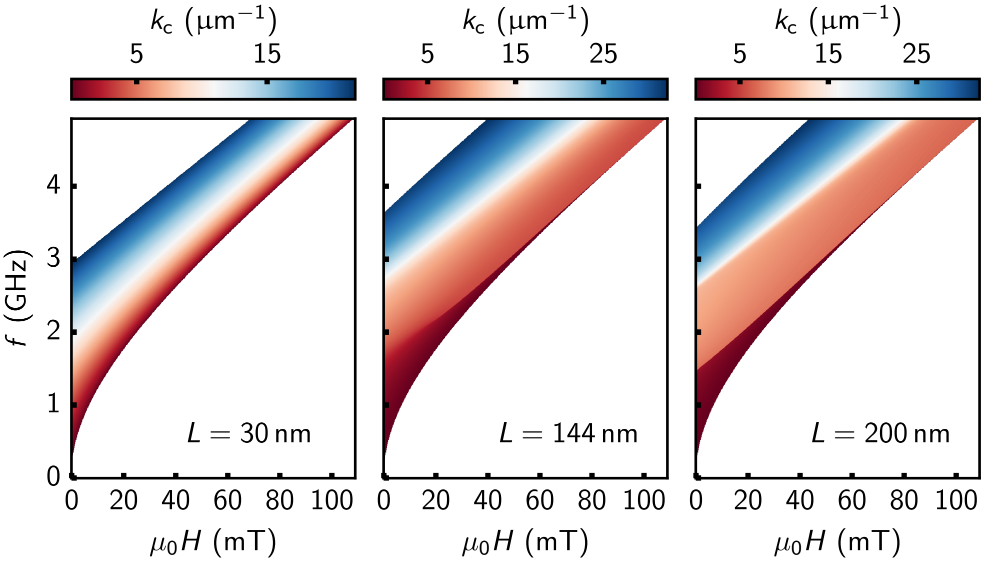

Figure 4.7. Frequency and field maps of caustic wavenumbers for different YIG thicknesses L. The caustic properties and the domain where caustic beams are generated vary with thickness. As thickness decreases, the transition to the low-frequency pocket becomes less distinct. Please note the distinct color scale for each graph.

different YIG film thicknesses. It can be observed that the caustic band, in general, varies in shape and wave vector values. In particular, for $L = 30$ nm, the band is considerably narrower, while for $L = 144$ nm it appears broader compared to the 200 nm thick film. Moreover, the transition to the low-frequency pocket becomes less abrupt with decreasing thickness. In the case of 144 nm film, the boundary remains sharp down to a frequency of approximately 2.2 GHz; however, below this frequency, it smears out and becomes more continuous. For 30 nm no sharp boundary is visible at all.

Note that, thus far, the analysis has focused solely on one undulation point along the iso-frequency curve, the one corresponding to the lowest wavenumber. However, there may actually be more than one caustic point for a given magnetic field and frequency. In the case of a 200 nm thick YIG film, up to three caustic points can emerge from one given iso-frequency curve as illustrated in Fig. 4.8.

Notably, within the domain where caustic points exists, the iso-frequency curve hosts either only one or three caustic points at the given frequency and field condition. This behavior can be quantitatively understood by examining the local behavior of $d\theta_\mathrm{v}/dk$. As $d\theta_\mathrm{v}/dk$ crosses zero, it does so similar to a polynomial of the form $P(k) = -(k - k_\mathrm{c})^3 + a(k - k_\mathrm{c}) + b$ [26]. If $a < 0$, a single root exists, while if $a > 0$ and b is sufficiently small, three roots will emerge. To illustrate, Fig 4.9 depicts the behavior of $d\theta_\mathrm{v}/dk$ for different iso-frequency curve scenarios featuring only one root and three roots. The somewhat cubic behavior also provides a quantitative explanation for the sharp transition into the low-frequency pocket. From Fig. 4.8, it can be seen that the upper boundary of the low-frequency pocket coincides with the emer-

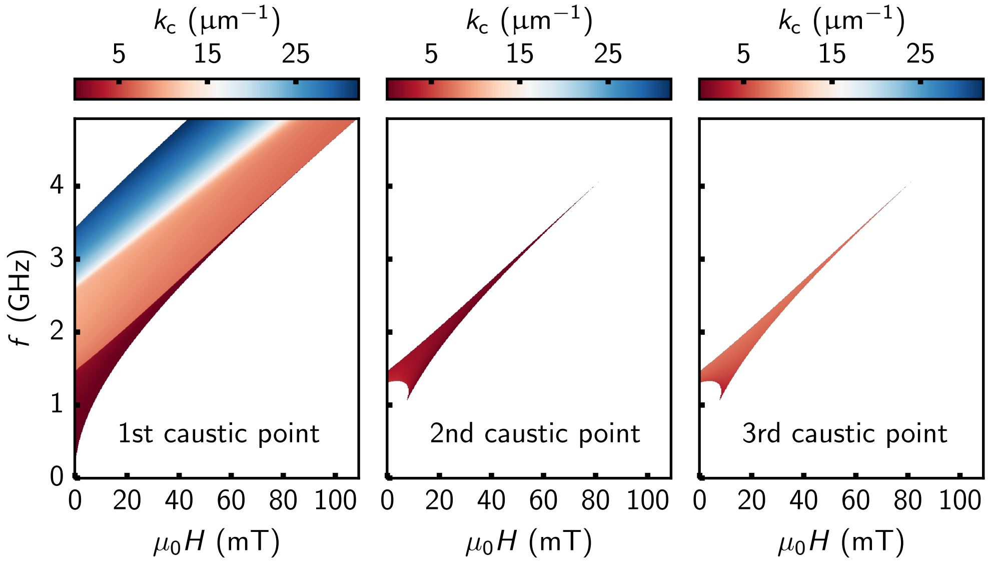

Figure 4.8. Frequency and field maps of first, second, and third caustic point for a 200 nm thick YIG film.

gence of the second and third caustic points. Transitioning from the domain of a single caustic point toward lower frequencies at a fixed field, the parameter a increases. This causes a shift of the lower wavenumber region closer to zero. Crossing the low-frequency boundary, a becomes positive, and two additional caustic points emerge at lower wavenumbers. The previous caustic point, observed in the single caustic point domain, now corresponds to the highest wavenumber caustic point in the three caustic points domain. A new lowest wavenumber caustic point emerges with different properties than the previous one, as illustrated in Fig 4.9.

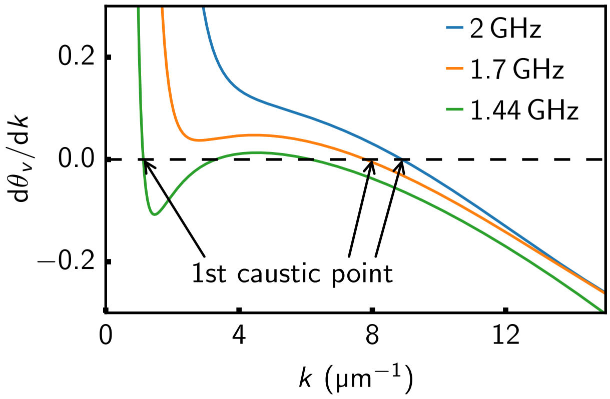

Figure 4.9. $d\theta_{\rm v}/dk$ as a function of wave vector at a magnetic field of $\mu_0 H = 5\,\mathrm{mT}$. When crossing zero, $d\theta_{\rm v}/dk$ behaves similarly to a cubic polynomial. At 2 GHz and 1.7 GHz, one root exists, while at 1.44 GHz, three roots are found. A jump in lowest wavenumber caustic point occurs when crossing the low-frequency pocket boundary.

To conclude this section, it is important to highlight that while a purely mathematical analysis identifies distinct caustic points, quantifying this distinction experimentally is challenging due to the lack of a straight-forward signature of $d\theta_\mathrm{V}/dk$ crossing zero [26]. Additionally, close-to-straight portions of the iso-frequency curve can also exhibit focussing effects [27, 33, 34, 42, 47, 49]. The radiation pattern of these caustic-like features is essentially indistinguishable from that of a true caustic point where the derivative goes to zero. Often, there is a transition from a caustic-like regime to a true caustic point, which is not discrete but continuous, rendering any clear distinction between the two scenarios difficult in the first place.

4.4. Limit of Model Applicability

The previous discussions were based on the thin film approximation, where the thickness of the film is comparable to the exchange length of the material. However, deviations may arise for thick films as PSSWs have to be considered (cf. Section 3.1).

In the experiments, 200 nm thick YIG films are investigated, which can already be considered relatively thick compared to the exchange length in YIG, $l_\mathrm{ex} \approx 17\,\mathrm{nm}$. Fig 4.10 displays micromagnetic simulations of the dispersion using TetraX for a 200 nm thick YIG under a magnetic field of $\mu_0 H = 5\,\mathrm{mT}$ at various angles between the external magnetic field and the spin wave propagation direction. The differences between the two models are negligible at relatively low frequencies but become more pronounced going toward high k-values and, hence, higher frequencies. Moreover, the frequencies at which these deviations become prominent shift towards lower values for smaller angles φ, leading to distortions of the iso-frequency curve in those regimes.

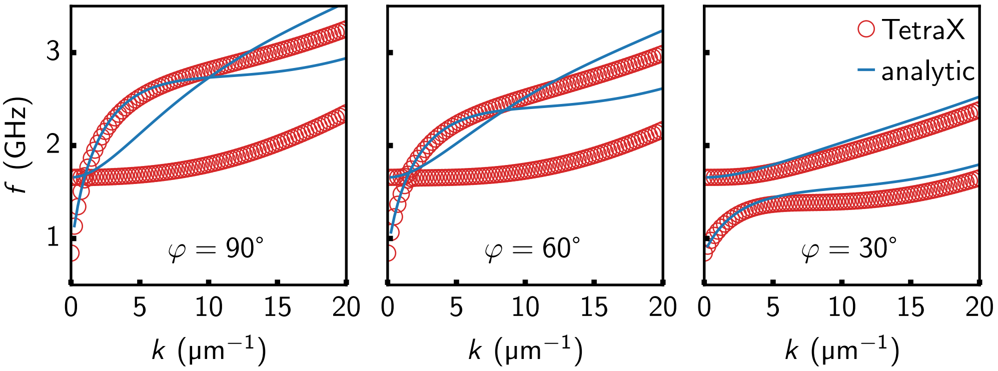

Figure 4.10. Dispersion relation of lowest two thickness modes for a 200 nm thick YIG film with an magnetic field of $\mu_0 H = 5\,\mathrm{mT}$, calculated by TetraX (red). Deviations from the analytic model (blue) are observed for different angles φ between the wave vector and in-plane field.

Furthermore, it can be observed that the mode hybridization is not solely limited to the DE geometry ($\varphi = 90°$) but can also be encountered for intermediate values of φ (e.g., $\varphi = 60°$).

Given that the thin film approximation neglects mode hybridization, deviations of the iso-frequency curve from the discussed caustic model are also expected near these anticrossing points.

4.5. Micromagnetic Simulations

Fig. 4.11 shows micromagnetic simulations of a 200 nm thick YIG film, performed using MUMAX3. In these simulations, spin waves are excited from a cylindrical region of different diameters using an out-of-plane excitation field at $f = 1.44\,\mathrm{GHz}$, under an in-plane bias magnetic field of $\mu_0 H{=}5\,\mathrm{mT}$. The radial geometry of the excitation source ensures that the iso-frequency curve is excited over the full angular range $\varphi \in [0, 2\pi]$. The cell dimensions were chosen to be 10 nm × 10 nm in the xy-plane, and 200 nm in the z-direction. Since no discretization in the z-direction is present in this simulation, PSSWs are neglected.

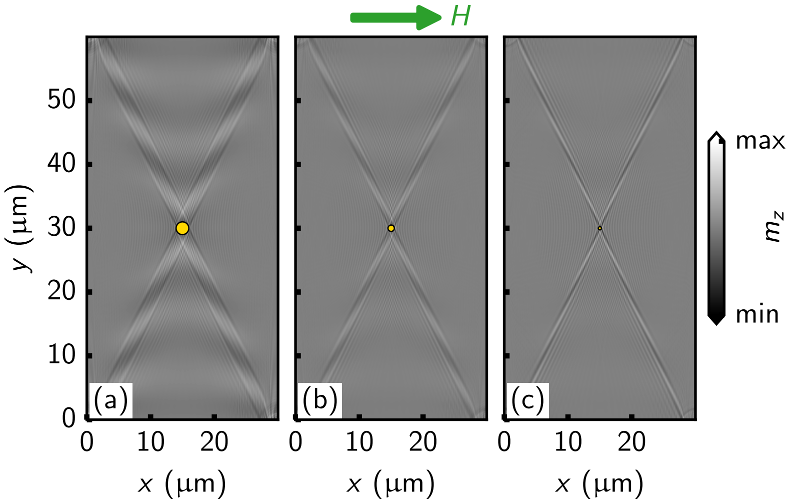

Figure 4.11. MUMAX3 simulations of m_z with excitation diameters of (a) 2 µm, (b) 1 µm, and (c) 0.5 µm. The excitation sources are illustrated by golden circles. The external magnetic field is applied along the x-direction. Note that each map's color scale was adjusted individually to increase contrast.

Indeed, four spin wave beams propagating from the excitation area are visible for each size of excitation source. The sharpness of these beams varies, which can be attributed to the different sizes of the excitation sources. A smaller excitation source results in a higher density of stationary group velocity directions per arc length of the cylindrical excitation source, leading to sharper beams. Moreover, the corresponding beam parameters have been extracted and are summarized in Table 4.1. The relevant parameters were determined using image processing and bootstrapping least-squares regression procedures. Appendix A provides a detailed walkthrough and example of this extraction process using experimental data. Nevertheless, the extracted beam parameters differ significantly depending on the size of the excitation source. Note that under the given magnetic field and frequency condition, 3 caustic points are predicted, whose properties are also displayed in Table 4.1 for comparison.

To further understand the discrepancies in beam parameters, Fig. 4.12 exhibits the magnitude Fourier-transformed (FT) data from the micromagnetic simulations. The FT data essentially allows for direct observation of the excited parts of the iso-frequency curve in k-

	sim. 2 µm	sim. 1 µm	sim. 0.5 µm	pred. CP1	pred. CP2	pred. CP3
θ_v (deg)	114.1	113.6	113.7	115.1	113.8	114.1
k (µm^{-1})	1.32	3.12	7.59	1.13	3.30	6.16
φ (deg)	49.1	34.2	27.9	51.3	33.2	28.9

Table 4.1. Extracted beam parameters from micromagnetic simulations with different excitation sources (cf. Fig. 4.11) and predicted parameters for caustic points (CPs) 1, 2, and 3 for $f = 1.44\,\mathrm{GHz}$ and $\mu_0 H = 5\,\mathrm{mT}$.

space. Due to the symmetry of the iso-frequency curve, only the range $\varphi \in [0, \pi]$ is displayed. Note that Hanning windowing was applied during transformation to reduce spectral leakage, which provides a good trade-off between wave vector and amplitude accuracy. Unless stated otherwise, Hanning windowing was also used for FT maps later on in the experimental section.

First, the contour of the FT data agrees well with the reconstructed iso-frequency curve (red dashed line in Fig. 4.12(b)), validating the model in the thin film approach. The FT data also shows that different excitation sources selectively excite portions of the iso-frequency curve with varying efficiency. As the size of the excitation source decreases, it can excite higher wave vectors, reducing gaps in the excitation spectrum and making the excitation of caustic points more uniform. Ideally, a true point source would uniformly excite all wave vectors, eliminating these gaps.

Figure 4.12. Magnitude of Fourier-transformed (FT) data of simulations in Fig. 4.11 with excitation diameters of (a) 2 µm, (b) 1 µm, and (c) 0.5 µm. The predicted caustic points (CPs) are marked with orange dots, and a reconstructed iso-frequency curve (red dashed curve in (b)) is shown for comparison.

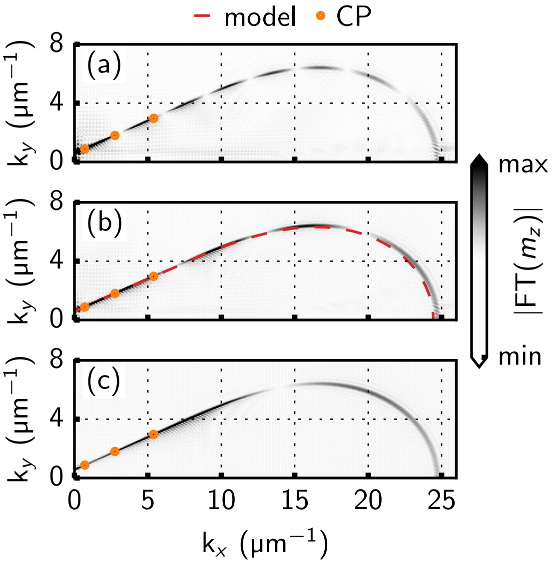

For the 2 µm simulation (Fig 4.12(a)), the caustic point at the lowest k-value is excited efficiently, while the caustic points at higher k-value are not excited at all (orange dots). Consequently, the extracted beam parameters closely match the predicted parameters for

CP 1 (cf. Table 4.1). For the 1 µm source, caustic points 1 and 2 seem to be excited efficiently, and the beam parameters match acceptably with the predicted parameters of CP 2. For the 0.5 µm case, all 3 caustic points are excited, but portions slightly above the k-value of the third caustic point are excited most efficiently. The extracted beam parameters align with the predicted ones for CP 3; however, the extracted k-value is much higher.

These observations can be better interpreted by considering the behavior of $d\theta_{\mathrm{v}}/dk$ for the given frequency and magnetic field condition (cf. green curve in Fig 4.9). At the first caustic point, $d\theta_{\mathrm{v}}/dk$ crosses zero very abruptly, whereas the crossing occurs very gradually close to CP 2 and CP 3. This gradual crossing allows for more almost stationary group velocity directions to contribute to the caustic beam. As a result, if, e.g., CP 1 and CP 2 are both excited sufficiently, the portion of the iso-frequency curve close to CP 2 may dominate the radiation pattern. Furthermore, $d\theta_{\mathrm{v}}/dk$ predicts that over a large portion of k-values ($3\,\mu\mathrm{m}^{-1} \lesssim k \lesssim 8\,\mu\mathrm{m}^{-1}$) the iso-frequency curve remains close-to-straight, even beyond the expected third caustic point. The 0.5 µm source excites this portion very efficiently (see Fig 4.12(c)). Thus, the corresponding radiation pattern likely arises from a caustic-like feature rather than a true caustic point. This further illustrates the difficulty in distinguishing radiation patterns originating from true caustic points and caustic-like features, especially since they are often in close proximity along the iso-frequency curve.

In summary, spin wave beams can be launched from caustic points, but the excitation source is crucial for making these points accessible and significantly influences the properties of the observed spin wave beams by determining which parts of the iso-frequency curve are excited. Moreover, distinguishing between true caustic points and caustic-like features is challenging, if not impossible, as no clear signatures indicate a truly stationary group velocity. Consequently, the beam may not exhibit the properties of the predicted true caustic point, as the radiation pattern may not solely originate from this point but instead be dominated by nearly straight portions of the iso-frequency curve.

5. Experimental Design

In order to experimentally study caustic points and CSWBs, it is essential for the spectrum of spin wave excitation to cover a wide range of wavenumbers and possible wave vector directions. This ensures sufficient excitation of the portion of the iso-frequency curve containing the caustic point. As previously discussed, achieving the ideal case where all wave vectors are uniformly accessible would correspond to a spin wave point source. However, this scenario is not attainable for any high-frequency antenna. Consequently, a compromise must be made between ease of fabrication and broadband excitation. Two separate approaches were employed in the experiments: a half-ring-shaped microstrip antenna and an antidot in the magnetic film from which plane waves are scattered [27].

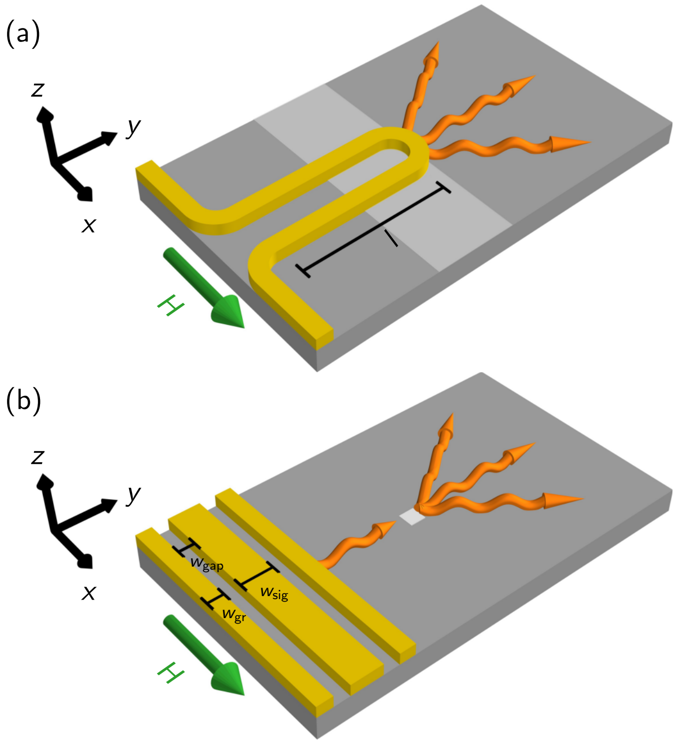

Figure 5.1. Schematic of the measurement configurations. (a) Spin waves are excited within a broad angular range from a half-ring-shaped microstrip antenna. To suppress plane wave background from the legs of the antenna aligned with the x-axis, either (i) $l = 1\,\mathrm{mm}$ was chosen, or (ii) the light grey area was etched away and $l = 50\,\mu\mathrm{m}$ was chosen. (b) Plane waves excited by a coplanar waveguide (CPW) scatter from an antidot (white area) over a broad angular range.

In the case of the half-ring-shaped microstrip, the design allows for excitation of the iso-frequency curve within $\varphi \in [0, \pi]$. However, the excitation spectrum in k-space is not uniform due to the microstrip width on the order of a micrometer. In the antidot configuration, on the other hand, the antidot essentially acts like a point source, enabling, in principle, access to a broad k-spectrum within $\varphi \in [0, 2\pi]$. Its excitation efficiency, however, depends on the strength of the incoming plane wave, which itself is non-uniformly excited by a CPW.

The experiments were conducted on a 200 nm thick YIG film grown on gadolinium gallium garnet (GGG) substrate. For the half-ring configuration, a microstrip antenna with a width of 2 µm to 3 µm was patterned on top of the YIG film by optical lithography with subsequent Argon pre-etching and electron-beam-induced evaporation of Cr(5 nm)/Au(100 nm-220 nm). The same procedure was used for the antidot sample to fabricate a CPW with $w_{\mathrm{sig}} = 10\,\mu\mathrm{m}$, $w_{\mathrm{gr}} = 5\,\mu\mathrm{m}$ and $w_{\mathrm{gap}} = 5\,\mu\mathrm{m}$. Here, additional optical lithography and subsequent Argon etching of the film were executed to create a square-shaped antidot within the film. During the measurement, if not stated otherwise, the external magnetic field was kept fixed along the x-direction. Figs. 5.1 illustrates a schematic of the two measurement configurations.

It is worth mentioning that in the antidot configuration, the CSWBs are always superimposed on the initial DE-like plane wave. The half-ring structure, on the other hand, can provide a more isolated investigation of CSWBs, as no additional plane wave is required for their excitation. However, the legs of the microstrip, which are aligned along the x-direction, excite spin waves in the DE-geometry. Due to the low damping [2], and hence, relatively long attenuation length in YIG, these modes may propagate to the antenna's tip and interfere with the CSWBs excited by the half-ring. In order to minimize this artifact, two different design approaches were applied. Either (i) the microstrip was designed such that the distance l between the legs and tip (see Fig. 5.1(a)) was set to $l = 1\,\mathrm{mm}$, or (ii) $l = 50\,\mu\mathrm{m}$ was chosen and the YIG between legs and tip was etched away (light grey area in Fig. 5.1(a)).

6. Experimental Results

6.1. Evaluation of Caustic Spin Wave Beams at Low-Frequency Pocket Conditions

Fig. 6.1(a) shows a Kerr image recorded with a constant excitation frequency $f = 1.44\,\mathrm{GHz}$ under an external magnetic field $\mu_0 H = 5\,\mathrm{mT}$ in the half-ring-shaped microstrip geometry. This experimental condition lies within the low-frequency pocket, and 3 caustic points are predicted (cf. Table 4.1). The width of the microstrip was $2\,\mu\mathrm{m}$, and the distance l between legs and tip was $1\,\mathrm{mm}$ (design (i) in Fig. 5.1(a)).

Two spin wave beams with distinct, well-defined propagation directions are visible. In between the beams, a curved wavefront is observed. Moreover, the phase and group velocity for each beam are clearly non-collinear to each other. Note that the observed spin wave pattern matches well with the micromagnetic simulation for a $2\,\mu\mathrm{m}$ excitation source (Fig. 4.11(a)). However, a small non-reciprocity of beam amplitude seems to be present, which will be discussed at the end of this section.

The two beams are further highlighted and labeled I and II in Fig 6.1(b). Beam I originates from the iso-frequency curve quadrant $\varphi \in [0, \pi/2]$ and has a beam angle of 119.0° with respect to the positive x-axis. Beam II, originating from the iso-frequency curve quadrant $\varphi \in [\pi/2, \pi]$, has a beam angle of 64.3° with respect to the positive x-axis. Projected onto the first quadrant of the iso-frequency curve, the beam directions are $\theta_\mathrm{I} \approx 119.0°$ (beam I) and $\theta_\mathrm{II} \approx 115.7°$ (beam II). Unless stated otherwise, any experimental angle (beam direction or wavefront angle) from now on is always projected onto the first iso-frequency quadrant within this thesis.

The slight asymmetry in beam direction can be assigned to a misalignment of the external magnetic field direction with respect to the x-direction. This deviation leads to a rotation of the iso-frequency curve by $\alpha_\mathrm{H} = (\theta_\mathrm{I} - \theta_\mathrm{II})/2 \approx 1.65°$ with respect to the experimental frame of reference. Taking this into account, the average beam direction is $\theta_{\mathrm{v,e}} \approx 117.4°$. Furthermore, the wavenumbers and wavefront angles are determined as $k_\mathrm{I} = 1.04\,\mu\mathrm{m}^{-1}$ and $\varphi_\mathrm{I} = 52.4°$ for beam I, and $k_\mathrm{II} = 1.07\,\mu\mathrm{m}^{-1}$ and $\varphi_\mathrm{II} = 48.9°$ for beam II (cf. Fig. 4.4(b) for illustration of beam parameters). Consequently, the average wavenumber and average wavefront angle are $k_\mathrm{e} = 1.06\,\mu\mathrm{m}$ and $\varphi_\mathrm{e} = 50.7°$. The apparent wavenumber along the beam direction was also extracted from a separate fitting procedure, yielding $k_\mathrm{app} = 0.42\,\mu\mathrm{m}$, which is significantly lower than the actual wavenumber k_e.[1] Overall, the experimentally determined values for $\theta_{\mathrm{v,e}}$, k_e and φ_e show good agreement with the parameters predicted

---

[1] It shall be reminded that a walkthrough on how the beam parameters are extracted is provided in Appendix A.

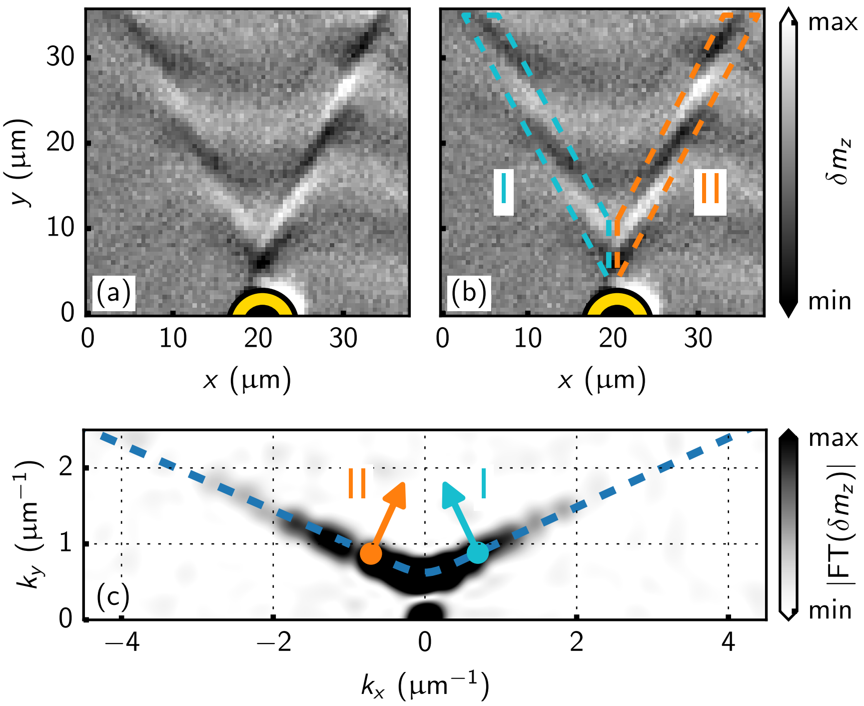

Figure 6.1. Measurement data obtained with a spin wave excitation frequency of $f = 1.44\,\mathrm{GHz}$ and an external magnetic field of $\mu_0 H = 5\,\mathrm{mT}$. (a) Kerr image acquired from TR-MOKE experiment. Two spin wave beams, highlighted in cyan and orange in (b), propagate from the tip of the microstrip. Gold indicates the position of the half-ring-shaped microstrip extracted from the topographic image. (c) Modulus of Fourier transformed (FT) Kerr image and expected iso-frequency curve (dashed blue line). The cyan and orange points and arrows indicate the expected caustic points and their group velocity directions in the low-frequency pocket. Caustic points I and II correspond to beams I and II in (b), respectively.

by the theoretical approach for a caustic point, which are $\theta_{\mathrm{v,c}} = 115.1°$, $k_{\mathrm{e}} = 1.13\,\mu\mathrm{m}$, and $\varphi_{\mathrm{e}} = 51.3°$.

To gain insight into the experiment in reciprocal space, the FT data of the Kerr image is depicted in Fig. 6.1(c). This transformation effectively yields a representation of the experimental iso-frequency curve. The FT data shows that the antenna structure excites a broad range of wave vector directions in the dipolar regime. As previously discussed, the gaps in the FT spectrum arise from the excitation source's finite size, i.e., the width of the microstrip.

A comparison between the FT spectrum and the reconstructed iso-frequency curve in the thin film approximation (blue dashed line) shows good qualitative agreement. Additionally, the FT data offers an alternative method to determine the external magnetic field angle, α_H. By fitting the FT data to the reconstructed iso-frequency curve (as detailed in Appendix B), $\alpha_H \approx 0.5°$ is found. This value is comparable to the field offset inferred from the slight deviation of beam directions. The reconstructed iso-frequency curve in Fig. 6.1 is presented with this rotation applied.

More importantly, the half-ring structure efficiently excites the expected caustic points in the low-frequency pocket (cyan and orange dots). Combined with the good match in experimental and predicted beam parameters, it may be concluded that beams I and II in the Kerr image correspond to caustic points I and II on the iso-frequency curve.

The conclusion that the beams stem from a true caustic point is further supported by the prediction of a very abrupt crossing of zero of $d\theta_{\mathrm{v}}/dk$ for the lowest wavenumber caustic point under the given experimental conditions (see green curve in Fig: 4.9). This point doesn't exhibit large close-to-straight portions of the iso-frequency curve in its close vicinity, whose radiation pattern would be indistinguishable from a true caustic point. In other words, close to the first caustic point, the group velocity directions capable of generating spin wave beams are highly concentrated around this point. As for the other two predicted caustic points and caustic-like portions, the antenna structure fails to excite these sufficiently, making them inaccessible in the experiment.

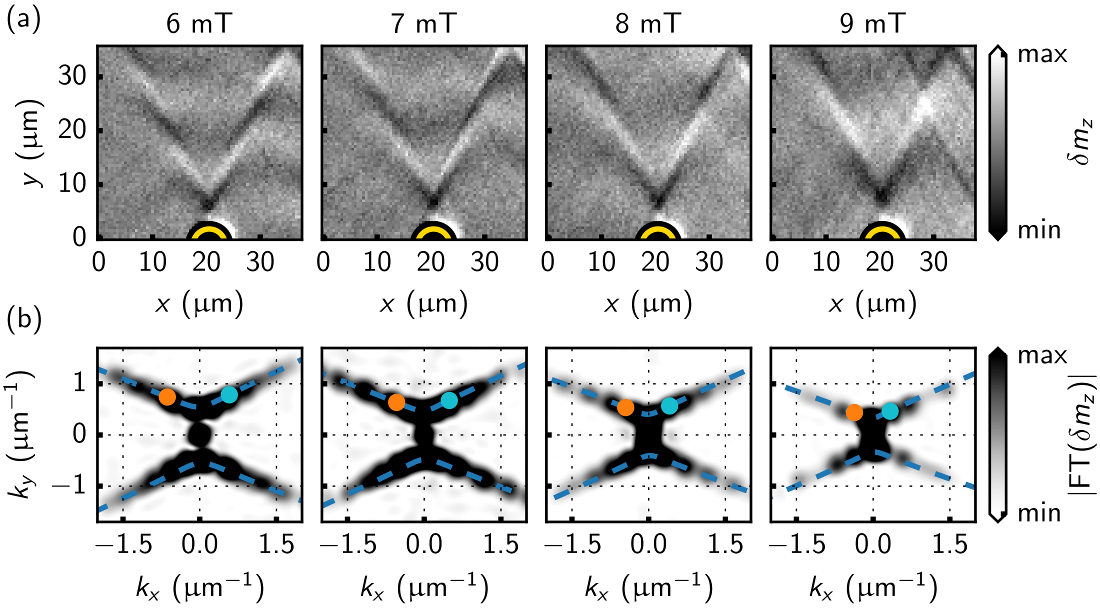

Figure 6.2. Measurement data with an excitation frequency of $f = 1.44\,\mathrm{GHz}$. (a) Kerr images for several external magnetic fields. All Kerr maps are normalized to the same color scale. (b) Corresponding Fourier-transformed data with reconstructed iso-frequency curve (blue dashed line) and expected caustic points (orange and cyan dots).

In Fig. 6.2(a), multiple Kerr images at the same excitation frequency (1.44 GHz) but different external magnetic fields are displayed. The chosen conditions still lie within the low-frequency pocket. Twin beams with different apparent wavelengths and beam directions, launched from the half-ring structure, are observable in each Kerr image. Note that spin wave beams not originating from the antenna structure are visible in some Kerr images (es-

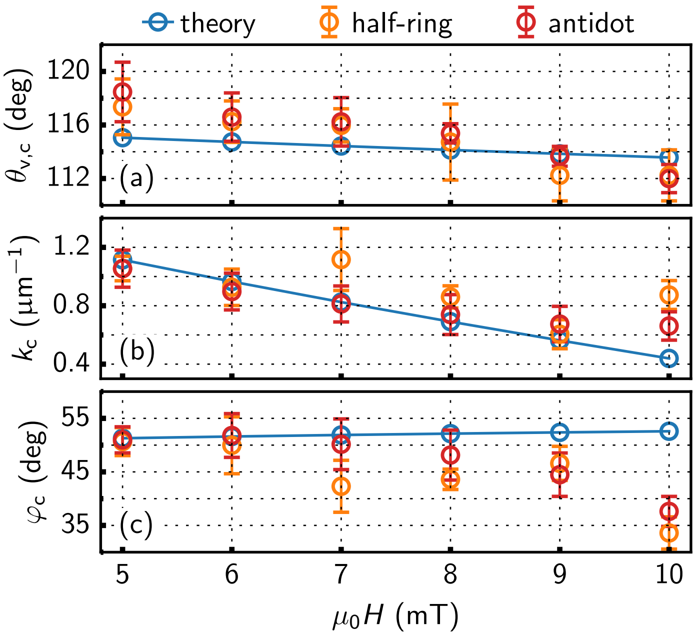

Figure 6.3. Extracted beam parameters (a) $\theta_{v,c}$, (b) k_c, and (c) φ_c from half-ring (orange) and antidot geometry (red) compared to predicted caustic point properties (blue). The error bars correspond to the standard deviation of a bootstrapping fitting procedure weighted with the deviations of beam parameters due to the external magnetic field angle offset.

pecially at 9 mT). These may be attributed to defects in the YIG film. The corresponding FT spectra (Fig. 6.2(b)) match, yet again, well with the predicted iso-frequency curves, and the respective caustic points are accessed sufficiently.

An overview of the extracted beam parameters is presented in Fig. 6.3 (orange circles). Clearly, the beam parameters change with the external magnetic field, and there is reasonable, sometimes even good, agreement between predicted and experimental values of $\theta_{v,c}$ and $\tilde{k}_c$. This strongly suggests that the observed beams are true CSWBs. The deviations in beam directions are mostly within the offset angle in the external magnetic field. The larger offset in wavefront range φ_c, with opposing trends in the simulation (increasing) and experiment (decreasing), may be attributed to the sharpness of the CSWB.

Additionally, Fig. 6.4 highlights the discrepancy between the actual wavenumber k_e and the apparent wavenumber $k_{e,app}$ extracted from the experimental data. The wavenumber projected along the beam direction consistently underestimates the actual wavenumber due to the strong non-collinearity of group and phase velocity. The experimentally acquired apparent wavenumber values show excellent agreement with the theoretically predicted ones, further suggesting that the discrepancy of theory and experiment at higher magnetic fields in Fig. 6.3 may indeed be inherent to the limited beam sharpness.

Further measurements using square antidots of different sizes (4 µm, 5 µm, and 6 µm) as scattering sources for plane waves were conducted using the same experimental conditions. Exemplary Kerr images are shown in Figs. 6.5(a) and (b). Distinct spin wave beams, superimposed with the initial plane wave excited from the CPW, are observed. The plane waves in the DE geometry propagate toward the antidots and are subsequently scattered. The resulting beams seem to be emitted from the edges of the antidots, which act as point sources, with each antidot edge generating twin beams. This can be seen clearest for the 6 µm antidot in

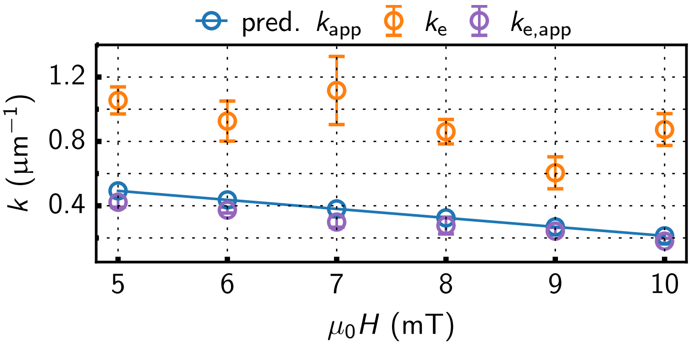

Figure 6.4. Actual wavenumber k_e (orange) and apparent wavenumber $k_{e,app}$ (purple) extracted from the half-ring Kerr data. The blue line represents the apparent wavenumbers predicted by the theoretical model.

Fig. 6.5(b), where the edge spacing is the largest. The antidot-generated beams also appear to be sharper in beam width than the beams excited by the half-ring antenna. Furthermore, due to the antidot symmetry, the iso-frequency curve is excited over the full angular range of $\varphi \in [0, 2\pi]$, causing the formation of beams not only in forward direction but also back toward the CPW.

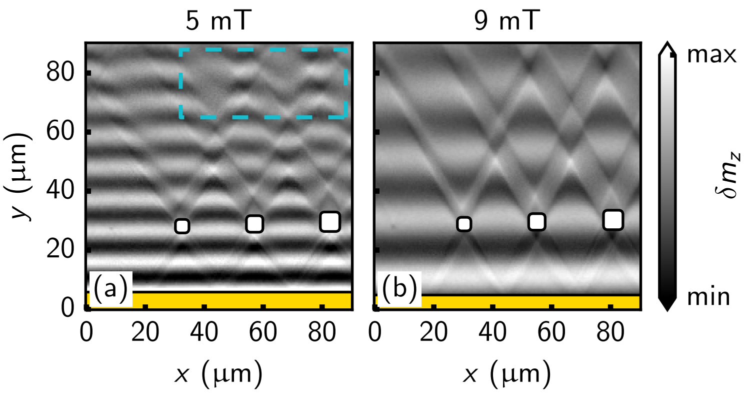

Figure 6.5. Kerr maps at 1.44 GHz for antidot geometry of different sizes under an external magnetic field of (a) $\mu_0 H = 5\,\mathrm{mT}$ and (b) $\mu_0 H = 9\,\mathrm{mT}$. The golden area highlights the position of the excitation antenna, while the white spaces indicate the antidot positions extracted from the topographic map.

The excitation efficiency and propagation profile of the beams appear to depend on the ratio between the wavelength of the incoming plane wave and the antidot size. When the antidot size becomes smaller compared to the spin wave wavelength, the beams seem to be excited more efficiently. This is due to the arrangement of antidots functioning as a diffraction grating. As the spin wave wavelength becomes comparable to the spacing between the antidots or the antidot size, diffraction phenomena become more pronounced [34, 36]. This effect is, for instance, observed within the cyan-colored contour in Fig. 6.5(a), where diffraction-induced patterns are observed beyond the antidot structure. As the wavelength increases, a transition into a caustic-dominated regime occurs [34, 36], resulting in less pronounced diffraction, as depicted in Fig. 6.5(b).

From the antidot structure, the beam parameters are extracted and shown as red circles in Fig. 6.3. These parameters align closely with the half-ring data and the predicted values for CSWBs. This indicates that the beam patterns stem from true caustic points, establishing antidots as another viable method for exciting CSWBs.

At this stage, the author addresses the non-reciprocity of amplitude between beam I and beam II, noting that beam II appears more intense (cf. Fig. 6.1(a)). This observation is supported by the respective amplitudes obtained from the fitting procedure. One possible explanation for this disparity is that the beams still display surface character. The surface character of the beams is suggested by the simulated modal profiles $|m_z|$ of the dynamic out-of-plane magnetization component m_z for the predicted caustic point properties at external magnetic fields of $\mu_0 H = 5\,\mathrm{mT}$ and $\mu_0 H = 10\,\mathrm{mT}$ in Fig. 6.6.[2] However, considering that the laser penetration depth for laser wavelengths between 400 nm and 800 nm typically ranges from a few hundred nanometers to a few micrometers [156][3] and that the focal lengths fall within a similar range[4], the laser should probe across most of the thickness of the YIG film. Additionally, if the modal nonreciprocity were the underlying cause, similar non-reciprocity would be expected in the antidot-induced measurements (cf. Fig. 6.5), yet no such clear signature was observed.

Another potential explanation is that the helicity mismatch with the excitation field causes a non-reciprocal emission (cf. Section 1.4), similar to the findings in Ref. [39]. However, considering the geometry of the experiment, where $\sin(\varphi_{\mathrm{II}}) = \sin(\pi - \varphi_{\mathrm{I}}) = \sin(\varphi_{\mathrm{I}})$, this explanation seems unlikely. It is still presumed that the non-reciprocity stems more from the antenna excitation, as it is absent in the antidot experiments, although the exact cause remains unclear.

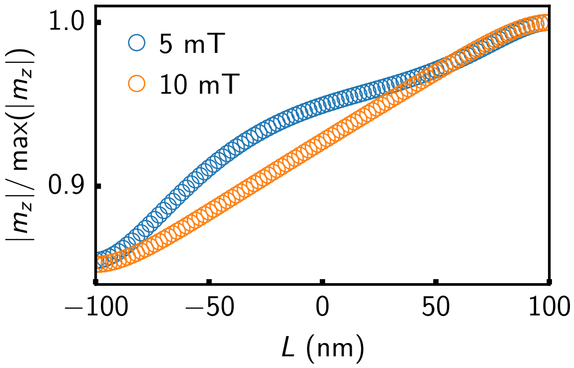

Figure 6.6. Numerically obtained mode profile of m_z across the film thickness L of predicted caustic properties at 5 mT (blue circles) and 10 mT (orange circles) and $f = 1.44\,\mathrm{GHz}$. The caustic beams are suggested to show an amplitude non-reciprocity where the magnitude of m_z is bigger at the top surface of the film.

In summary, this section demonstrated that low-frequency pocket caustic points can be accessed by designing suitable antenna structures and antidot geometries. The predicted and experimental values of the beam parameters are in reasonable agreement, indicating true CSWBs. Furthermore, their properties change as a function of the external magnetic field, showing the potential for tailoring and steering spin wave beams by tuning of the external magnetic field.

---

[2] Note that the beam localization is opposite to the DE case (cf. Fig. 1.6). This is consistent with the findings in Refs. [81] when the fundamental mode (n=0) approaches the first PSSW.

[3] The penetration depth is given by $L_{\mathrm{p}} = \frac{\lambda}{4\pi \mathrm{Im}(\tilde{n}(\omega))}$, where λ is the laser wavelength and $\mathrm{Im}(\tilde{n}(\omega))$ denotes the imaginary part of the material's refractive index. For laser wavelengths between 400 nm and 800 nm, typical values of $\mathrm{Im}(\tilde{n}(\omega))$ for YIG are below 0.2 [156].

[4] The focal length b of a Gaussian beam profile is given by $b = 2 \cdot z_{\mathrm{R}}$, where $z_{\mathrm{R}} = w_{\mathrm{b}}^2 \pi/\lambda$ is the Rayleigh length, w_{b} the radius of the beam waist and λ the laser wavelength [157].

6.2. Experimental Observation of Model Limitation

The experiments also exhibited beam-like spin wave features far from any predicted caustic point. Fig. 6.7(a) shows a Kerr map where spin waves were driven with an excitation frequency of $f = 1.84\,\mathrm{GHz}$ under an external magnetic field of $\mu_0 H = 5\,\mathrm{mT}$. In this measurement, the spin waves were excited using a half-ring antenna with a width of $3\,\mu\mathrm{m}$ and a tip-leg distance $l = 50\,\mu\mathrm{m}$, along with the partially etched YIG film at the microstrip tip (cf. design (ii) in Fig. 5.1(a)).

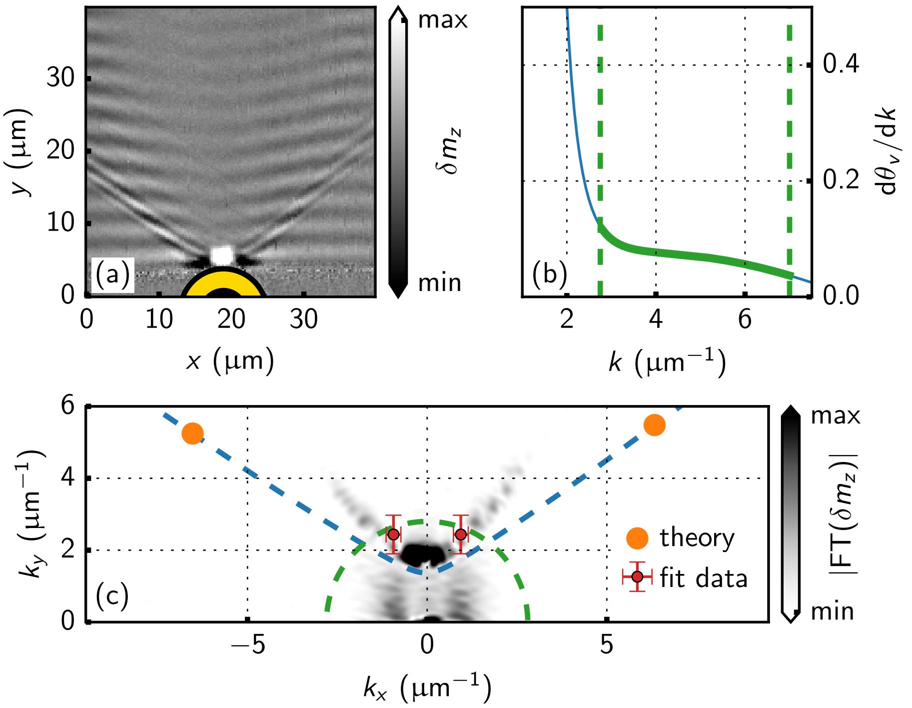

Figure 6.7. Measurement data obtained with an excitation frequency of $f = 1.84\,\mathrm{GHz}$ and with an external field of $\mu_0 H = 5\,\mathrm{mT}$. (a) Kerr map. (b) Calculated derivative of group velocity direction at given experimental conditions. The green part highlights the close-to-straight portion of the iso-frequency curve. (c) FT data of Kerr map showing experimentally extracted beam parameters in red, reconstructed iso-frequency curve in blue, and the predicted caustic points in orange. Dashed green semicircle indicates the lower limit of the green portion in (b).

A plane wave background, along with twin beams, is observed in this geometry. The presence of plane waves, despite the antenna geometry in principle lacking to excite them over such a broad spatial range, can be attributed to a spatial variation of the dynamic demagnetizing field at the YIG edge at the microstrip tip. This variation can act as a source of propagating spin waves, as pointed out in [158]. Regarding the beams, the analysis procedure yields the following parameters: $\theta_{\mathrm{v,e}} = 136.3°$, $k_{\mathrm{e}} = 2.61\,\mu\mathrm{m}$, and $\varphi_{\mathrm{e}} = 69.0°$

(cf. Fig. 4.4(b)). In contrast, the thin film approach predicts only one caustic point with $\theta_{\mathrm{v,c}} = 133.3^\circ$, $k_\mathrm{c} = 8.37\,\mu\mathrm{m}$, and $\varphi_\mathrm{c} = 48.0^\circ$.

Examining the behavior of $d\theta_\mathrm{v}/dk$ (Fig. 6.7(b)), an almost stationary group velocity direction is predicted between $2.8\,\mu\mathrm{m} \lesssim k \lesssim 7\,\mu\mathrm{m}$ which lies within error bars of k_e. The proximity is also illustrated in the FT data in Fig. 6.7(c), where the dashed green semicircle denotes the lower limit $2.8\,\mu\mathrm{m}$ and the red dots denote the beam parameters extracted from the fitting procedure applied to the beams. This may explain the observed beams. However, for this almost stationary portion, group velocity directions of maximal $\theta_\mathrm{v} = 125\,^\circ$ are predicted, which is in stark contrast to the experimentally observed value.

Moreover, from Fig. 6.7(c), the FT data deviates significantly from the reconstructed iso-frequency curve (blue dashed curve), especially when going towards higher wavenumbers. As previously discussed, a 200 nm thick YIG film can already be considered relatively thick and may not be fully treated within the thin film approach. Recalling Fig. 4.10, it can be seen that the given experimental conditions ($f = 1.84\,\mathrm{GHz}$, $\mu_0 H = 5\,\mathrm{mT}$) lie close to the mode anticrossing, thus making the established caustic model less reliable. The experimental iso-frequency curve may still feature portions of stationary or almost stationary group velocity directions, which favors the formation of the observed beams; the caustic model, however, fails to capture this.

Another potential cause of the beam-like features could be the limited excitation efficiency of the microwave antenna, as indicated by the numerous gaps in the FT spectrum. The beam properties appear to align closely with some of these gaps, implying that the beams may correspond to the excitation of only a small portion of the iso-frequency curve within this region.

6.3. Limit of Phase Information in Spin Wave Beams

As previously mentioned and observed, the anisotropic spin wave propagation characteristics in in-plane magnetized films allow for a non-collinearity of beam direction and wavefronts. At an excitation frequency of $f = 1.2\,\mathrm{GHz}$ and an external magnetic field of $\mu_0 H = 10\,\mathrm{mT}$, comparable to the expected FMR field of $\mu_0 H_\mathrm{FMR} = 9.988\,\mathrm{mT}$, two caustic points are predicted: $\theta_{\mathrm{v,c1}} = 103.7^\circ$, $k_\mathrm{c1} = 0.60\,\mu\mathrm{m}^{-1}$, $\varphi_\mathrm{c1} = 11.8^\circ$, and $\theta_{\mathrm{v,c2}} = 104.2^\circ$, $k_\mathrm{c2} = 3.42\,\mu\mathrm{m}^{-1}$, $\varphi_\mathrm{c2} = 13.6^\circ$. For this condition, group velocity direction and wavefront angle are highly non-collinear, almost perpendicular, making it an interesting feature to probe experimentally. Given that the excitation frequency is quite low, our model may provide sufficient accuracy.

Fig. 6.8(a) shows a Kerr measurement where the magnetization dynamics are excited with a $3\,\mu\mathrm{m}$ wide half-ring antenna indicated by the yellow half-circle. Sharp twin beams emitted from two separate antenna portions are visible within a uniform background. Interestingly, almost no wavefronts or apparent wavelengths are visible within the beams. This suggests that group and phase velocity are indeed almost orthogonal to each other. Due to its finite width, the beams then carry almost no phase information anymore, causing the apparent wavelength to diverge, even though the portions contributing to the beam may have finite wavelengths. The FT data in Fig. 6.8(b) shows good agreement between theory and experiment and illustrates the near perpendicularity of k-vector (orange-colored arrow) and group

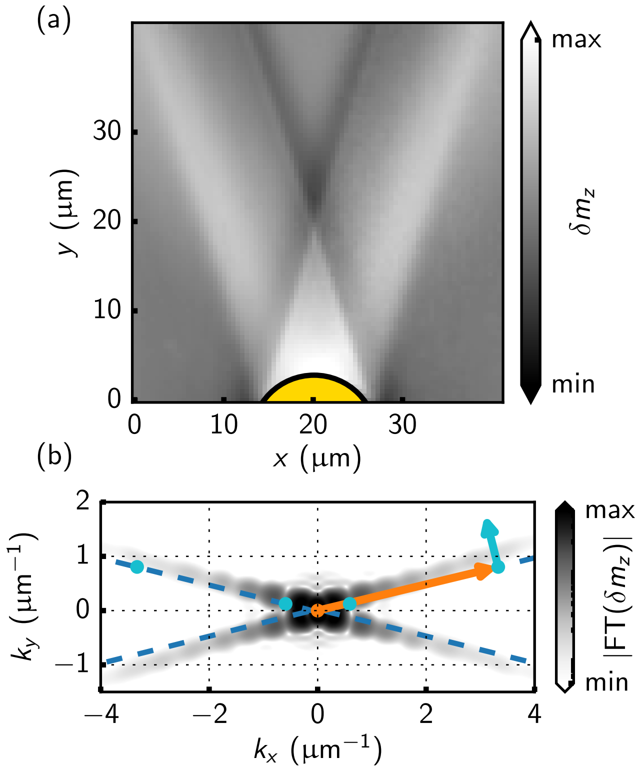

Figure 6.8. Measurement obtained with an excitation frequency of $f = 1.2\,\mathrm{GHz}$ and an external magnetic field of $\mu_0 H = 10\,\mathrm{mT}$. (a) Kerr map. Beams with almost no phase information are visible. (b) FT spectrum in logarithmic scale. The blue dashed line represents the reconstructed iso-frequency curve, and the cyan dots are the expected caustic points. The beam direction (cyan arrow) and k-vector (orange arrow) at a caustic point are almost orthogonal to each other.

velocity direction (cyan arrow). In fact, almost the full portion of the excited iso-frequency curve exhibits such a behavior.

In summary, this example demonstrates that beams with close to no phase information can be tailored. As a result, concepts such as propagation-induced phase and spectral breadth need to be treated carefully within spin wave beams.

6.4. Reflection of Caustic Spin Wave Beams in a Magnonic Waveguide

Reflection phenomena of plane spin waves in in-plane magnetized films have been studied extensively [37, 78, 159–166]. The reflection properties of pure spin wave beams have also been investigated in several theoretical and simulation studies [167–170]. Unlike caustic beams, pure spin wave beams can be understood as coherent low-diverging beams that do not form from anisotropic focussing effects [169]. Generating such beams remains more challenging; however, recent advancements have been made through the usage of non-uniform antenna designs [171, 172], the implementation of beam shaping techniques using curved antennas [173], and the production of high wave vector beams by coupling to a magnetic nanowire array [174].

At its core, the reflection of plane spin waves and pure spin wave beams adheres to Snell's law for spin waves, which requires continuity of the wave vector component tangential to the reflection interface [37, 56, 78, 164–166]. Experimentally, this reflection interface is typically implemented as a thickness step within the magnetic material, where the thickness step or edge serves as the boundary for reflection [56]. Assuming that the edge is aligned along the x-direction, Snell's law corresponds to the conservation of the k_x component. The k_y component, on the other hand, changes sign upon reflection, with its magnitude adjusting to keep the overall reflected wave vector on the iso-frequency curve. The same principles apply to the process of spin wave refraction, but the following experiments focus solely on spin wave reflection.

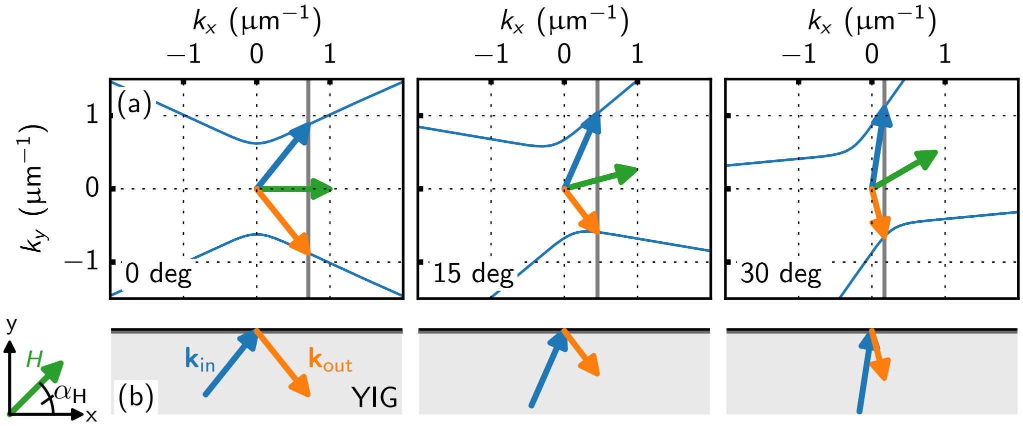

Figure 6.9. Snell's law for reflection of spin waves under varying external magnetic field angles. The top row (a) illustrates the reflection process via iso-frequency curves, with the blue arrow indicating the incoming wave vector, the orange arrow showing the reflected wave vector, and the green arrow representing the external magnetic field direction. The preserved k_x component is marked by the grey line. The bottom row (b) depicts the corresponding real-space reflection of the wave vectors at the reflection edge (dark black line), with the edge aligned along the x-direction. In experiments, the reflection interface is realized by a thickness step, which does not necessarily imply a transition to a region without magnetic material.

Fig. 6.9(a) illustrates the reflection process for spin waves on the example of a reconstructed iso-frequency curve with $f = 1.44\,\mathrm{GHz}$ and $\mu_0 H = 5\,\mathrm{mT}$ for several angles α_H between the external magnetic field and the reflection edge. The external magnetic field angle α_H is defined relative to the x-axis, or equivalently, the k_x-axis in reciprocal space. The incoming wave vector (blue) reflects, conserving the k_x component, and results in the reflected wave vector (orange). Depending on the external magnetic field direction, the wavenumber of the outgoing wave changes with respect to the incoming wave. Fig. 6.9(b) shows the corresponding real-space reflection of these wave vectors at the reflection interface. The angle of the incoming wave vector relative to the reflection edge is equal to that of the outgoing wave vector relative to the reflection edge.

In contrast, reflection phenomena associated with CSWBs, have only been briefly addressed in the literature [44, 175]. The beam direction of CSWBs is determined by the stationary group velocity direction rather than by wave vector directions alone. To preserve the caustic nature of these beams upon reflection, the reflected beam must also originate from a point of stationary group velocity direction on the iso-frequency curve [44]. If this condition is not met, the reflected spin waves don't exhibit a focussing effect.

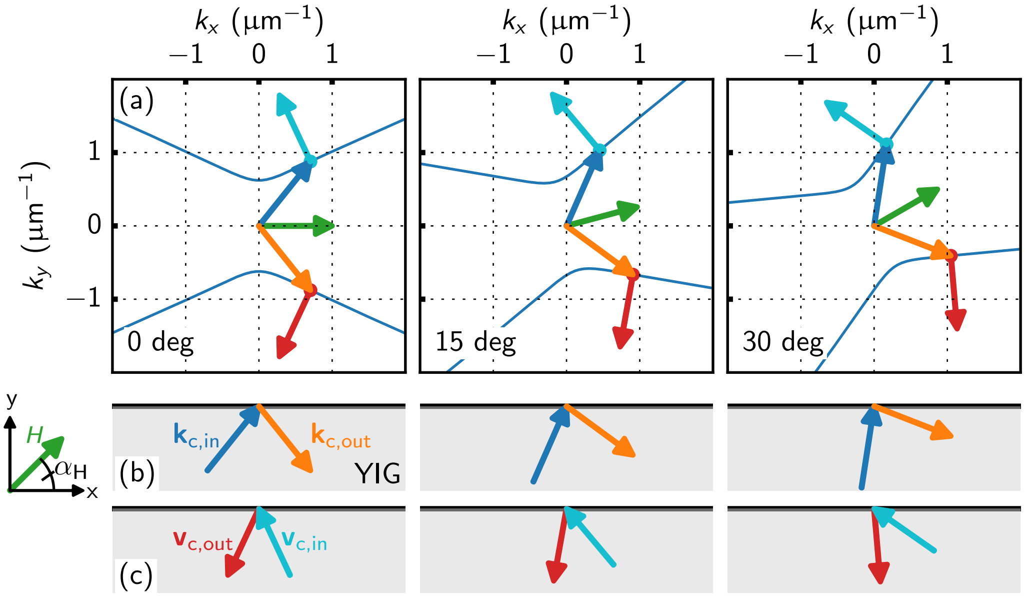

Figure 6.10. Reflection of caustic spin wave beams under varying external magnetic field angles. (a) Iso-frequency curve illustrating the reflection process of CSWBs, showing the transition between caustic points. The incoming beam direction is indicated in cyan, the incoming wave vector in blue, the outgoing beam direction in red, and the outgoing wave vector in orange. (b) and (c) depict the wave vectors and group velocity directions for the incoming and outgoing beams at the edge of the magnetic material. Notably, the angles of the incoming and outgoing beams relative to the edge are generally unequal.

Fig. 6.10(a) illustrates the reflection of CSWBs under different external magnetic field angles in the context of the iso-frequency curve ($f = 1.44\,\mathrm{GHz}$ and $\mu_0 H = 5\,\mathrm{mT}$). The low-frequency pocket caustic points are considered. As the beam reflects, it transitions from the caustic point in the quadrant $\varphi \in [0, \pi/2]$ (cyan dot) to the caustic point in the quadrant $\varphi \in [3\pi/2, 2\pi]$ (red dot). The incoming beam follows the group velocity direction indicated by the cyan arrow and the carrier wave vector indicated by the blue arrow. The outgoing beam exhibits a group velocity direction shown by the red arrow and an outgoing carrier wave vector shown by the orange arrow. The external magnetic field direction dictates the orientation of the iso-frequency curve [78], thereby controlling the positions of these caustic points and also enabling steering of CSWBs.

A representation of the wave vector and group velocity direction of incoming and outgoing beams at the edge of the magnetic material is provided in Figs 6.10(b) and (c), respectively. The orientations of the wave vectors and group velocity directions within each set (incoming and outgoing) differ significantly, often pointing in opposite directions. When the external magnetic field is aligned with the edge ($\alpha_H = 0$), both the incoming wave vector and group velocity directions reverse the y-component, resulting in the incident and reflected beam angles being equal. However, as the external field angle increases, the beam directions deviate from the conventional "incident angle equals reflected angle" rule. In some instances, such as at $\alpha_H = 30°$, the beam may even exhibit negative reflection. Although the wave vector maintains its magnitude, the wavefront angle with respect to the edge changes upon reflection.

In the following, the reflection properties of CSWBs are investigated in the low-frequency pocket by TR-MOKE microscopy. To achieve this, one of the twin beams emitted from the half-ring antenna was directed into a magnonic waveguide, where the beam can undergo multiple reflections at the waveguide edges. The other beam served as a reference. For this purpose, a YIG film was patterned into a waveguide structure with a nominal width of 40 µm by optical lithography and subsequent Ar etching. A topographic map of the geometry is shown in Fig. 6.11 where the edges are always oriented along the x-direction. The antenna width was 2 µm. In the first set of experiments, the external magnetic field was applied along the x-direction, while in the second set, the external magnetic field angle was varied.

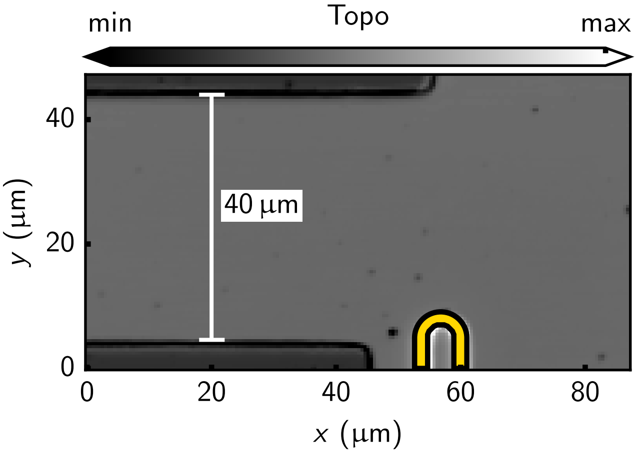

Figure 6.11. Topographic map of the experimental design, showing the spin wave waveguide fabricated on one side of the excitation antenna. Dark areas indicate regions where YIG was etched away. The waveguide edges are oriented along the x-direction.

6.4.1. External Magnetic Field Dependence of Reflection

Figs. 6.12(a)-(j) show Kerr images recorded at an excitation frequency $f = 1.44\,\text{GHz}$ under various external magnetic field values. On the basis of these Kerr images, the section first qualitatively discusses the propagation and reflection profile. Subsequently, it delves into an examination of the beam parameters $\theta_{\text{v,e}}$, k_{e}, and φ_{e} for the incoming and reflected beams, followed by an analysis of the reflection amplitudes.

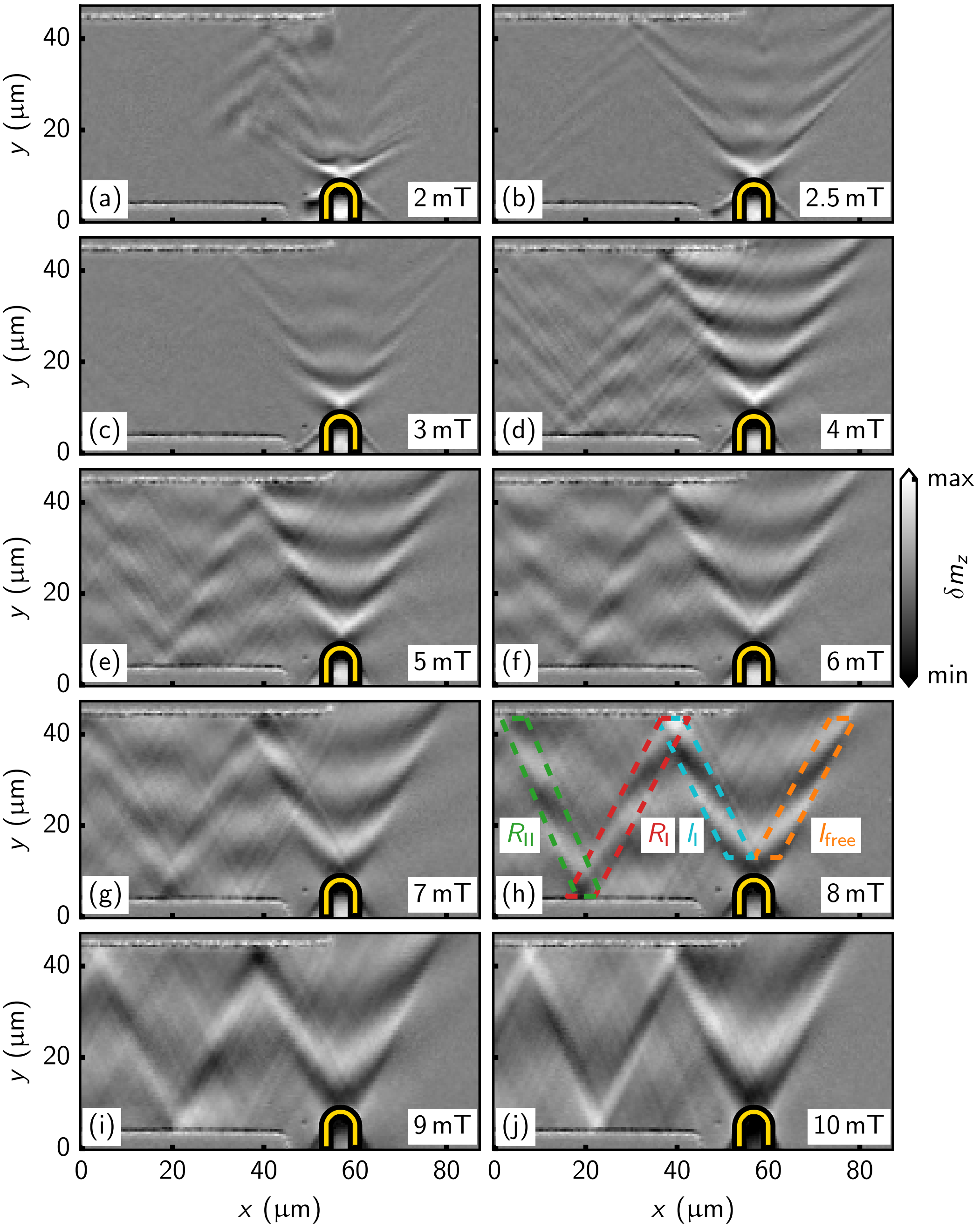

Figure 6.12. Reflection of spin wave beams in a magnonic waveguide (a)-(j) Kerr maps recorded at $f = 1.44\,\text{GHz}$ under different external magnetic fields. Caustic spin wave beams are reflected back and forth with varying efficiencies. All Kerr maps are normalized to the same color scale. A detailed description can be found in the text.

Qualitative Discussion of the Radiation and Reflection Profile

Each Kerr image shows a pair of beams emitted from the antenna tip, with the radiation profile changing as the applied field increases, resulting in larger apparent wavelengths. At relatively low external magnetic fields (Figs. 6.12(a)-(c)), little to no reflection of the beam coupled into the waveguide is observed. Specifically, at $\mu_0 H = 3\,\mathrm{mT}$ (Fig. 6.12(c)), no reflected beam is observed, while at $\mu_0 H = 2.5\,\mathrm{mT}$ (Fig. 6.12(b)) a slight first reflection within the waveguide is noted. At $\mu_0 H = 2\,\mathrm{mT}$ (Fig. 6.12(a)), the beam does not even enter the waveguide but is instead damped out, forming a complex wavefront pattern.

These observations at low fields are closely related to the proximity of the experimental conditions to the hybridization band, which, as shown in Fig. 3.2, occurs at very low magnetic fields (1 mT) for the given excitation frequency (1.44 GHz). Moreover, the edges of the waveguide induce demagnetizing effects, altering the effective magnetic field distribution. Micromagnetic simulations using MUMAX3 were conducted to visualize this effect. The results are shown in Fig. 6.13, which presents the spatial distribution of the x-component of the effective magnetic field ($\mu_0 H_{x,\mathrm{eff}}$) under an applied static field of $\mu_0 H = 3\,\mathrm{mT}$.[5] Within the waveguide, the effective magnetic field remains almost unchanged from the applied field, as it is aligned longitudinally to the waveguide axis. At the corners where the full film transitions into the waveguide, local reductions of the magnetic field are observed. Here, the reduction reaches up to 2 mT. Consequently, at the entrance of the magnonic waveguide, the hybridization condition is further approached due to the reduction in effective magnetic field, which strongly attenuates spin-wave propagation. A more detailed evaluation of this phenomenon is provided in Part III. In Fig. 6.12(a), this effectively creates a barrier, preventing the beam from entering the waveguide [34, 176].

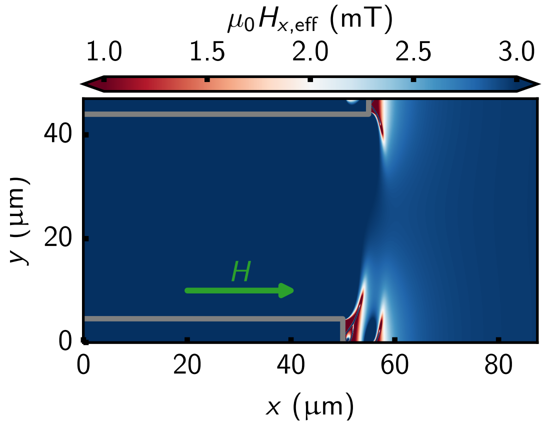

Figure 6.13. Simulated distribution of x-component of the effective magnetic field under an applied static field of $\mu_0 H = 3\,\mathrm{mT}$. The grey contour marks the edges of the waveguide where reductions of the effective magnetic field occur in the corners.

At higher external magnetic fields (Figs. 6.12(d)-(j)), when the beam emitted into the waveguide reaches the first edge, a reflected beam with an opposite y-direction and a wavelength similar to the incoming beam becomes clearly visible, with a mirrored wavefront angle.

---

[5] A grid of 1000 × 4400 × 4 was used in the simulation. To enhance simulation speed, and since the effective magnetic field rather than spin wave properties were of interest, the cell dimensions were chosen to be 50 nm in all 3 dimensions, which is above the exchange length in YIG.

This reflected beam then interacts with the opposite edge, leading to further reflections and changes in direction as the beams bounce back and forth within the waveguide. The patterned edge structures also excite caustic features, which are reflected multiple times, contributing to the complex background observed in many images.

Each point of the edge region serves as a secondary point-like excitation source with a finite size on the order of the beam's width [44, 140]. The secondary source radiates a wave packet with a wide angular spectrum accessing another caustic point on the iso-frequency curve [44]. In analogy to Figs. 6.10(a)-(c), during the first reflection, the incoming beam transitions from the caustic point in the quadrant $\varphi \in [0, \pi/2]$ to the caustic point in the quadrant $\varphi \in [3\pi/2, 2\pi]$ for the outgoing beam. At the second edge, the reflected beam folds back to the caustic point in the quadrant $\varphi \in [0, \pi/2]$. In the ideal case, where the external magnetic field is perfectly aligned with the edge, the beam parameters[6] of the incoming and outgoing beams are expected to remain the same.

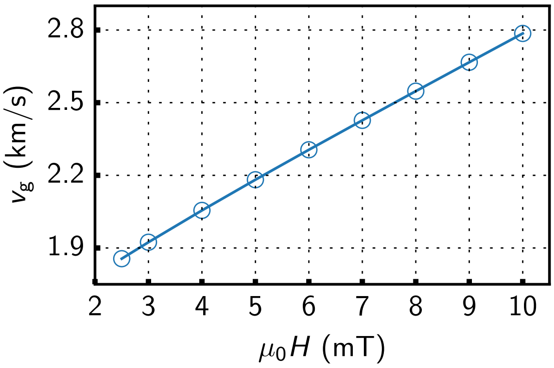

Figure 6.14. Predicted group velocities v_g of caustic points. With decreasing external magnetic field, v_g decreases, corresponding to a stronger spin wave attenuation.

Furthermore, the beam intensity appears to be influenced by the external magnetic field, with reflected beams becoming progressively weaker as the external magnetic field decreases. This weakening may be attributed to two factors. First, reflection losses, which will be discussed in more detail later on. Second, the reduction in group velocity (v_g) plays a role. As shown in Fig. 6.14, the group velocities at the predicted caustic points decrease as the external magnetic field decreases, leading to stronger attenuation of the CSWBs. This reduction in group velocity may be even more pronounced as the anticrossing regime is approached at lower external magnetic fields.

Analysis of Beam Parameters $\theta_{\mathrm{v,e}}$, k_e, and φ_e

The beam properties are further analyzed by extracting the beam parameters $\theta_{\mathrm{v,e}}$, k_e, and φ_e for the beams labeled I_free, I_I, R_I, and R_II in Fig. 6.12(h) (cf. Appendix A). The results are illustrated in Figs. 6.15(a)-(c).[7] If no parameters are displayed for a beam at a given

---

[6] Projected into the first quadrant.

[7] To better compare with the caustic model, potential deviations of the external magnetic field direction are taken into account in the error bars. This is done by considering the deviations in beam parameters between the I_free and I_I. Fig. 6.12(a) was excluded from the analysis.

external magnetic field, it indicates that the algorithm failed to detect the beam accurately or that no beam was visible in the first place.

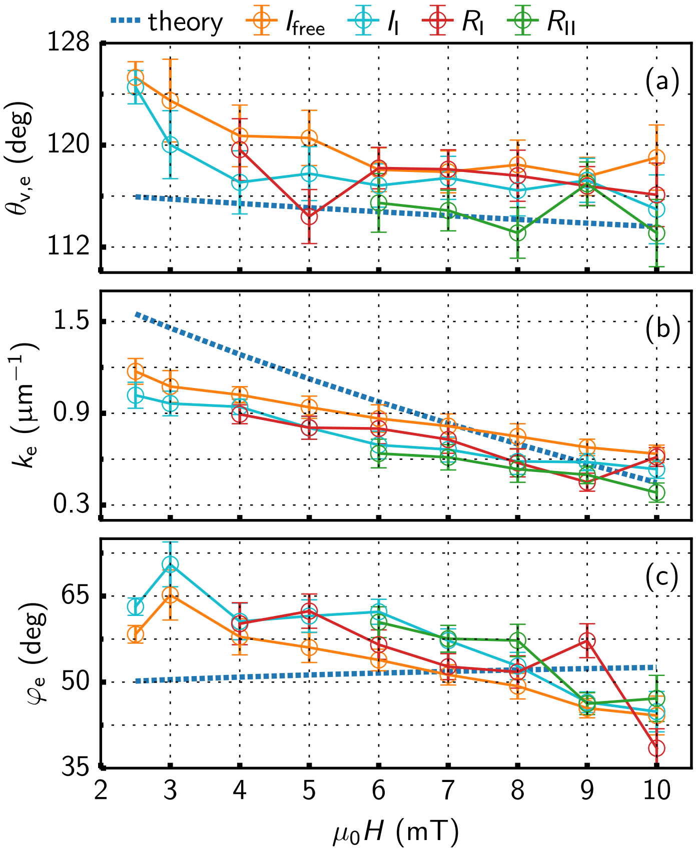

Figure 6.15. Experimental beam parameters of the beams I_{free} (orange) and I_{I} (cyan) emitted from the antenna and the reflected beams R_{I} (red) and R_{II} (green) inside the waveguide. Shown are: (a) $\theta_{\text{v,e}}$, (b) k_{e}, and (c) φ_{e}. The dashed blue lines represent the caustic point properties as predicted by the theoretical model for comparison.

Overall, the beam parameters of the different beams mostly lie within error bars and align well with the caustic model, supporting the caustic nature of the reflected beams. The stronger deviations to the predicted caustic points observed at high external magnetic fields are attributed to the beam sharpness. The pronounced deviations at low external magnetic fields (2 mT and 3 mT) are due to the system approaching the hybridization regime as the external magnetic field decreases, rendering the thin film approximation less valid.

The beam I_{free} tends to exhibit a slightly larger beam angle than I_{I}, and a similar angle mismatch is observed between the reflected beams R_{I} and R_{II}, with R_{I} having a slightly larger angle. This suggests a small misalignment of the external magnetic field angle from the x-direction. A fitting procedure applied to the FT data, as detailed in Appendix B, determined an external magnetic field angle of $\alpha_H = (-2.4 \pm 0.1)°$.

Analyis of Reflection Amplitudes and Reflection Efficiency

To analyze the reflection efficiency the amplitudes A_{fit} of beams I_{free}, I_{I}, R_{I}, and R_{II}, separately extracted from the fitting procedure, are displayed in Fig. 6.16(a).

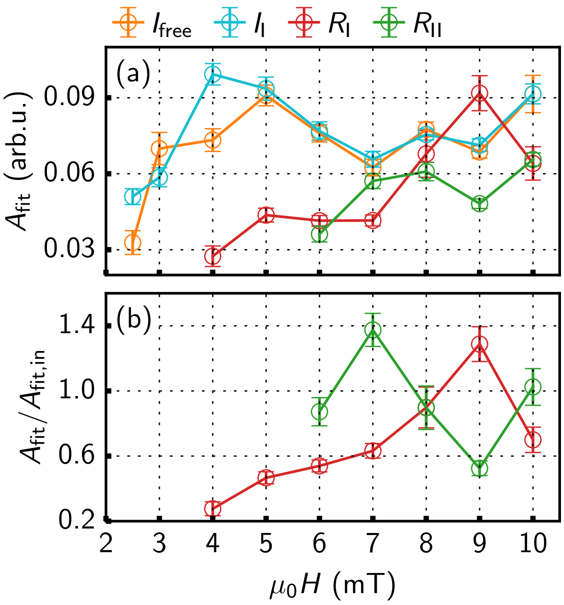

Figure 6.16. (a) Amplitudes of beams I_{free}, I_{I}, R_{I}, and R_{II}. (b) Reflection rates for first and second reflection. The reflection rate is defined as the ratio of amplitude between the incoming and the reflected beam at the YIG edge.

The amplitudes of the beams I_{free} and I_{I} directly emitted from the antenna vary slightly with the external magnetic field between $\mu_0 H = 4\,\mathrm{mT}$ and $\mu_0 H = 10\,\mathrm{mT}$, without a clear trend. Below $\mu_0 H = 4\,\mathrm{mT}$, the amplitude tends to decrease due to increased damping associated with hybridization effects. The difference between the amplitudes of beams I_{free} and I_{I} is negligible between $\mu_0 H = 5\,\mathrm{mT}$ and $\mu_0 H = 10\,\mathrm{mT}$, suggesting similar excitation efficiencies from the antenna for both beams. However, at $\mu_0 H = 4\,\mathrm{mT}$ an amplitude mismatch is noted, reminiscent of the observations in Section 6.1.

The amplitudes of the reflected beams R_{I} and R_{II} tend to be lower than those of the beams directly emitted from the antenna, especially at lower external magnetic fields, and generally tend to decrease as the external magnetic field decreases. Notably, R_{I} exhibits a sharp maximum at $\mu_0 H = 9\,\mathrm{mT}$, where its amplitude even exceeds that of the incoming beam I_{I}. This observation may be due to background artifacts excited from the edge, particularly within the waveguide, where interference between the beams and background signals is possible. This caveat should always be kept in mind when analyzing the amplitudes within the waveguide.

Nevertheless, the reflection properties are further analyzed by means of the reflection efficiency or rate in Fig. 6.16(b). In this figure, the amplitudes of the reflected beams R_{I} and R_{II} are normalized to their respective incident beams I_{I} and R_{I}, i.e., the quantities $A_{R_{\mathrm{I}}}/A_{I_{\mathrm{I}}}$ and $A_{R_{\mathrm{II}}}/A_{R_{\mathrm{I}}}$ are displayed. The efficiency of the first reflection (red curve) fluctuates between 0.4 and 0.6 below $\mu_0 H = 8\,\mathrm{mT}$, reaches near unity at $\mu_0 H = 8\,\mathrm{mT}$, and exceeds 1.0 at $\mu_0 H = 9\,\mathrm{mT}$, likely due to background effects, as previously discussed. At $\mu_0 H = 10\,\mathrm{mT}$, the efficiency is approximately 0.6. Below $\mu_0 H = 4\,\mathrm{mT}$, no reflected beam was sufficiently detectable. For the second reflection (green curve), maximum efficiency is observed at $\mu_0 H = 7\,\mathrm{mT}$, exceeding 1. At $\mu_0 H = 6\,\mathrm{mT}$ and $\mu_0 H = 8\,\mathrm{mT}$, the reflection efficiency is close to unity, while at $\mu_0 H = 10\,\mathrm{mT}$, it is around 0.7. Below $\mu_0 H = 6\,\mathrm{mT}$, no reflected beam R_{II} was sufficiently detectable.

As mentioned, the variation in background within the waveguide impacts the extracted reflection efficiency. Another factor to consider is mode quantization due to the finite width of the magnonic waveguide. The finite width introduces discretization of the wavenumber along the waveguide's width (in the y-direction), as discussed in Section 3.2. If the wave vector components k_y contributing to the beam do not sufficiently match the waveguide mode, efficient propagation within the waveguide is suppressed. Mismatched wavenumber modes experience stronger attenuation, filtering portions of wavefront angles that contribute to the CSWB. Particularly, if there is a slight angular mismatch between the incoming beam and the outgoing caustic beam, the beam-induced point-like source excitation at the edge may not sufficiently excite all the wavefront angles contributing to the reflected caustic beam.

Fig. 6.17(a) presents the predicted wave vector components k_y of the caustic points and compares them to the waveguide modes $k_{y,m} = \frac{m\pi}{w_{\mathrm{wg}}}$ (grey dashed lines) for $m = 0, 1, 2, \dots$ and $w_{\mathrm{wg}} = 40, \mu\mathrm{m}$. The predicted values have been adjusted for the external magnetic field offset α_H. The "+" symbols correspond to the predicted values for beams I_{free} and R_{I}, while the "-" symbols correspond to the predicted values for beams I_{I} and R_{II}.

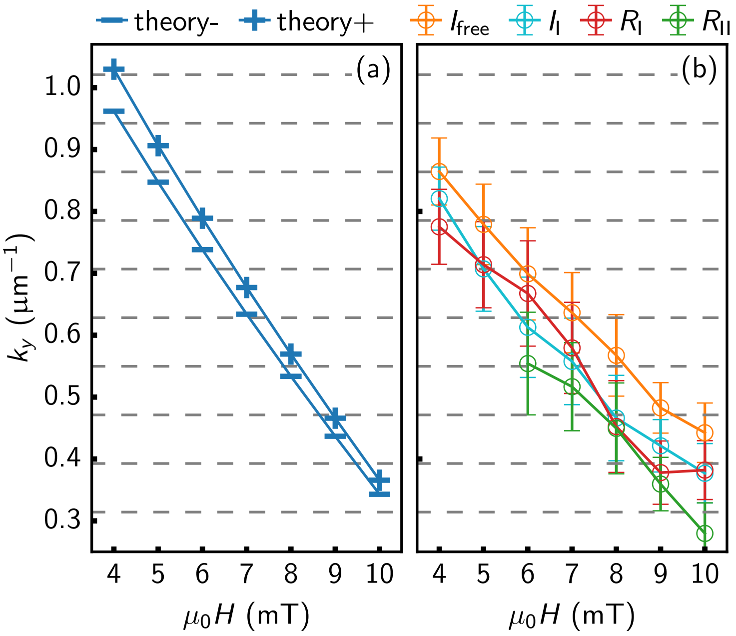

Figure 6.17. Comparison of the k_y component of the beams with the waveguide modes (grey dashed lines). (a) Predicted k_y of the caustic points considering the external magnetic field offset α_H in the experiments. The "+" symbols correspond to the predicted values for beams I_{free} and R_{I}, the "-" symbols to beams I_{I} and R_{II}. (b) Wave vector component k_y extracted for each beam from the experimental data.

At $\mu_0 H = 9\,\mathrm{mT}$, the overall discrepancy between the predicted k_y values for the beams R_{I}, I_{I}, and R_{II} is still relatively small. Specifically, the predicted k_y for the reflected beam R_{I} closely matches the waveguide mode, whereas the incident beam I_{I} and the second reflected beam R_{II} exhibit slight deviations. This alignment for R_{I} may explain the higher reflection efficiency observed in Fig. 6.16(b) at $\mu_0 H = 9\,\mathrm{mT}$. In contrast, the opposite behavior is observed at $\mu_0 H = 7\,\mathrm{mT}$, where the reflection efficiency decreases. At $\mu_0 H = 8\,\mathrm{mT}$, the predicted k_y values align closely with the waveguide modes for all beams, leading to high reflection efficiencies for both R_{I} and R_{II}. However, as the external magnetic field decreases further, larger discrepancies in k_y emerge, which may result in increased filtering of wave vector components that contribute to the reflected beams.

Fig. 6.17(b) shows the extracted k_y components from the experimental data. Notably, the beams within the waveguide consistently exhibit lower k_y values compared to beam I_{free}. This observation may indicate a filtering effect due to mode mismatch. However, the error bars are much larger than the spacing between the waveguide modes, suggesting that the presence of an exact mismatch should be interpreted with caution. More clarity could be provided by bigger mode spacing, hence a smaller waveguide width. However, for low-frequency pocket CSWBs, the reduced beam length makes it difficult to analyze wavefronts effectively. Achieving this with higher wavenumber caustic points and corresponding smaller excitation sources may be possible.

At this point, the author would like to point out that the experiments presented in this section closely resemble the phenomenon of total internal reflection. In such processes, the Goos-Hänchen (GH) shift is a factor to consider [177]. The GH shift refers to a small lateral displacement of the reflected beam along the interface, relative to the point where the incident beam meets the reflection interface. This shift occurs in the plane parallel to the interface and is related to the interaction with the evanescent wave generated at the interface during total internal reflection [178, 179].

For pure spin wave beams, a GH shift has been theoretically predicted [167–169]. However, these shifts are expected to be on the order of tens of nanometers, which is well below the resolution limit of the current experimental setup. Moreover, detecting such a phenomenon is further complicated by the physical characteristics of the magnetic material's edge. As will be discussed in Section 8.5, the edges produced through the described fabrication processes exhibit a height gradient over a lateral distance of approximately one to two micrometers; yet sharp edges are essential for observing such small spatial shifts.

Additionally, the GH shift manifests as a phase shift upon reflection at the edge, a phenomenon that has been experimentally demonstrated for plane spin waves [180]. However, analyzing the phase shift in the presented experiments is challenging. The imperfect YIG edge complicates the accurate determination of the reflection region. The finite width of the CSWBs introduces additional complexity, as the sharpness of the beam is not well-defined, further affecting the identification of the reflection point at the waveguide edge. Even a slight misalignment of the reflection edge by a few pixels can already cause a phase shift in the analysis. Furthermore, because the caustic beam is composed of multiple k-vectors, the phase shift is not ambiguous. The outer regions of the CSWB may exhibit different wavelengths compared to the inner regions, potentially resulting in a non-uniform phase shift across the beam width.

An attempt to analyze the phase shift upon reflection of the CSWBs is presented in Appendix C. However, due to the factors mentioned above, a detailed exploration of the GH shift seems to be impossible.

6.4.2. Angular Dependence of Reflection

The reflection of the beams was also examined under various external magnetic field angles. Figures 6.18(a)-(f) present the Kerr maps for different angles at an excitation frequency of

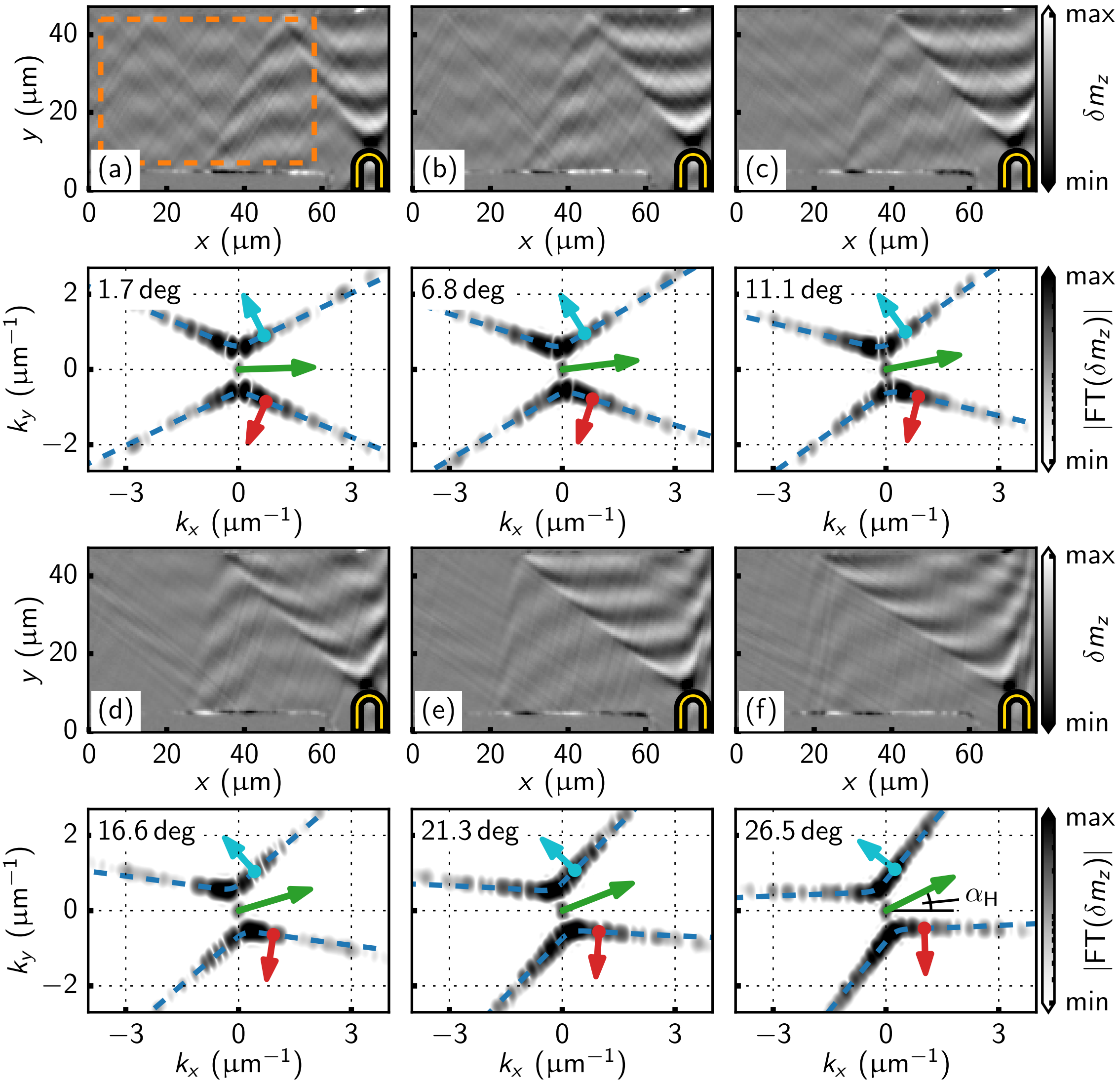

Figure 6.18. (a)-(f) Reflection as a function of external magnetic field angle α_H with $f = 1.44\,\mathrm{GHz}$ and $\mu_0 H = 5\,\mathrm{mT}$. All Kerr maps in the upper row are normalized to the same color scale. The lower row depicts FT data in a logarithmic scale obtained from the orange region in the Kerr map. The angle of α_H, extracted from a fitting procedure, is displayed in the FT plot. The green arrow represents the corresponding direction of the external magnetic field. The blue dashed curve depicts the rotated iso-frequency curve, while cyan- and red-colored arrows correspond to the group velocity directions at the predicted caustic points.

$f = 1.44\,\mathrm{GHz}$ and an external magnetic field of $\mu_0 H = 5\,\mathrm{mT}$. The corresponding FT data, extracted from the area within the orange rectangle, is shown below each map. This data includes the reconstructed iso-frequency curves and the predicted group velocity directions of the incoming and reflected caustic beams. The external magnetic field angles α_H were determined through a fitting procedure applied to the FT data (see Appendix B).

Firstly, as the external magnetic field angle increases, the beam angle of the beam emitted from the antenna I_I clearly increases, demonstrating the feasibility of steering CSWBs with the external magnetic field. Secondly, focussing on the reflection process, it is evident that the beam angle of the first reflected beam R_I decreases with increasing field angle, significantly deviating from the conventional law of reflection in optics, where the incident angle equals the reflected angle. This deviation is also observed in the reflection at the lower edge, which is faintly visible in some of the Kerr maps. Furthermore, the reflection efficiency appears to decrease as the external magnetic field angle increases.

The observed beam directions closely align with the predicted group velocity directions originating from the caustic points, as visualized by the cyan-colored (I_I) and red-colored arrows (R_I) in the FT data. This alignment underscores that the reflection of CSWBs is governed by the transition between caustic points located in different quadrants of the iso-frequency curve as illustrated in Figs. 6.10(a)-(c).

This conclusion is further supported by the analysis of the beam parameters presented in Figs. 6.19(a)-(c). In this analysis, only the beam emitted from the antenna and its first reflection were considered. Fig 6.19(a) shows that the beam direction $\theta_\mathrm{c,e}$ of the incident beam I_I (cyan curve) increases with the external magnetic field angle, with the increment in beam direction closely matching the increment in the external magnetic field angle. Conversely, the beam direction of the reflected beam R (red line) decreases by the corresponding negative increment. Notably, the average of the two beam directions (brown curve) aligns well with the predicted caustic beam direction when $\alpha_H = 0^\circ$ (dashed blue line). A similar pattern is observed in the wavefront angles in Fig 6.19(c). The wavenumbers of incident and reflected beam (Fig 6.19(b)) exhibit no obvious trend but appear to remain relatively constant across all beams, reasonably aligning with the predicted caustic wavenumbers. These observations validate the caustic nature of the observed reflection phenomena.

The beam amplitudes were also analyzed and are depicted in Fig.6.20(a). The amplitude of the incoming beam I_I exhibits slight variations with the external magnetic field angle, likely due to interactions with parasitic backgrounds excited by the patterned edges. These interactions are more pronounced in the low-angle maps shown in Figs.6.18(a)-(f). In contrast, the amplitude of the reflected beam R_I decreases as the external magnetic field angle increases. This trend is further illustrated by the reflection efficiency presented in Fig. 6.20(b), which declines with increasing external magnetic field angle.

While filtering effects due to the width modes of the waveguide, as discussed in Section 6.4.1, may contribute to the reflection efficiency, the primary factor is the mismatch between the external magnetic field direction and the reflection edge itself. This mismatch leads to differing angular spectra between the incoming and outgoing wave packets [44], resulting in less efficient excitation of the reflected caustic point at the edge as the external magnetic field angle increases.

To conclude this section, the experimental data is compared with Snell's law as applied to the reflection of spin waves. For this analysis, the predicted wavenumbers and wavefront

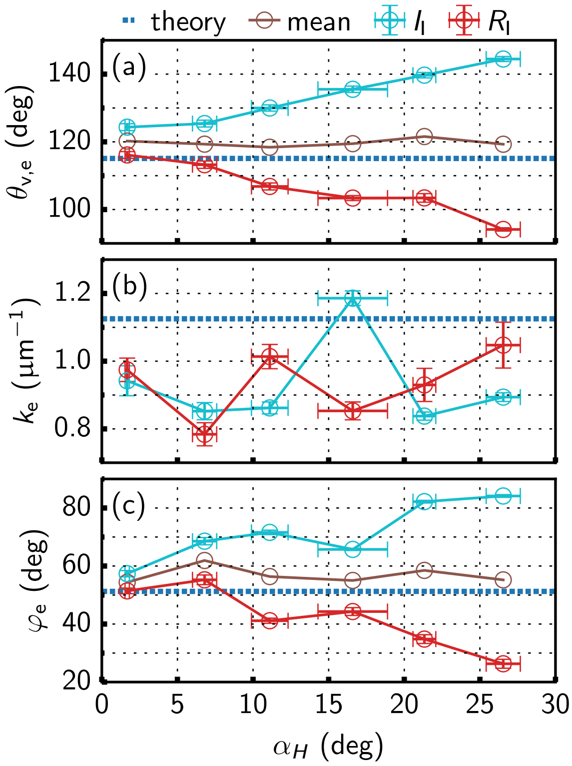

Figure 6.19. Beam parameters (a) $\theta_{\mathrm{v,e}}$, (b) k_e, and (c) φ_e of incoming (cyan dots) and first reflected beam (red dots) at different external magnetic field angles α_H. The dashed blue line represents the predicted CSWB features when $\alpha_H = 0°$, whereas brown dots represent the mean values of the incident and reflected beam. The error bars in α_H correspond to the standard deviations of a fitting procedure.

angles of the incoming beams were used to calculate the properties of the reflected wave from the geometrical considerations of Snell's law on the iso-frequency curve (see Fig.6.9). The comparison with the experimentally observed reflected beam R_I is presented in Figs. 6.21(a) and (b).

Notably, Snell's law predicts a decrease in the wavenumber of the reflected wave. In contrast, the experimental data from the caustic spin wave beam experiments suggest that the wavenumber remains relatively constant. An even more pronounced discrepancy is observed in the wavefront angles φ; Snell's law predicts a monotonically increasing wavefront angle for the reflected wave, while the experimental wavefront angle actually decreases.

This comparison underscores the differences between the reflection behavior of pure spin waves and caustic spin wave beams. According to Snell's law for spin waves, the reflected wave vector generally does not correspond to a caustic point, except in the specific case where $\alpha_H = 0$. The emission and reflection of caustic spin wave beams, however, rely on a stationary group velocity direction, which occurs at a caustic point.

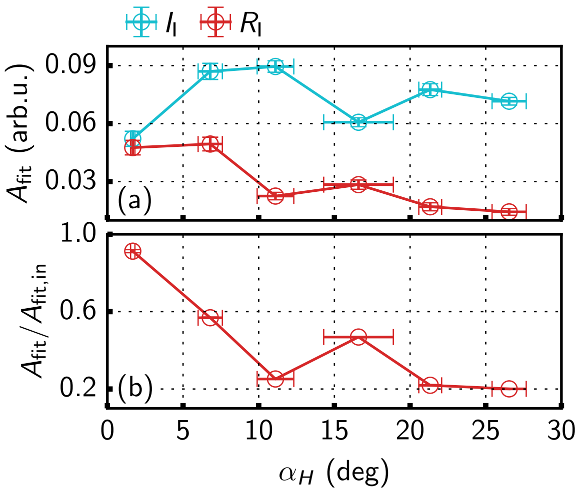

Figure 6.20. (a) Amplitudes of incoming beam I_I and reflected beam R_I as a function of the external magnetic field direction. (b) Corresponding reflection efficiencies.

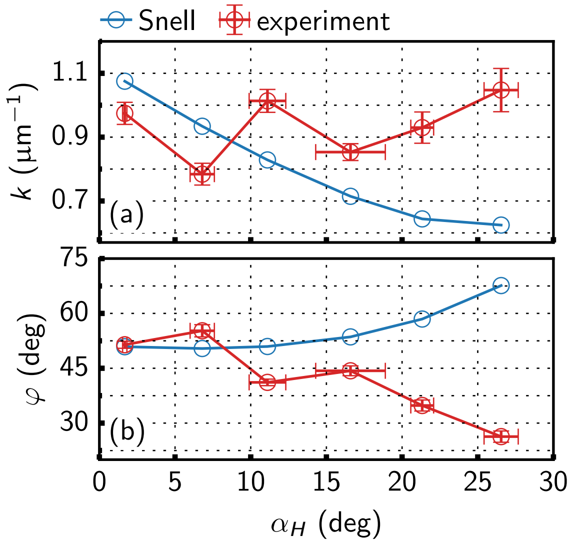

Figure 6.21. Comparison of the experimental (a) wavenumber and (b) wavefront angle of the reflected beam (red) with predictions based on Snell's law (blue). The reflection behavior of caustic spin wave beams does not adhere to Snell's law for spin waves.

Part III.

Spatial Control of Hybridization-Induced Spin Wave Stop Band

Many of the discussions and findings in this part are published in [176].

7. Motivation and Experimental Design

In Ref. [34], it was experimentally demonstrated that within a 200 nm thick YIG film, spin wave propagation is highly suppressed at an excitation frequency of $f = 2.8\,\text{GHz}$ around an external magnetic field of $\mu_o H = 32\,\text{mT}$. This suppression was attributed to the mode hybridization between the zeroth-order DE mode and the first-order PSSW mode. Furthermore, it was observed that upon launching spin waves towards a 1D diffraction grating composed of antidots in the YIG film, no spin wave signal was transmitted for certain external magnetic field values. This phenomenon was attributed to a geometry-dependent reduction of the internal magnetic field in the sections between the antidots in order to avoid magnetic surface charges [64, 167, 181]. This field reduction forced the DE modes to enter the hybridization regime in-between neighboring antidots and, hence, into a regime of high spin wave attenuation.

By exploiting these two effects—the hybridization-induced spin wave stop band and the geometry-induced variation of the internal effective magnetic field—the stop position of propagating spin waves should also be smoothly controllable rather than being limited to an abrupt stop at the position of the antidot grating. This control can be achieved by tuning the external magnetic field within a properly designed magnetic structure. A suitable structure for this purpose may be a waveguide that gradually decreases in effective magnetic field along the spin wave propagation direction.

A sketch of the measurement geometry is shown in Fig. 7.1. A trapezoidal (or tapered) waveguide was patterned from a 200 nm thick full YIG film by means of optical lithography and subsequent Argon etching of the film. The trapezoid gradually decreases from a width w_1 to a width w_2 along a length l. Default values, unless specified otherwise, are $w_1 = 30\,\mu\text{m}$, $w_2 = 5\,\mu\text{m}$ and $l = 80\,\mu\text{m}$. In order to minimize reflections, a gradual continuation from the trapezoid shape back to the full film was implemented. For the excitation of spin waves, a CPW with $w_{\text{sig}} = 10\,\mu\text{m}$, $w_{\text{gr}} = 5\,\mu\text{m}$ and $w_{\text{gap}} = 5\,\mu\text{m}$ was fabricated on top of the YIG film by optical lithography and electron beam evaporation of Ti(5 nm)/Au(210 nm). In the experiments, spin waves in the DE geometry were launched from the full film into the transversely magnetized trapezoidal waveguide.

To gain insight into the influence of the trapezoidal shape on the effective magnetic field, micromagnetic simulations utilizing MUMAX3 [66] were performed[1]. In Fig 7.2(c), the spatial distribution of the x-component $\mu_0 H_{x,\text{eff}}$ of the effective magnetic field is shown at an applied static magnetic field of $\mu_0 H = 33.5\,\text{mT}$. Within the trapezoid, the effective magnetic field exhibits local variations and is notably reduced at the edges of the patterned YIG. The inhomogeneous spatial field distribution is further highlighted by the sketched iso-field lines

---

[1] A grid of $1000 \times 4400 \times 4$ was used in the simulation. The cell dimensions were chosen to be 50 nm in all 3 dimensions.

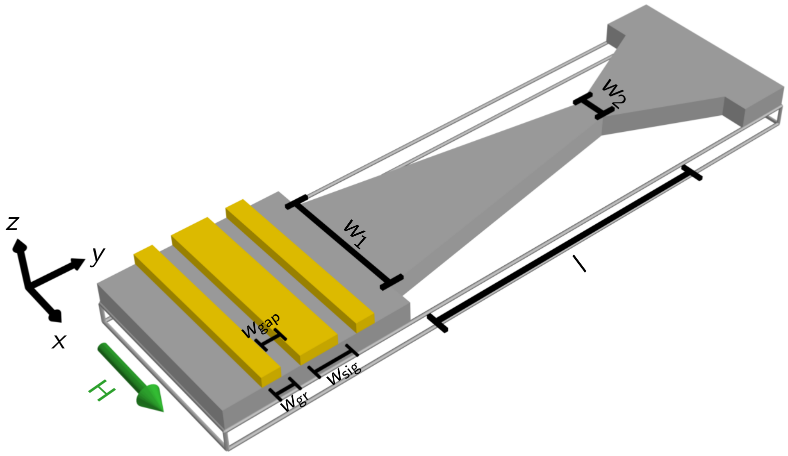

Figure 7.1. Sketch of sample and measurement geometry. In the experiments, spin waves in the dipolar regime are excited by a coplanar waveguide (golden cuboids) and are directed toward a trapezoidal structure in the Damon-Eshbach geometry. The coplanar waveguide dimensions are $w_{\text{sig}} = 10\,\mu\text{m}$, $w_{\text{gr}} = 5\,\mu\text{m}$ and $w_{\text{gap}} = 5\,\mu\text{m}$. If not stated otherwise, $w_1 = 30\,\mu\text{m}$, $w_2 = 5\,\mu\text{m}$ and $l = 80\,\mu\text{m}$. The grey layer represents the patterned YIG, and the transparent layer represents the GGG substrate. A static external magnetic field along the x-direction was applied throughout the experiment, as indicated by the green arrow.

(black lines), which display rounded triangular-like features within the trapezoid. Across the trapezoid's width (Fig. 7.2(b)), sharp dips of the effective magnetic field occur at the edges, leading to a gradual decrease in the effective magnetic field along the direction of spin wave propagation (Fig. 7.2(a)). This inhomogeneity of the effective magnetic field stems from the geometry-induced demagnetizing field, which aims to avoid the formation of magnetic surface charges [64, 167].

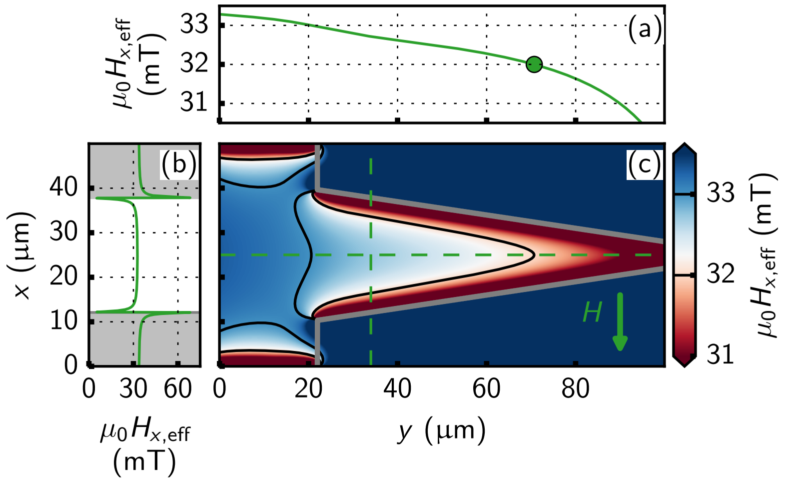

Figure 7.2. Effective magnetic field distribution within the trapezoid. The external magnetic field was applied along the x-direction, as indicated by the green arrow. (a) The x-component of the effective magnetic field (extracted along the horizontal green dashed line in (c)) decreases gradually along the waveguide's length. The green dot marks the hybridization field for full film YIG at 2.8 GHz. (b) Across the width of the trapezoid (vertical green dashed line in (c)), pronounced reductions in effective magnetic field are observed at the edges. Grey-shaded regions indicate areas outside the magnetic medium. (c) Spatial map showing the inhomogeneous distribution within the transversely magnetized trapezoid.

8. Experimental Results

8.1. Spin Wave Stop Band in 200 nm thick Full YIG Film

In the first set of experiments, spin wave propagation in the 200 nm thick YIG full film is investigated in order to validate the presence of hybridization-induced attenuation effects.

In this context, spin waves in full film YIG are excited at a constant frequency of $f = 2.8\,\mathrm{GHz}$ in the DE geometry and detected far away from any patterned magnetic structure by TR-MOKE microscopy. Fig. 8.1(a) shows the corresponding line profiles of the dynamic out-of-plane magnetization as a function of the applied external magnetic field. The grey-scale represents the detected Kerr signal. Following the dispersion relation, the wavelength increases with increasing magnetic field. However, a clear suppression of spin wave propagation occurs around $\mu_0 H = 32\,\mathrm{mT}$ within a narrow region of the external magnetic field range.

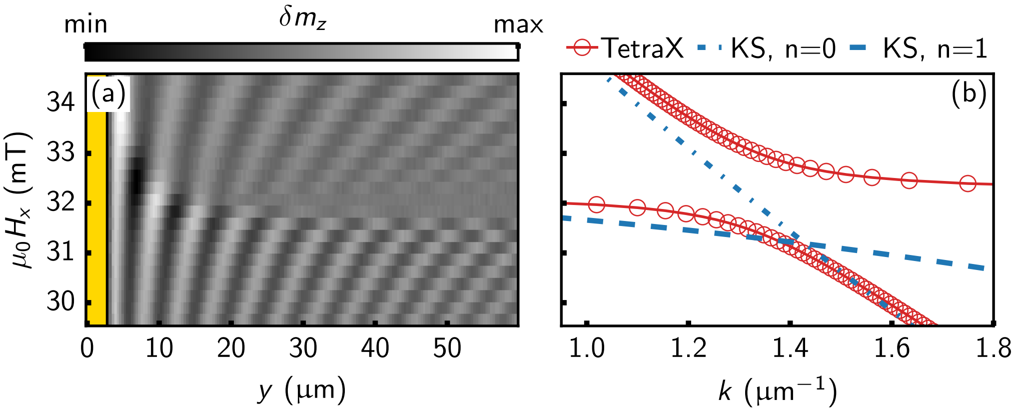

Figure 8.1. Hybridization-induced spin wave stop band in a 200 nm thick YIG film at an excitation frequency of $f = 2.8\,\mathrm{GHz}$. (a) Spin wave propagation excited in the DE geometry by a coplanar waveguide (ground line indicated by golden region) as a function of the external magnetic field. A suppression of propagation is observable around 32 mT. (b) TetraX simulation. The $n = 0$ (blue dash-dotted line) and $n = 1$ (blue dashed line) predicted by Kalinikos and Slavin (KS) hybridize and form an anticrossing in the micromagnetic simulations (red line and circles). A band of strongly attenuated propagation emerges.

In the zeroth-order KS model, the $n = 0$ and $n = 1$ modes intersect slightly below $\mu_0 H = 32\,\mathrm{mT}$ at the given experimental conditions, as illustrated in Fig. 8.1(b). This degeneracy is lifted in the micromagnetic simulations performed with TetraX by forming an anticrossing.

In this regime, the dispersion relation is flattened and the group velocity approaches zero (cf. Eq. (1.22)), leading to a significant attenuation of spin wave propagation (cf. Eq. (1.23)). Given the close match between theoretical prediction and experiment, it is concluded that the observed suppression of propagation is indeed attributed to the hybridization of the DE mode and the first-order PSSW mode. Thus, at a driving frequency of $f = 2.8\,\mathrm{GHz}$, the hybridization field lies at $\mu_0 H_{\mathrm{hyb}} \approx 32\,\mathrm{mT}$.

8.2. Propagation Profile in a Trapezoidal Waveguide

Fig 8.2(a) displays a Kerr map of the trapezoidal structure recorded with an excitation frequency of $f = 2.8\,\mathrm{GHz}$ and a static external magnetic field of $\mu_0 H = 33.5\,\mathrm{mT}$. Plane spin waves are launched from the CPW into the full film. Upon entering the trapezoid, however, the propagation profile changes. In the center of the trapezoid, a prominent mode with slightly bent wavefronts is observed. Close to the edges, a localized mode with strongly bent wavefronts is apparent.

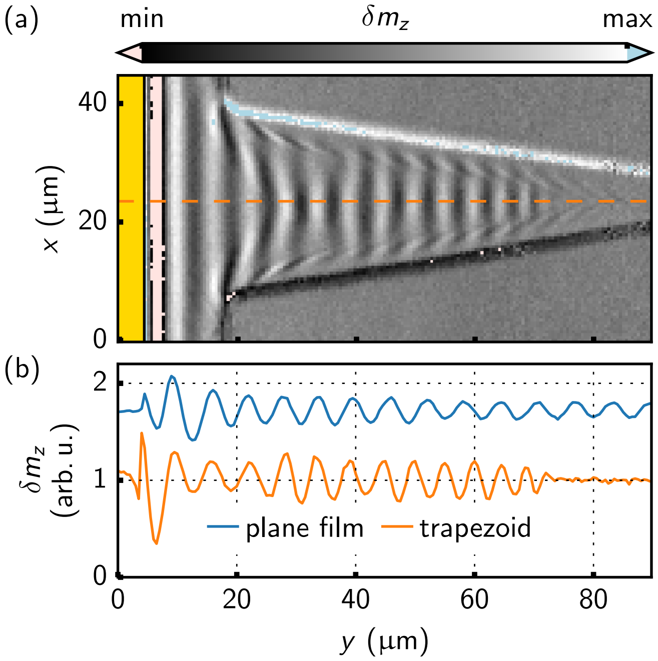

Figure 8.2. TR-MOKE measurement with $f = 2.8\,\mathrm{GHz}$ and $\mu_0 H = 33.5\,\mathrm{mT}$. (a) Spatial Kerr map. For better visibility, the contrast was increased; light red and blue indicate a saturation of the grey-scale. (b) Comparison of line profiles along the middle of the wedge (orange curve) and in non-patterned plane YIG (blue curve). The orange curve is extracted from the dashed orange line in (a). Inside the trapezoid, the propagation stops at a distinct position.

This bending of spin waves results from the inhomogeneous internal magnetic field distribution (cf. 7.2). This distribution causes local variations of the dispersion relation and, hence, of the propagation characteristics [167]. As the effective magnetic field is reduced locally, the DE dispersion relation also shifts towards lower wavelengths at the given excitation frequency. This effect is particularly pronounced in the low-field pockets in the effective magnetic field distribution at the edges of the trapezoid (cf. 7.2(b)), leading to the pronounced mode localization in this region [115, 182, 183].

More significantly, however, the center mode undergoes a change in wavelength within the trapezoid and comes to a stop at a distinct point in space. Beyond this point, spin wave propagation is nearly entirely suppressed. This behavior is further highlighted in Fig. 8.2(b) by the line profile extracted from the center of the trapezoid. An additional line scan on plane YIG, far away from any patterned structure, is provided for comparison. Upon entering the trapezoid, the wavelength gradually decreases, consistent with the corresponding simulated reduction in effective magnetic field (cf. Fig. 7.2(a)). At $y \approx 74\,\mu\text{m}$, the spin wave profile abruptly ceases, whereas, in the plane film, propagation persists beyond this distance from the antenna.

In the preceding Section 8.1, it was found that with $f = 2.8\,\text{GHz}$, the investigated YIG exhibits a hybridization-induced stop band at an external magnetic field of $\mu_0 H_{\text{hyb}} \approx 32\,\text{mT}$ in the full film configuration. From Fig. 7.2(a), it can be observed that the stop position within the wedge ($y \approx 74\,\mu\text{m}$) corresponds to an estimated effective magnetic field of $\mu_0 H_{x,\text{eff}} \approx 32\,\text{mT}$, aligning well with the measured full film hybridization condition. Thus, it is inferred that the reduction in effective magnetic field at different spatial positions leads to the local dispersion entering the hybridization regime. As a result, spin wave propagation comes to a halt at a specific position in space.

8.3. Spatial Control of Spin Wave Propagation Distance

These findings are now employed towards the active control over propagation distance within the trapezoid. Fig. 8.3 depicts Kerr images at various external magnetic fields. At an external magnetic field of $\mu_0 H = 31.5\,\text{mT}$ (Fig. 8.3(a)), the center mode propagates along the full length of the trapezoid without any sharp attenuation. In this scenario, the stop band is not reached within the geometry, given that the applied external magnetic field is already below the full film hybridization condition and only undergoes further reduction inside the trapezoid. Furthermore, a complex beating profile with a prominent node at $y \sim 45\,\mu\text{m}$ is observed. This periodic pattern results from the interference of width modes induced by the trapezoidal waveguide [184, 185] and the generation of caustic-like beams from the corners where the full film transitions into the trapezoid [26, 34]. As the caustic-like beams are reflected back and forth at the edges of the trapezoid, non-equidistant nodes of higher amplitude occur. This phenomenon was referred to as self-focussing in Ref. [184] and shall not be confused with focussing effects that lead to caustic spin wave beam emission (cf. Part II).

In Figs. 8.3(b)-(d), spin wave propagation stops at different positions in space depending on the external magnetic field strength. Also, note that the boundaries of the spin wave patterns exhibit a shape comparable to the iso-field lines of the effective magnetic field inside the trapezoid (cf. 7.2(c)). Here, the external magnetic fields lie slightly above the stop band field, and the reduction in the effective magnetic field pushes the dispersion relation into the hybridization regime along the trapezoid. Consequently, the positions where the dispersion relation locally gains access to the stop band shift further outward along the y-direction with increasing external magnetic field. In conclusion, the geometry-induced hybridization determines the stop position and enables active control over the spin-wave propagation distance by tuning the static external magnetic field close to the stop band.

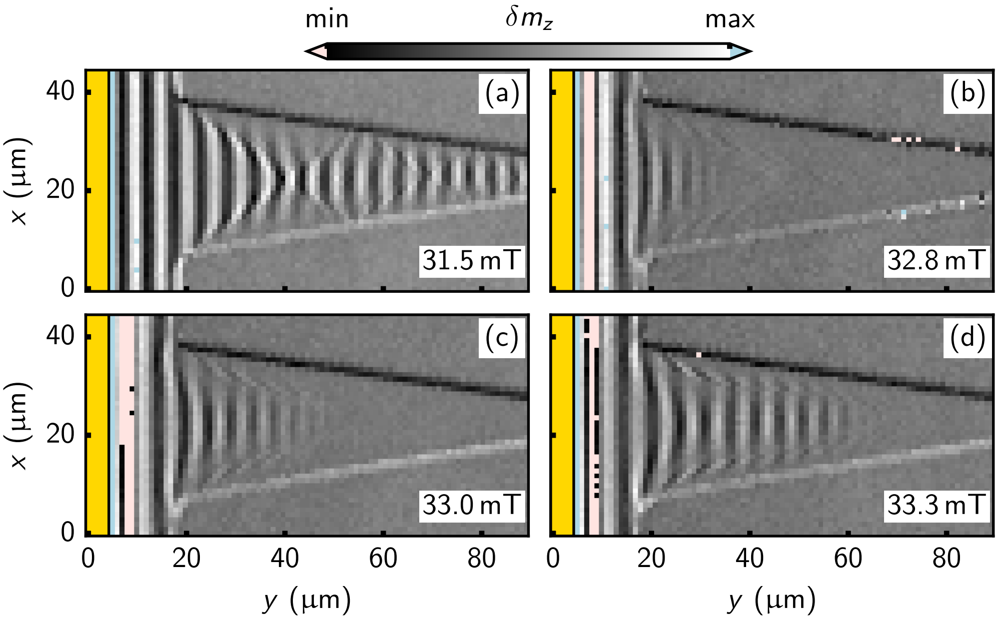

Figure 8.3. TR-MOKE images acquired at different external magnetic fields and a constant excitation frequency of $f = 2.8\,\mathrm{GHz}$. (a) Below the full film hybridization field ($\mu_0 H_{\mathrm{hyb}} \approx 32\,\mathrm{mT}$), spin waves propagate along the full length of the trapezoid. (b)-(c) Coming from external magnetic fields slightly above the stop band, the spin wave propagation vanishes at different positions in space.

Furthermore, by modifying the geometry of the trapezoidal waveguide, one can adjust the sensitivity of propagation distance control to the external magnetic field. Figs. 8.4(a)-(d) show Kerr maps close to the full film hybridization where the trapezoid structure transitions from a width of $w_1 = 30\,\mu\mathrm{m}$ to $w_2 = 5\,\mu\mathrm{m}$ over a distance $l = 200\,\mu\mathrm{m}$.

At an external magnetic field of $\mu_o H = 32.5\,\mathrm{mT}$ (Fig. 8.4), the main mode stops within a few microns of propagation within the trapezoidal waveguide. At $\mu_o H = 32.8\,\mathrm{mT}$ (Figs. 8.4(b)), the propagation distance is much larger than in the previously discussed geometry and gradually fades away. At $\mu_o H = 33\,\mathrm{mT}$ (Figs. 8.4(c)), the stop position extends even beyond the scanning range. Overall, this behavior can be attributed to the steadier reduction in the effective magnetic field along the spin wave propagation direction. Fig. 8.4(d) shows a micromagnetic simulation [66] of the effective magnetic field along the center of the waveguide (green dashed line in Fig. 8.4(b)). The overall reduction in the effective magnetic field over the given y-range is much smaller than in Fig. 7.2(a). Thus, the hybridization condition is reached at a more distant position in space along the waveguide in comparison, and a fixed increase in the external magnetic field results in a correspondingly larger increase in the spin wave propagation distance.

Furthermore, in the vicinity of the transition area from the full film to the trapezoidal waveguide, the effective magnetic field exhibits a steeper decrease than in the rest of the

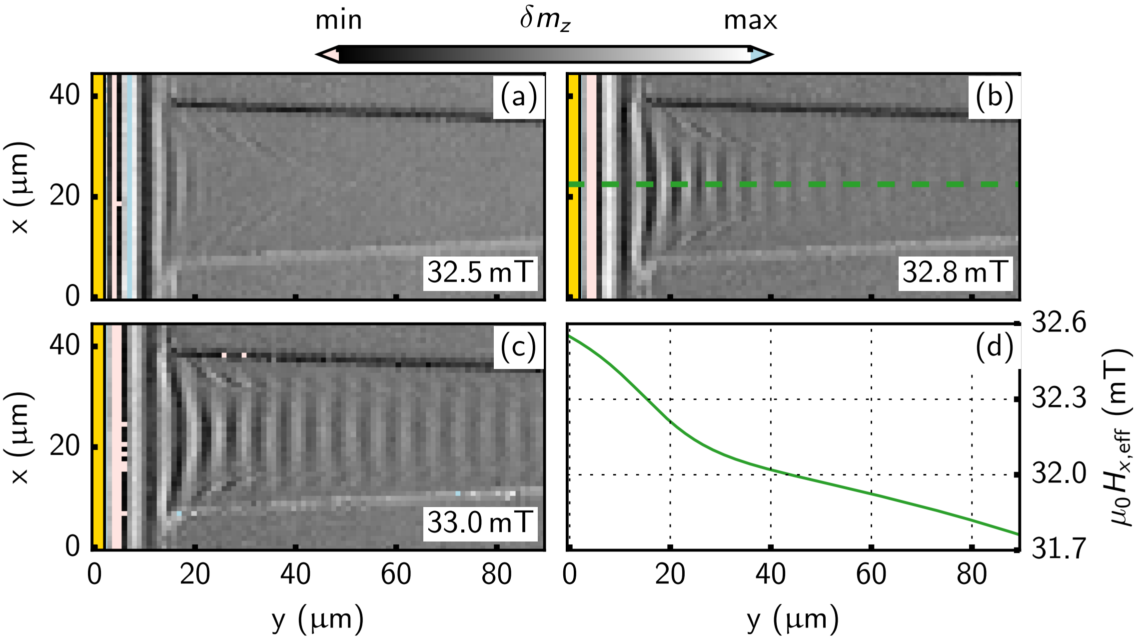

Figure 8.4. (a)-(c) Kerr images at different fields with $f = 2.8\,\mathrm{GHz}$. The trapezoid has the following dimensions (cf. Fig. 7.1): $w_1 = 30\,\mu\mathrm{m}$, $w_2 = 5\,\mu\mathrm{m}$, and $l = 200\,\mu\mathrm{m}$. The field window in which the propagation distance can be controlled is much smaller compared to the steeper trapezoidal waveguide. (d) Effective magnetic field simulation at an external magnetic field of $\mu_0 H = 32.8\,\mathrm{mT}$ along the green dashed line in (b).

depicted waveguide. This results in a more abrupt stop of propagation when the hybridization is reached in the transition area (Fig.8.4(a)), whereas in the case of $\mu_0 H = 32.8\,\mathrm{mT}$ (Fig.8.4(b)), spin wave propagation gradually disappears.

8.4. Transmission Control between Microstrip Antennas

In this section, the geometry-induced hybridization is utilized to gain control over the electrical transmission between several microstrip. Fig. 8.5 shows a sketch of the experimental configuration. Three 800 nm wide gold microstrips were deposited at different positions along the patterned YIG film. Each of the microstrips was connected to a different port of a four-port *Agilent N5222A* vector network analyzer (VNA) and all-electrical spin wave spectroscopy measurements (cf. Section 2.3) were carried out. The microstrip connected to port 1 served as a source of excitation for spin waves, while microstrips 2 and 3 were employed for detection. Note that microstrips were chosen instead of CPWs since they provide a more continuous excitation and detection range of wave vectors (cf. Section 1.4), making them more suitable for broadband spectroscopy. All measurements were conducted at a microwave power of 3 dBm, and the real and imaginary parts of the transmission parameters S_{21} and S_{31} were recorded.

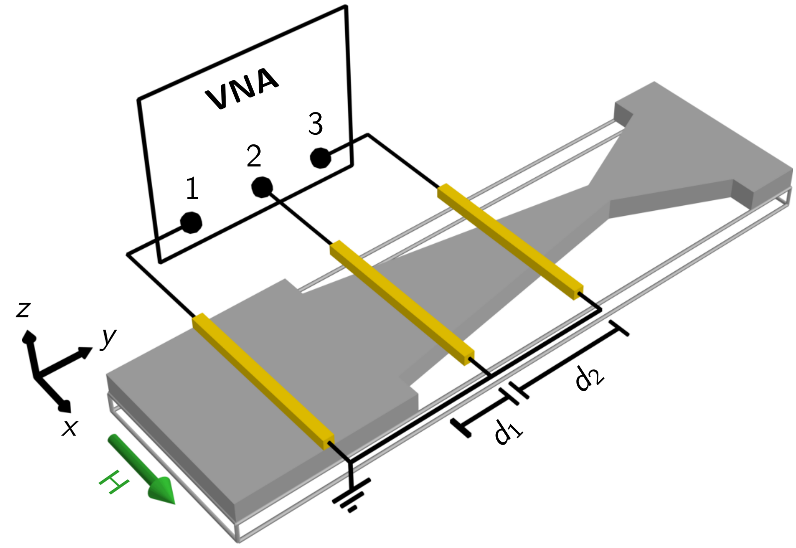

Figure 8.5. Sketch of all-electrical broadband spin wave spectroscopy measurement. Three microstrip antennas distributed along the sample geometry ($d_1 = 15\,\mu\text{m}$, $d_2 = 34\,\mu\text{m}$) are connected to separate ports 1, 2 and 3 of a VNA. Spin waves are excited from antenna 1 and detected along the trapezoid by antennas 2 and 3.

Figure 8.6. Transmission spectra of $|\Delta S_{21}|$ and $|\Delta S_{31}|$. Modes close around FMR are prominent (white contrast), yet transmission over a broad range of external magnetic fields and excitation frequencies is observable.

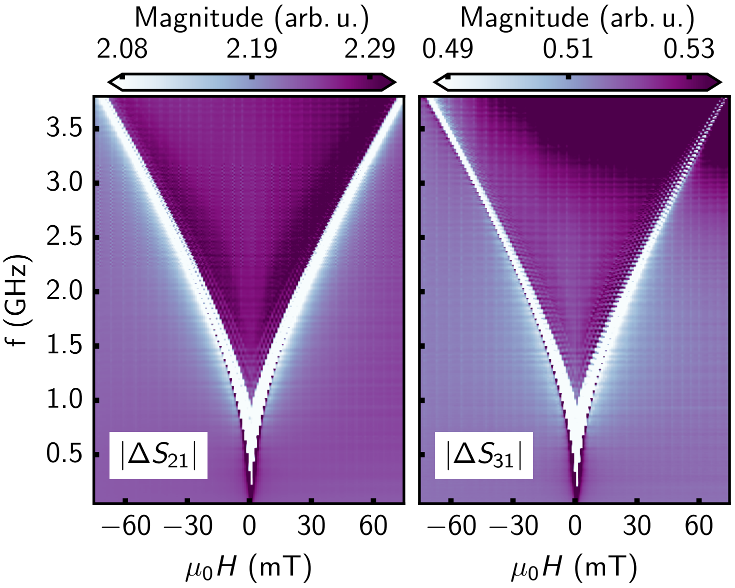

In Fig. 8.6, broadband spectra of the amplitude of the transmission parameters are displayed. Here, the external magnetic field was incrementally changed in 5 mT steps from high to low fields, and the spin wave excitation frequency was swept at each external magnetic field value. High external magnetic field reference data was recorded at $\mu_0 H_{\text{ref}} = 200\,\text{mT}$ and subtracted, and the resulting transmission parameters are presented in terms of $|\Delta S_{21}|$ and $|\Delta S_{31}|$ (cf. Section 2.3). Both spectra exhibit pronounced contrast for modes around the FMR, but transmission over a broad range of external magnetic fields and excitation frequencies, and hence wave vectors occurs. The contrast and magnitude of the $|\Delta S_{21}|$ spectrum is larger since spin waves are further damped when propagating towards microstrip 3. Furthermore, the transmission efficiency appears to be higher for positive external magnetic field values, which may result from non-reciprocity in antenna excitation and detection, non-reciprocal surface localization of the DE modes, or, most likely, a combination of these two factors.

Figs. 8.7(a) and (b) show further spectra with enhanced resolution in the vicinity of the hybridization condition at positive external magnetic fields. Both, the $|\Delta S_{21}|$ and the $|\Delta S_{31}|$ data, exhibit oscillations in magnitude, which can be attributed to changes in lateral spin wave profile. The variation in magnetic field and applied frequency alters the width-induced self-focussing conditions, shifting the positions of high amplitude and caustic-like nodes [184]. In the $|\Delta S_{31}|$ transmission, the spacing between these oscillations is shorter. This results from the gradual decrease in trapezoid width, leading to a smaller node spacing in the external magnetic field domain at the position of the third microstrip compared to the location of microstrip 2.

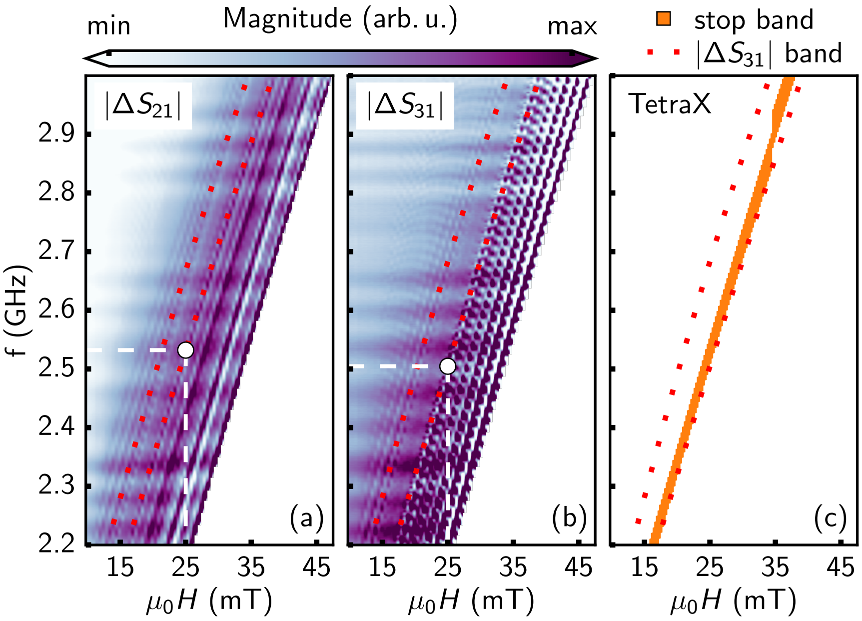

Figure 8.7. Transmission spectra of (a) $|\Delta S_{21}|$ and (b) $|\Delta S_{31}|$ in the vicinity of the stop band. Regions with low to no transmission occur (indicated by red dotted lines as guides for the eye). The band is broader in the transmission amplitude $|\Delta S_{31}|$. At a given external magnetic field, the band forms at lower frequencies in $|\Delta S_{31}|$ (highlighted by white dashed lines). For better contrast, data in the white space region on the right is not displayed. (c) Comparison between simulated full film stop band (orange band) and experimental band from (b).

Moreover, distinct wide regions with low to no transmission where the oscillatory behavior is suppressed are observed and highlighted by red dotted lines in both spectra. The bands extracted show good qualitative agreement with the expected full film stop band conditions calculated by TetraX as illustrated in Fig. 8.7(c), where the band extracted from $|\Delta S_{31}|$ is compared to the simulation (orange band). One notable difference, however, is the broader width of the experimental data which will be explained later. Nevertheless, it is valid to conclude that these regions of lower transmission indeed correspond to the spin wave stop band induced by the hybridization of the DE-like mode with the first PSSW mode.

In the $|\Delta S_{31}|$ data, the stop band spans over a broader range compared to the $|\Delta S_{21}|$ spectrum and is reached at lower excitation frequencies at a given external magnetic field (illustrated by white dashed lines). This directly results from the spatially varying stop position of the spin waves. As spin waves advance further along the trapezoid, the effective magnetic field is further reduced, facilitating access to the anticrossing regime. This, in turn, leads to a suppression of transmission between the VNA channels over a broader range of external magnetic fields and excitation frequencies as the excitation and detection microstrips move farther apart. An analogous reasoning applies to the difference in width between experimental data and full film simulation (Fig. 8.7(c)).

To put the experimental findings differently, distinct external magnetic field and frequency conditions exist where transmission is absent in both $|\Delta S_{21}|$ and $|\Delta S_{31}|$, transmission is observed only in $|\Delta S_{21}|$, and transmission occurs in both $|\Delta S_{21}|$ and $|\Delta S_{31}|$. Consequently, selective control over the transmission between the microstrips can be achieved.

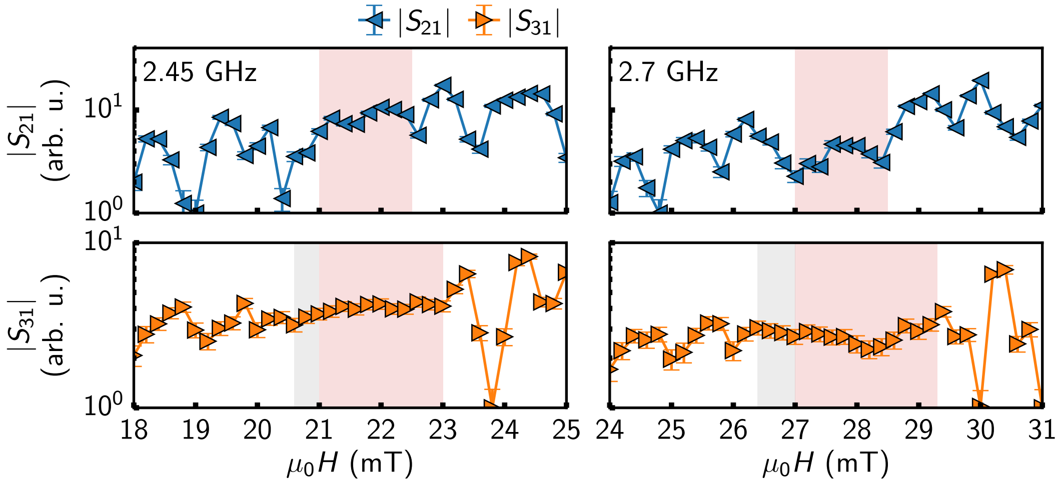

Figure 8.8. Transmission signals in CW mode at different excitation frequencies. The hybridization-induced stop band region (red-shaded areas serve as guides to the eye) spans to higher external magnetic fields in the $|S_{31}|$ trace. Additional regions of suppressed transmission occur in $|S_{31}|$ slightly below the stop band (grey-shaded region).

This is further illustrated in the CW sweeps at different excitation frequencies in Fig 8.8. Here, the transmission is represented in terms of $|S_{21}|$ and $|S_{31}|$, as no high external magnetic field reference needs to be recorded in this mode of operation. The regions of suppressed transmission due to the hybridization (highlighted by the red-shaded rectangles) shift with applied frequency and extend to higher external magnetic fields in the $|S_{31}|$ parameter due to the reduction in the effective magnetic field along the trapezoid. For instance, at $f = 2.45\,\mathrm{GHz}$

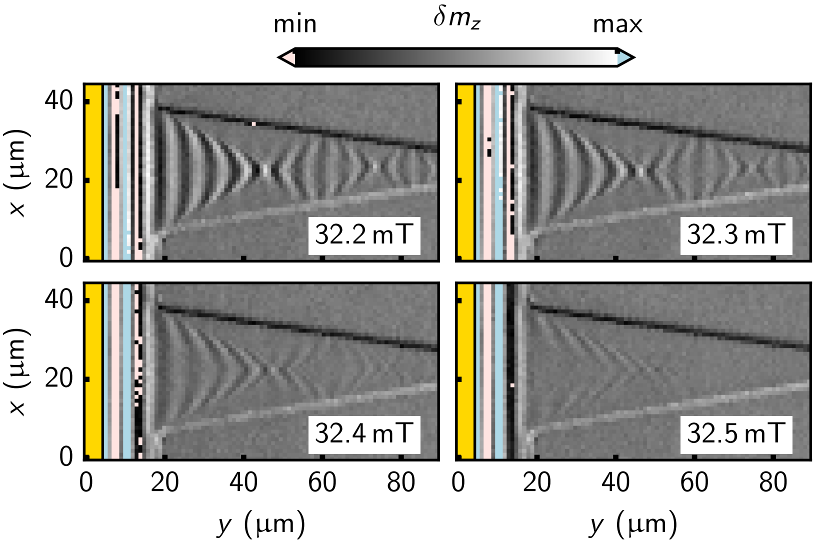

Figure 8.9. TR-MOKE measurement with $f = 2.8\,\mathrm{GHz}$ at different external magnetic fields slightly below the stop band. Caustic-like beams occur, which are attenuated upon propagation along the trapezoid.

and with an external magnetic field of $\mu_0 H = 23\,\mathrm{mT}$, transmission in the $|S_{21}|$ channel is observed, but minimal transmission in the $|S_{31}|$ trace is present. Similar behavior is observed in the data with an excitation frequency of $f = 2.7\,\mathrm{GHz}$ data at an external magnetic field of $\mu_0 H = 29\,\mathrm{mT}$.

Moreover, the transmission in the $|S_{31}|$ trace also appears to be suppressed for external magnetic fields slightly below the hybridization band (highlighted by grey-shaded rectangles). In this context, additional Kerr images approaching the hybridization from lower external magnetic fields at an excitation frequency of $f = 2.8\,\mathrm{GHz}$ are presented in Fig. 8.9. The images reveal the presence of caustic-like beams that gradually fade away during propagation along the patterned geometry, contributing to the early cessation of transmission in $|S_{31}|$.

8.5. Edge Modes due to Imperfect Fabrication

Fig. 8.10 exhibits several TR-MOKE maps with different excitation frequencies and relative phases between rf excitation and laser pulses under an external magnetic field of $\mu_0 H = 33.5\,\mathrm{mT}$. Propagation inside the trapezoid is observed, and in the lower-frequency (2.4 GHz, 2.48 GHz, 2.56 GHz) Kerr images, intense caustic-like beams are reflected back and forth within the trapezoidal waveguide. Close to those reflection points, a localized mode profile emerges at the edge of the patterned YIG, extending further in x-direction than the modes from the previous Kerr images. Upon adjusting the relative phase between rf excitation and laser pulses, the magnetic contrast of these localized modes changes. At conditions where the caustic-like beams fade, and DE-like modes become dominant in the propagation profile (2.72 GHz), the edge contrast vanishes.

Fig. 8.11(a) illustrates the height profile of a segment of the trapezoidal waveguide recorded by atomic force microscopy (AFM). Line profiles across the trapezoid edge in Fig. 8.11(b) indicate that the height transition from YIG to the GGG substrate is not sharp but rather

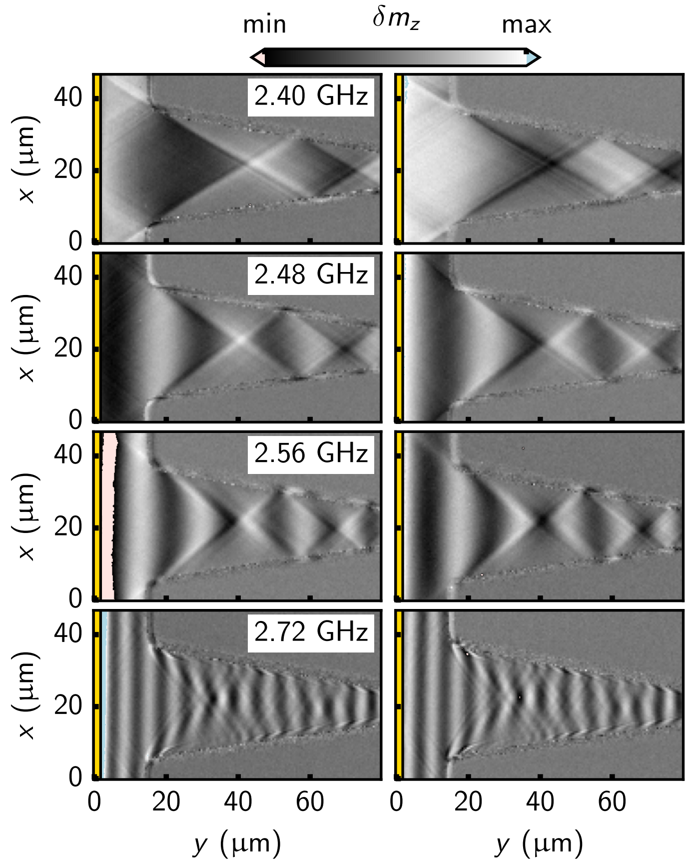

Figure 8.10. Kerr images with an external magnetic field of $\mu_0 H = 33.5\,\mathrm{mT}$. The left column shows Kerr images at one fixed relative phase between rf excitation and laser pulses (in-phase) for different frequencies. The right column shows the corresponding Kerr images shifted by 90°in phase relative to the left column (out-of-phase). In the caustic regime, modes in the edges of the trapezoid occur.

gradual, spanning a distance of about 1-2 µm along the x-direction. This can be attributed to imperfections in the fabrication processes resulting in nonuniform Argon etching.

Due to their well-defined directionality, the caustic-like beams are able to access the wedge-like boundary region. Each point of this edge region itself may then serve as a secondary point-like excitation source with a finite size of the order of the beam's width [44, 140]. Hence, spin wave modes may be excited within this transitional region. Fig. 8.11(c) displays iso-frequency curves for various film thicknesses at specific experimental parameters (2.48 GHz, 33.5 mT). These iso-frequency curves show that the potentially excited modes remain within the optical resolution limit of the TR-MOKE set-up across a considerable range of film thickness. As a result, mode profiles in the transitional region appear.

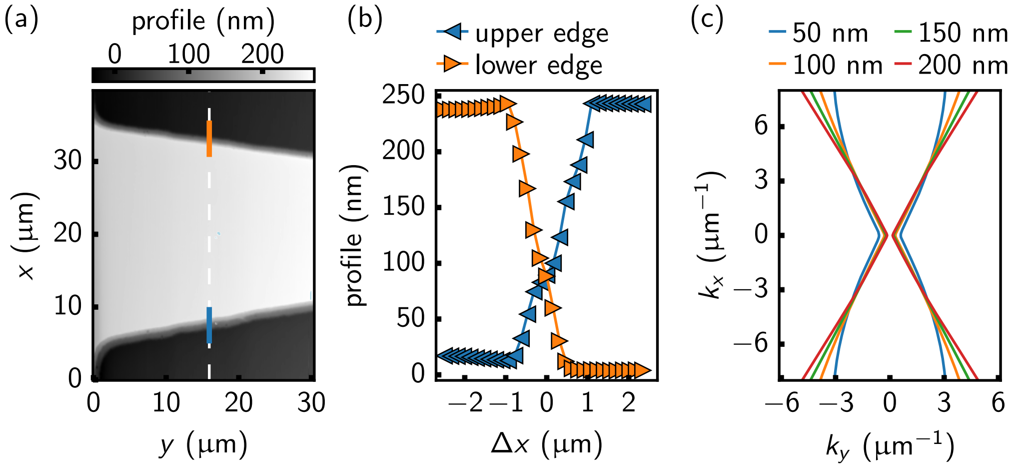

Figure 8.11. (a) Atomic force microscopy profile of the trapezoidal waveguide. (b) Line profiles taken across blue and orange dashed lines in (a). (c) Iso-frequency curves for various film thicknesses at an excitation frequency of $f = 2.48\,\mathrm{GHz}$ and a magnetic field of $\mu_0 H = 33.5\,\mathrm{mT}$.

Part IV.

Spin Wave Propagation in a Ring-Shaped Waveguide

Parts of this chapter are prepared for publication.

9. Motivation and Experimental Design

Magnonic structures that permit the propagation of only specific spin wave modes, known as spin wave filters, have been suggested through several approaches [21, 186–188]. Kim *et al.* [188], assessed a broadband GHz-range spin wave filter based on engineering width-modulated magnonic waveguides with micromagnetic simulations. Qin *et al.* experimentally demonstrated a narrow-band magnonic Fabry-Pérot interferometer [21]. Recently, ring-shaped magnonic resonators have emerged as a promising approach for spin wave filtering and engineering [50–52, 189], drawing parallels to photonic ring resonators [190], where interference effects occur along the ring.

Building on the principles of ring resonators, Iwaba *et al.* [189] explored a feedback-ring structure that enhances spin waves through phase matching. In the work of Odintsov *et al.* [50], micromagnetic simulations explored the coupling of two sub-millimeter-sized YIG stripes via a ring-shaped magnonic microcavity positioned between them. Note that the stripes and the cavity are spatially separated. The study suggested that this configuration allows for control of spin wave transmission between the two stripes. The transmission depends on the external magnetic field strength and angle due to the wavelength dependence of the coupling of spin waves and the excitation of different spin wave modes within the ring cavity. Recent experimental work validated these predictions, demonstrating filtering and demultiplexing capabilities [51].

A similar approach using micromagnetic simulations was explored by in magnonic ring resonators on the nanoscale by a [52], but on the nanoscale and with the ring in a zero-field vortex state. Filtering effects were observed based on interference between the initial wave and the wave from the ring resonator, accumulating a phase within the ring proportional to its radius. This closely resembles its optical counterpart. The nanometer dimensions, however, make this approach challenging to realize experimentally.

This chapter aims to experimentally investigate spin wave propagation in a ring-shaped magnonic waveguide. To this end, a ring attached to a stripe was patterned using optical lithography and Argon etching of a 200 nm thick YIG film. A sketch of the device is illustrated in Fig. 9.1. The magnonic stripe and ring have a width of 7 µm, with the ring having an inner radius of 3.5 µm. Spin waves in the dipolar regime were excited with a 2 µm wide microstrip antenna, and measurements were conducted in the DE- and BV-configuration. Incoming waves ($\mathrm{SW_{in}}$) scatter into the ring resonator, potentially interfering with the ring modes and resulting in an outgoing spin wave ($\mathrm{SW_{out}}$).

The fabricated structure has two limitations for direct phase accumulated interference along the ring. First, the structure lacks local separation between the ring and the stripe. The ring and waveguide are not directly decoupled. Second, due to the micrometer size of the patterned device and the wavelengths in the dipolar regime, the experimental approach more closely reflects the work of Odintsov *et al.* [50, 51] and Iwaba *et al.* [189], where several propagating

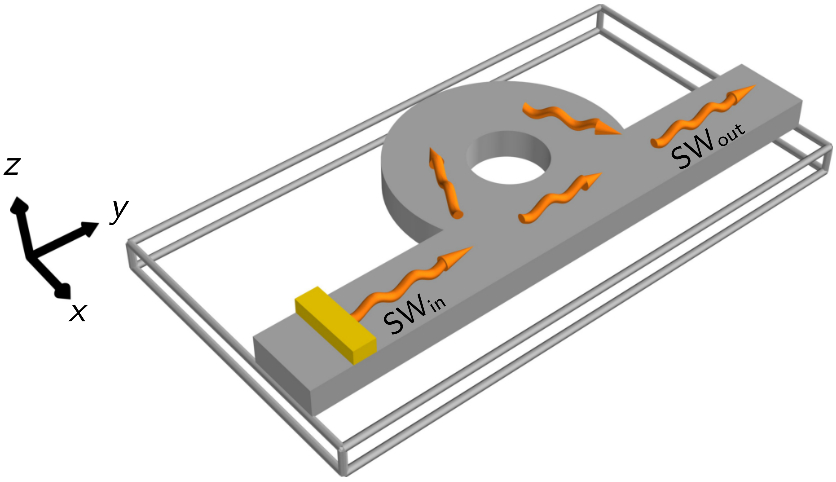

Figure 9.1. Experimental design of the spin wave filter. The waveguide and the ring are 7 µm wide, the inner radius of the ring is 3.5 µm, and the microstrip (golden cuboid) width is 2 µm. Both DE ($\boldsymbol{H} \parallel \boldsymbol{e}_x$) and BV geometry ($\boldsymbol{H} \perp \boldsymbol{e}_y$) were excited in the stripe section of the waveguide.

spin wave modes are present in the ring. Nevertheless, spin wave mode interaction between the ring and stripe is still expected in the experimental design.

An external magnetic field of $\mu_0 H = 70\,\mathrm{mT}$ was applied for all measurements. Fig. 9.2 shows the corresponding full film dispersion relation in the dipolar regime. The dispersion relation includes various possible spin wave modes ranging from the limiting cases of BV to DE modes. The $k = 0$ mode is expected to appear at $f_{\mathrm{FMR}} \approx 3.68\,\mathrm{GHz}$. Measurements spanned a frequency range within the spin wave spectrum, where either DE or BV modes excited in the stripe propagate towards the ring, potentially exciting the full spin wave spectrum at the given frequency and interfering with the initial wave.

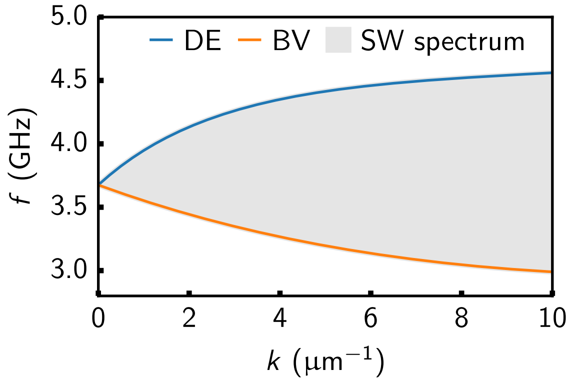

Figure 9.2. Dispersion relation for 200 nm thick YIG film under an external magnetic field of $\mu_0 H = 70\,\mathrm{mT}$. The spin wave (SW) spectrum includes spin wave modes between the DE and BV cases, with the FMR mode ($k = 0$) at $f_{\mathrm{FMR}} \approx 3.68\,\mathrm{GHz}$.

10. Experimental Results

Reasonable frequency resolution is necessary to investigate a frequency-dependent transmission of incoming and outgoing spin waves. Thus, the SNS-MOKE is better suited for this kind of measurement as it mostly overcomes the frequency restriction of the standard TR-MOKE (cf. Section 2.2.3). Additionally, the absolute precession amplitude, useful for determining transmission efficiencies, can be extracted in a single measurement. All the presented measurement data were obtained using the SNS technique. Note that the excitation frequency was always detuned by the same few kHz from the presented values for the actual measurement. However, values are rounded to the second digit after the comma in this section for better readability.

10.1. Backward-Volume Geometry

Figs. 10.1(a)-(d) show Kerr maps recorded at different frequencies with the external magnetic field applied along the YIG stripe. For each excitation frequency, two maps are presented. The left column displays $R = \sqrt{X^2 + Y^2}$ [136] from the lock-in detector, representing the absolute precession amplitude. X and Y denote the two channels of the lock-in. For better contrast, the R maps are normalized to their respective maximum value within the device boundaries. The right column of Figs. 10.1(a)-(d) shows $\sin(\theta_{\mathrm{LI}})$ of the lock-in phase $\theta_{\mathrm{LI}} = \arctan(Y/X)$ [136] illustrating the wavefronts of the spin wave. To enhance visibility, the phase data is displayed only within the spatial boundaries of the device, as determined from the topographic image. This restriction is applied because outside these regions, where spin waves are absent, the phase exhibits random fluctuations, which distract from the relevant features.

First, the propagation profiles of the detected amplitude and phase maps are discussed. In Fig. 10.1(a), the spin wave amplitude decreases along the YIG stripe region, barely reaching the ring section, with no observable spin wave amplitude beyond the ring. The phase map shows a small wavelength for the spin wave mode in the stripe. Inside the ring, several wavefronts are visible in the phase map, while a faint wavefront signal is observed beyond the ring. At an excitation frequency of $f = 3.76\,\mathrm{GHz}$ (Fig. 10.1(b)), plane wavefronts with higher wavelength propagate within the YIG stripe towards the ring section. At the ring section, scattering events occur, and spin wave amplitude is observed along almost the entire ring, with caustic-like features reflected back and forth. The phase map displays complex wavefront patterns within the ring. Beyond the ring section, almost no amplitude signal is visible, although the phase image may hint at a small amplitude plane wave.

At an excitation frequency of $f = 3.92\,\mathrm{GHz}$ (Fig. 10.1(c)), a spin wave amplitude is visible along the section up to the ring. The phase image indicates the presence of a spin wave mode

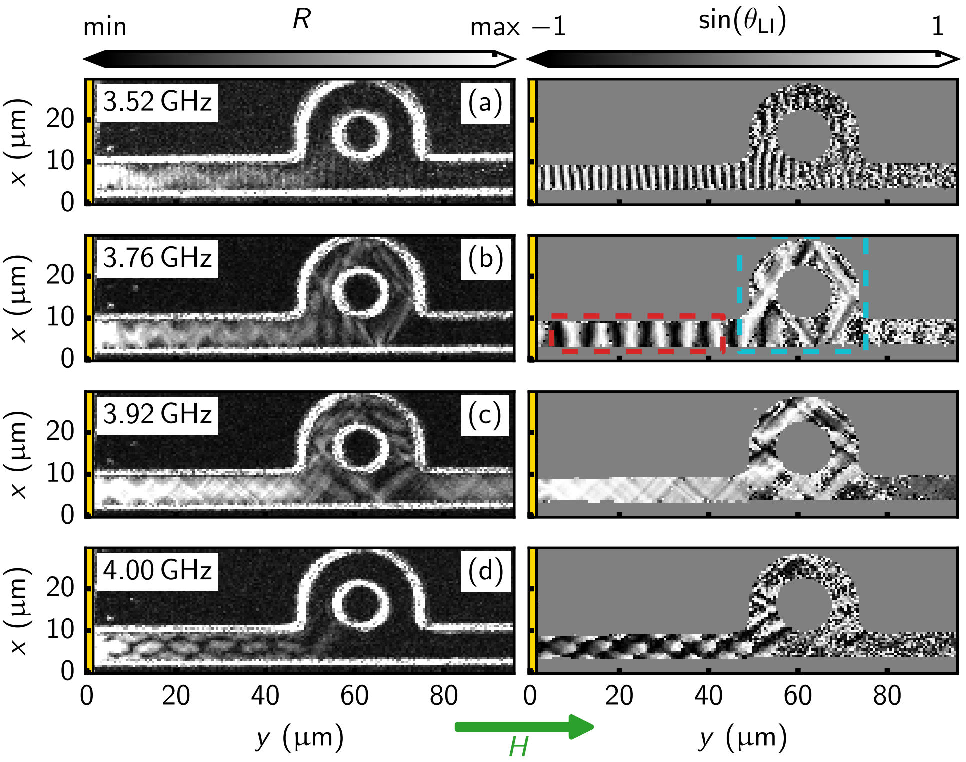

Figure 10.1. (a)-(d) Maps recorded by SNS-MOKE at different frequencies with an external magnetic field of $\mu_0 H = 70\,\mathrm{mT}$. Images in the left column represent the absolute amplitude R of the lock-in, while the right column represents the wavefronts of the spin waves in terms of $\sin(\theta_{\mathrm{LI}})$. A clear amplitude signal beyond the ring is observed in (c). Golden areas mark the excitation antenna, and the green arrow indicates the direction of the external magnetic field. FT data is extracted from areas within the cyan- and red-colored contours.

with a relatively large wavelength. An amplitude signal and a complex phase pattern are observed inside the ring part of the waveguide. Caustic-like features are present again, this time with a different beam direction and reflection angle, and are also visible in the stripe regions. Diminished amplitude areas are observed in the intermediate section of the ring and stripe. In contrast to the previous maps, a clear amplitude signal is visible beyond the ring, indicating that the transmission along the device may depend on the excitation frequency. In Fig. 10.1(d), a nodal structure across the width of the YIG stripe is observed, implying excitation of higher-order width modes. No clear transmission beyond the ring is noted.

In the following, a detailed analysis of spin wave propagation in the BV-geometry based on Figs. 10.1(a)-(d) is presented. The analysis starts with an FT examination of the wavefronts and the effective magnetic field distribution, followed by an exploration of the ring's influence on propagation. Finally, the transmission properties across the ring, focusing on the frequency-dependent suppression and transmission observed in the spatial maps, are discussed.

10.1.1. External Magnetic Field Offset and Effective Magnetic Field Distribution

Interestingly, above an excitation frequency of $f = 3.68\,\mathrm{GHz}$, no BV modes are predicted (cf. Fig. 9.2), yet clear wavefronts along the stripe are observed in the $f = 3.76\,\mathrm{GHz}$ maps (cf. Fig. 10.1(b)). Additionally, the transverse wavefronts in the stripe in Fig. 10.1(d) are unusual since the antenna should typically excite plane waves with directionality.

To better understand the propagation characteristics, FT data of the wavefront maps for the incoming wave and the ring section are separately extracted for each frequency from the red- and cyan-colored contours displayed in Fig. 10.1(b). Figs. 10.2(a)-(d) show the respective results. Note that no windowing function was applied here. The red color represents the FT data from the stripe, while the grey-scale represents the FT data from the ring section. The FT data is compared to the analytical solution of the respective iso-frequency curves for the nominal external magnetic field of $\mu_0 H = 70\,\mathrm{mT}$ (dashed blue curve) and for an external magnetic field of $\mu_0 H = 74\,\mathrm{mT}$ (dashed orange curve), following Kalinikos and Slavin (KS) [70].

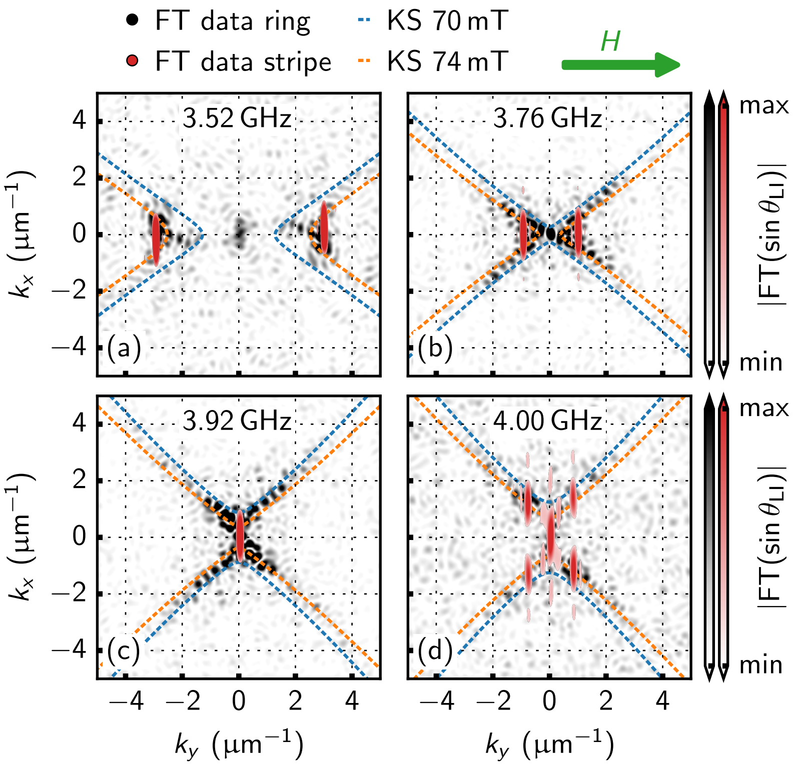

Figure 10.2. (a)-(d) FT data extracted from stripe and ring sections highlighted in Fig. 10.1. Many spin wave modes across the corresponding iso-frequency curve are excited. Mostly one single spin wave mode is excited in the stripe, while many spin wave modes following the iso-frequency curve from Kalinikos and Slavin (KS) (dashed orange and blue curves) are present within the ring.

Deviations between FT data and predicted iso-frequency curve for an external magnetic field of $\mu_0 H = 70\,\mathrm{mT}$ occur, particularly in Figs. 10.2(a) and (b) where plane waves are observed within the stripe in the real space maps. However, a reasonable match is found for an external magnetic field value of $\mu_0 H = 74\,\mathrm{mT}$, which is well within the margin of error of the experimental setup.

The higher external magnetic field shifts the FMR mode to $f_{\mathrm{FMR}} \approx 3.81\,\mathrm{GHz}$, consequently increasing the upper limit for the BV branch in the dipolar range. This can also be observed in Fig. 10.2(b), where, in contrast to $\mu_0 H = 70\,\mathrm{mT}$, BV character is predicted for $\mu_0 H = 74\,\mathrm{mT}$ within the stripe. Therefore, it is concluded that a small external magnetic field offset of about $4\,\mathrm{mT}$ is present, and the stripe spin wave modes in Figs. 10.2(a) and (b) are of BV type. In Fig. 10.2(c), the stripe spin wave mode appears to be close to the FMR mode, and the stripe spin wave mode in Fig. 10.2(d) appears near DE-type modes, which cannot be directly excited by the antenna. However, similar to Section 6.2, the edges transverse to the antenna can also drive spin waves, leading to the standing wave pattern across the width of the stripe.

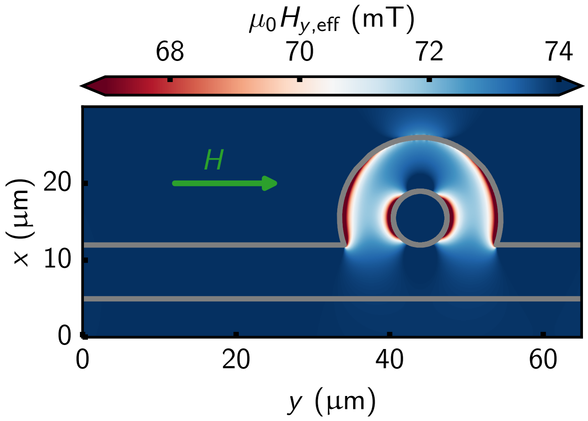

Figure 10.3. Micromagnetic simulations of the y-component of the effective magnetic field, $\mu_0 H_{y,\mathrm{eff}}$, for a longitudinally magnetized geometry under an external field of $\mu_0 H = 74\,\mathrm{mT}$. The green arrow indicates the direction of the applied external magnetic field.

Within the ring section, there is also a reasonable agreement between the $\mu_0 H = 74\,\mathrm{mT}$ isofrequency curve and the FT data. However, it shall be noted that the situation within the ring is more nuanced. Fig. 10.3 shows micromagnetic simulations [66] of the y-component of the effective magnetic field, $\mu_0 H_{y,\mathrm{eff}}$ for the longitudinally magnetized geometry with an applied external magnetic field of $\mu_0 H = 74\,\mathrm{mT}$.[1] In the stripe section, the effective magnetic field distribution is homogeneous and matches the applied magnetic field. In contrast, within the ring section, demagnetizing effects occur, which lead to local reductions and inhomogeneities of the effective magnetic field. As a result, the dispersion relation within the ring varies locally, adding complexity to the behavior of spin waves in this region.

10.1.2. Effect of the Ring Structure on Spin Wave Propagation

After addressing some basics of spin wave propagation within the device, a more detailed examination of the differences between the propagation within the stripe and the ring section is provided.

From the FT data (Figs. 10.2(a)-(d)), it can be observed that within the stripe section, mostly one spin wave mode is present. In contrast, multiple spin wave modes, governed by

---

[1] The simulation used a grid of $600 \times 1920 \times 4$ and a cell dimension of $50\,\mathrm{nm}$ in all 3 dimensions.

the anisotropic in-plane iso-frequency curve, appear within the ring section. This behavior is particularly prominent in Figs. 10.2(b) and (c), where a strong amplitude signal R is detected inside the ring.

Additionally, the allowed wavenumbers within the ring seem to be discrete. This is illustrated in Fig. 10.4, which displays zoomed portions of Figs. 10.2(b) and (c). To verify that this discretization arises from the magnetic contrast and not merely from the ring geometry, an additional Fourier transform was performed on a binary image of the ring section. Here, areas with wavefront contrast were assigned a value of 1, and areas without contrast were set to 0, essentially representing the topography. Fig.10.5(a) shows the binary image, and Fig.10.5(b) shows the corresponding FT data, where a pronounced FT amplitude is predominantly localized around $k = 0\,\mu\text{m}^{-1}$. This strongly suggests that the discrete patterns in Fig. 10.4 indeed correspond to spin wave modes.

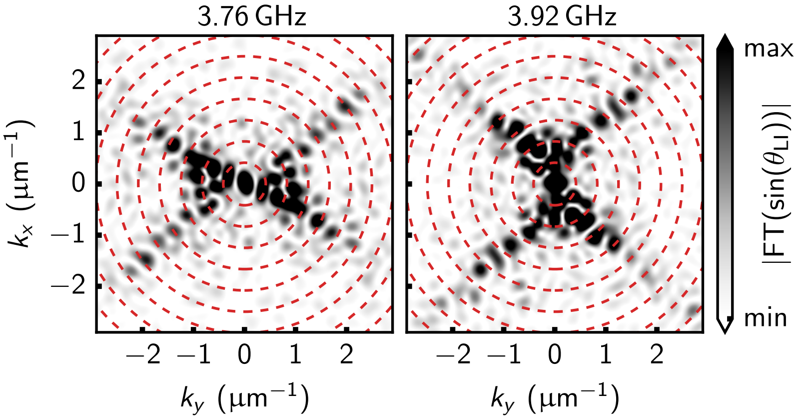

Figure 10.4. FT data extracted from ring section compared to ring eigenmodes. Red dashed circles illustrate the ring eigenmodes across the ring's width. The spin wave modes are discretized due to the ring's finite width.

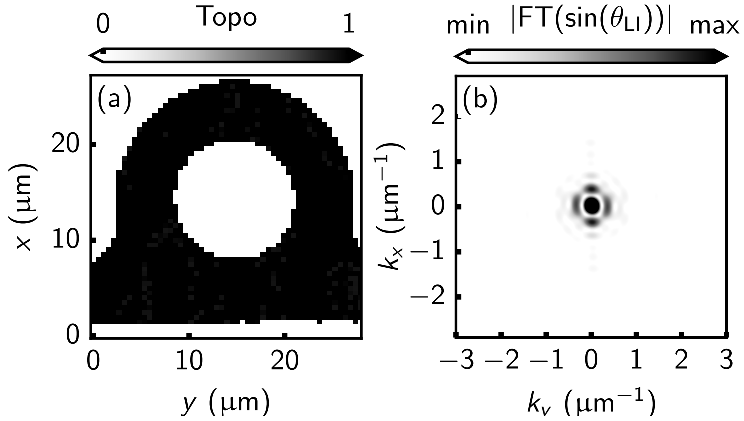

Figure 10.5. (a) Binary representation of the ring section topography. (b) Corresponding FT data of the binary image.

Furthermore, the red dashed circles in Fig. 10.4 indicate the eigenmodes $k_{\text{ring},m} = \frac{m\pi}{w_{\text{ring}}}$ across the width w_{ring} of the ring with $m = 0, 1, 2, \ldots$. Note that due to inaccuracies in fabrication, the actual ring width may vary from the nominal value. Therefore, the ring width was estimated from the topographic map of the stripe section (cf. Appendix D), resulting in an estimated width $w_{\text{ring}} = (7.55 \pm 0.50)\,\mu\text{m}$. The mean value was then used to calculate $k_{\text{ring},m}$.

The spacing of the discrete FT data closely aligns with the spacing of the ring's width modes, as indicated by the dashed red circles. These circles largely intersect with the discrete FT data points, suggesting that the finite dimensions of the ring impose additional confinement on the propagating spin waves. Consequently, the spin waves permitted within the ring are determined by the convolution of the dispersion relation with the ring's width eigenmodes.

10.1.3. Transmission Properties

In the spatial SNS-MOKE maps in Figs. 10.1(a)-(d), a frequency-dependent transmission beyond the ring section was observed. To assess whether the suppression of propagation beyond the ring is solely due to the intrinsic attenuation length of the spin waves, line profiles of the precession amplitude R were extracted and averaged over three lines from the middle of the stripe section. The profile portions before the ring were fitted with an exponential decay of the form

$$f(y) = A_{\text{exp}} \cdot \mathrm{e}^{-y/L_{\text{att}}} \tag{10.1}$$

and compared to the extracted profile beyond the ring. A_{exp} denotes the amplitude of the exponential decay and L_{att} the attenuation length of the spin waves.

Fig. 10.6(a) serves as a visual guide, where the dashed red line indicates the profile extracted from the stripe region before the ring, and the dashed blue line marks the profile extracted across the remaining length of the structure. The dashed red and blue lines in Figs. 10.6(b)-(e) show the corresponding profiles of the amplitude R from Figs. 10.1(a)-(d). The solid red curves represent the exponential fit of the dashed red profile. Background offset, averaged over the orange dashed rectangle in Fig. 10.6(a), was subtracted from all profiles.

In Figs 10.6(b) and (e), the absence of amplitude signal beyond the ring aligns with the expected exponential decay of the initially excited spin wave. However, at an excitation frequency of $f = 3.76\,\text{GHz}$ (Fig. 10.6(c)), the behavior deviates. Within the junction region, where the stripe and ring merge, the amplitude largely follows the exponential decay, although varying amplitudes are observed, suggesting interference patterns. Beyond the ring, the amplitude signal drops off abruptly, noticeably deviating from the exponential decay. This suggests that the lack of transmission at this frequency cannot be attributed solely to intrinsic damping along the propagation distance in the stripe. At an excitation frequency of $f = 3.92\,\text{GHz}$ (Fig. 10.6(d)), on the other hand, the clear transmission signal beyond the ring is consistent with the exponential decay within the stripe, whereas the signal within the junction region is diminished.

These findings imply that the transmission properties are influenced not only by the intrinsic attenuation but also by the interaction and scattering of various excited spin wave modes within the ring section and near the junction between the stripe and the ring. Rather than resulting from a purely accumulated phase from a wave of constant wavelength across the ring, the process of frequency filtering, however, is more intricate. As indicated by the FT data (cf. Figs. 10.2(a)-(d)), multiple spin wave modes are present within the ring section,

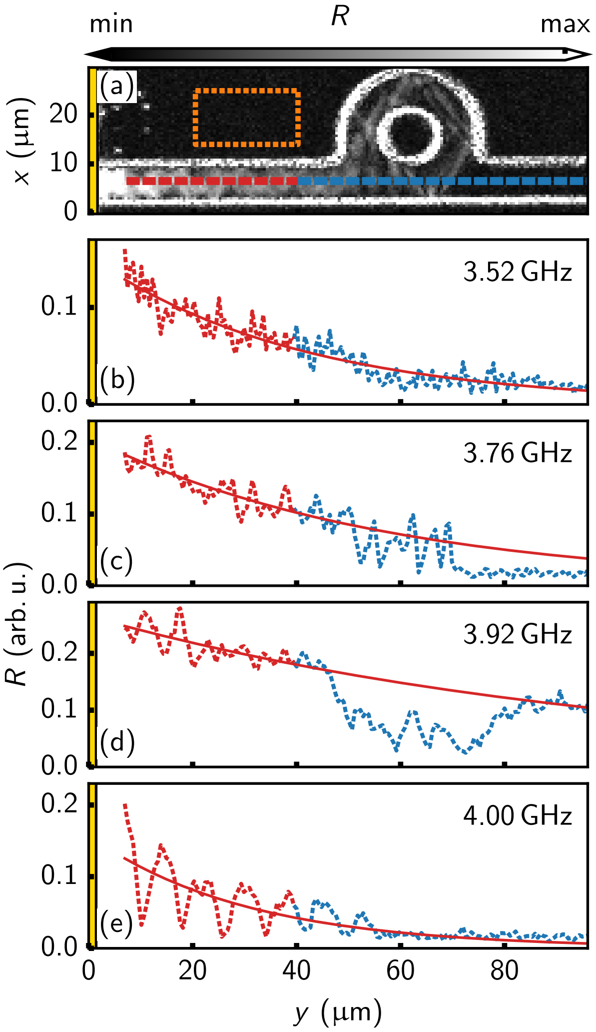

Figure 10.6. Line profiles of amplitude R along the center of the stripe. (a) Exemplary spatial map of the amplitude R acquired by SNS-MOKE at an excitation frequency $f = 3.76\,\mathrm{GHz}$ (cf. Fig. 10.1(b)). Dashed red and dashed blue lines indicate the positions where line profiles were extracted. The dashed orange rectangle marks the region where the background offset was averaged and subtracted from all profiles. (b)-(e) Corresponding line profiles of R for different excitation frequencies. The dashed red and the dashed blue lines represent the profiles along the dashed red and blue lines in (a). The solid red curve corresponds to an exponential fit of the dashed red profile before the ring section.

allowing waves of different wavelengths to interfere constructively or destructively within the ring section. These complex interactions can facilitate or suppress propagation after the ring section depending on the frequency, as the allowed spin wave modes themselves are governed by the frequency- and field-dependent dispersion relation. In addition, the geometry of the ring provides further mode selection due to its confinement and discretization of the propagation spectrum (cf. Fig. 10.4), and its inhomogeneous effective magnetic field distribution (cf. Fig. 10.3).

Further SNS-MOKE measurements at different excitation frequencies were performed to better understand the transmission properties of the ring. In this context, the regions A, J, and B were defined and are illustrated in the topography image in Fig. 10.7(a). Averaging the amplitude R over the rectangular regions then provides a measure for the experimental spin wave amplitude before, at, and after the ring junction. The results for different frequencies are presented in Figs. 10.7(b)-(d). The small red dots represent the extrapolated values at the center of regions A, J, and B obtained from the exponential fit in the stripe section before the ring (cf. Figs. 10.6(b)-(e)).

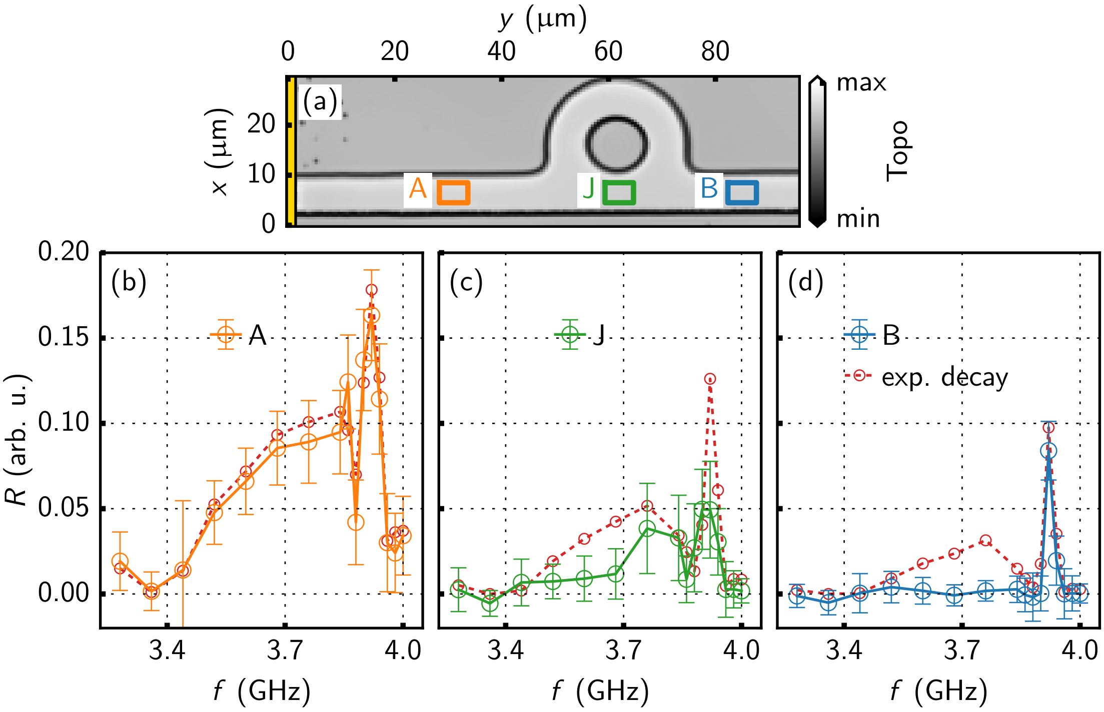

Figure 10.7. Spin wave amplitude signal across the device as a function of frequency. (a) Topographic image introducing square areas A, J, and B before, at, and after the junction. (b)-(d) Amplitudes averaged across squares A, J, and B as a function of frequency. Error bars indicate the standard deviation of the averaged mean. Small red dots and dashed red lines indicate values at the center position of A, J, and B if an exponential decay is assumed in the stripe region before the ring (cf. red lines in Fig. 10.6).

The spin wave amplitude varies with excitation frequency across different regions of the device. In region A (Fig. 10.7(b)), the amplitude is low for excitation frequencies below $f \approx 3.5\,\mathrm{GHz}$. As the frequency increases, the amplitude gradually rises. At $f = 3.88\,\mathrm{GHz}$, a sharp dip occurs, followed by a strong increase in amplitude to its maximum at $f = 3.92\,\mathrm{GHz}$. Beyond this frequency, the amplitude rapidly decreases. The experimental amplitude closely matches the extrapolated values from the exponential fit.

In region J (Fig. 10.7(c)), the amplitude tends to increase with increasing frequency, exhibiting a sharp dip near $f = 3.88\,\mathrm{GHz}$ and reaching its maximum at $f = 3.92\,\mathrm{GHz}$. The relatively large error bars in this region suggest complicated interference patterns at the junction. The extrapolated exponential fit shows generally good agreement with the experimental data, though it tends to slightly overestimate the experimental values, particularly at $f = 3.92\,\mathrm{GHz}$.

Region B (Fig. 10.7(d)) exhibits a different behavior compared to regions A and J. After the ring, there is little to no amplitude detected for frequencies below $f = 3.92\,\mathrm{GHz}$. At $f = 3.92\,\mathrm{GHz}$, a sharp transmission peak is observed, rapidly falling off afterward, exhibiting some amplitude at $f = 3.94\,\mathrm{GHz}$, but no amplitude beyond. Additionally, the extrapolated amplitudes from the exponential fit predict a sizable amplitude between $f = 3.6\,\mathrm{GHz}$ and $f = 3.84\,\mathrm{GHz}$. However, this prediction contrasts with the experimental data, which show no amplitude in this frequency range.

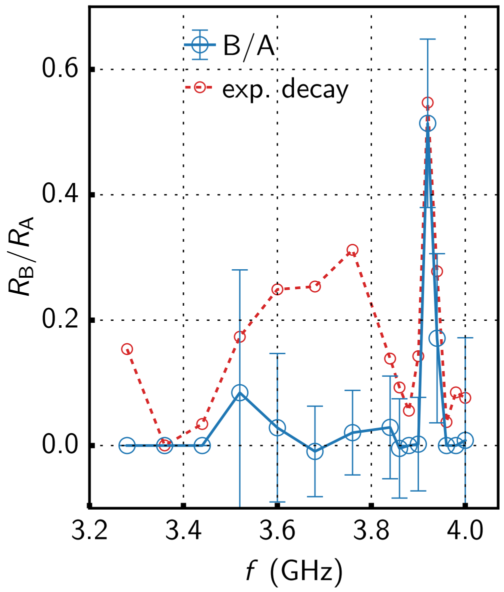

Figure 10.8. Transmission parameter $R_\mathrm{B}/R_\mathrm{A}$ from region A to region B as a function of frequency. In the band from $f = 3.6\,\mathrm{GHz}$ to $f = 3.84\,\mathrm{GHz}$ transmission is suppressed. Strong frequency selective transmission is observed for $f = 3.92\,\mathrm{GHz}$. Experimental values with error bars exceeding 0.35 were set to zero, and no error bar is shown for better visualization.

The frequency-dependent transmission across the ring guide is further illustrated in Fig. 10.8, where a transmission parameter is defined as the ratio $R_\mathrm{B}/R_\mathrm{A}$. Note that when $R_\mathrm{B}/R_\mathrm{A}$ is very small, essentially indicating no transmission, the associated error bars tend to become disproportionately large. Therefore, for better visualization, data points with error bars exceeding 0.35 were set to zero, and no error bars are displayed for those points in Fig. 10.8. In the frequency band from $f = 3.6\,\mathrm{GHz}$ to $f = 3.84\,\mathrm{GHz}$, transmission is suppressed despite the exponential decay predicting transmission. A sharp transmission peak is observed at $f = 3.92\,\mathrm{GHz}$.

In conclusion, these observations indicate that the transmission efficiency of spin waves through the ring depends on the excitation frequency. A sharp transmission peak occurs around $f = 3.92\,\mathrm{GHz}$, while other frequency bands show significant attenuation beyond the ring, demonstrating the system's frequency selectivity. This transmission suppression likely results from interference and scattering involving multiple spin wave modes, similar to the simulations of Odintsov *et al.* [50], rather than a purely accumulated phase along the ring.

10.2. Damon-Eshbach Geometry

Analogous measurements were conducted in the DE-geometry, i.e., with the YIG stripe transversely magnetized. Compared to the BV case, the spin wave modes within the ring may interact differently with the DE-like initial mode in the stripe, potentially resulting in different frequency selectivity of the transmission. Exemplary maps acquired using SNS-MOKE are depicted in Figs. 10.9(a)-(d).

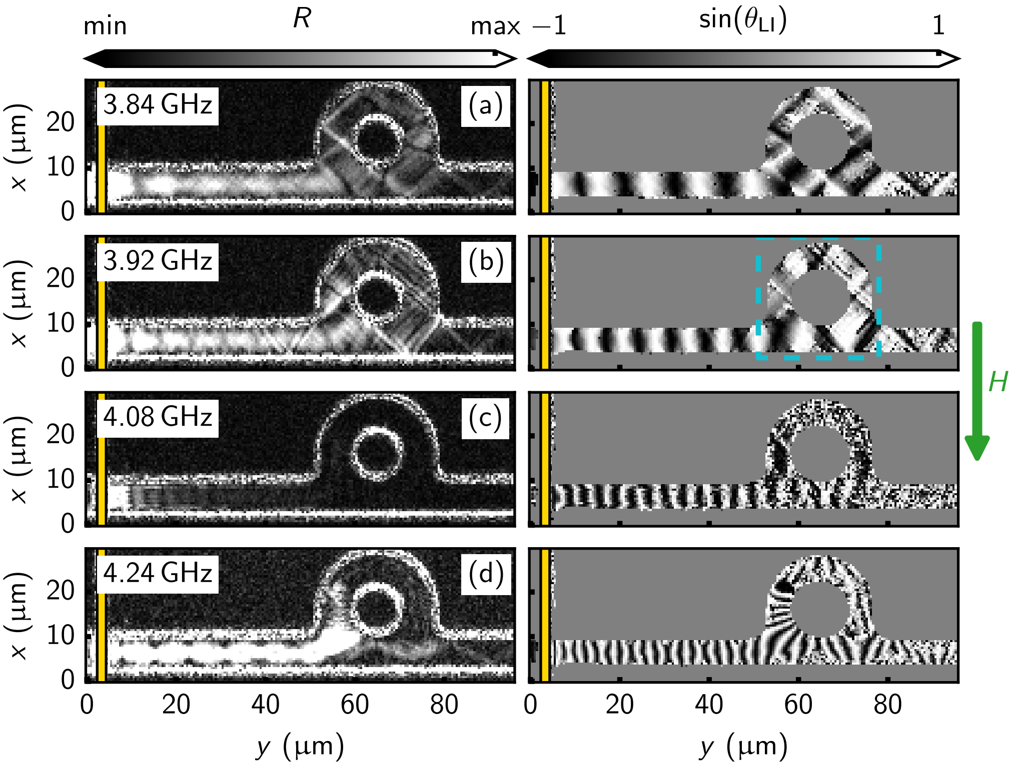

Figure 10.9. Maps in the DE-geometry at different frequencies. (a)-(d) propagation within the stripe is observed where the wavelength decreases with increasing external magnetic field. Caustic-like features are visible in the stripe section after the ring in (a) and (b).

In each map, a detectable amplitude signal is present within the stripe section. The phase maps show that plane spin waves are launched into the stripe from the microstrip antenna at each excitation frequency. Following the DE dispersion relation, the wavelength decreases with increasing frequency. In Figs. 10.9(a) and (b), a notable amplitude is observed within the initial stripe section and the ring section. Beyond the ring section, a sharp decrease in amplitude is detected in the stripe region, though caustic-like beam features, reflecting back and forth, are still visible. In the phase maps, as the plane waves advance closer to the ring section, their wavelength appears to increase. Within the ring section, complex wavefront patterns emerge, similar to those observed in the BV case. In Fig. 10.9(c), the amplitude signal abruptly ceases early along the stripe, while in Fig.10.9(d), the signal abruptly decreases after reaching the ring section. Beam-like features beyond the ring section are also observed in Fig. 10.9(d).

10.2.1. Effective Magnetic Field Distribution and PSSW Hybridization

Fig 10.10 shows micromagnetic simulations of the effective magnetic field [66] for the transversely magnetized geometry[2] under an external magnetic field of $\mu_0 H = 74\,\mathrm{mT}$. In contrast to the longitudinally magnetized case (Fig. 10.3), the stripe section exhibits a pronounced reduction of the effective magnetic field. As the stripe transitions into the ring section, the effective magnetic field gradually increases, as indicated by the iso-field line for $\mu_0 H_{x,\mathrm{eff}} = 70.6\,\mathrm{mT}$. This increase leads to a shift in the dispersion relation, resulting in the observed change in propagation wavelength along the stripe, with the spin waves adopting larger wavelengths. Within the ring, the effective magnetic field, and consequently the dispersion relation, also varies significantly.

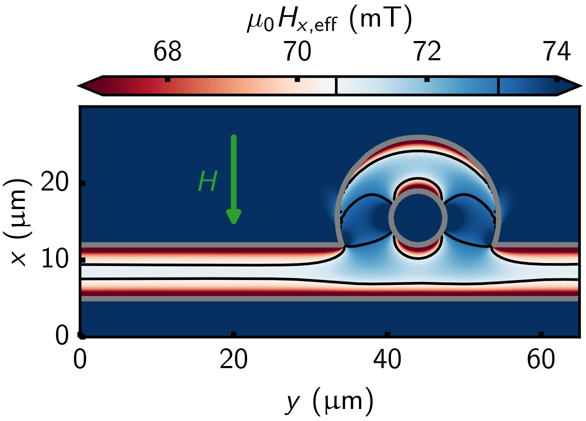

Figure 10.10. Micromagnetic simulations of the x-component of the effective magnetic field, $\mu_0 H_{x,\mathrm{eff}}$, for a transversely magnetized waveguide under an external magnetic field of $\mu_0 H = 74\,\mathrm{mT}$. The black contour lines correspond to effective magnetic fields of $\mu_0 H_{x,\mathrm{eff}} = 70.6\,\mathrm{mT}$ and $\mu_0 H_{x,\mathrm{eff}} = 73.1\,\mathrm{mT}$. The green arrow indicates the direction of the applied external magnetic field

Additionally, the DE modes can exhibit mode hybridization with the first PSSW, unlike the BV modes. Fig 10.11 shows the simulated full film stop band conditions for DE modes within the relevant experimental range. The stop band spans a broad excitation frequency range of $f \approx 4.0\,\mathrm{GHz}$ to $f \approx 4.25\,\mathrm{GHz}$ for external magnetic fields between $\mu_0 H = 68\,\mathrm{mT}$ and $\mu_0 H = 74\,\mathrm{mT}$. In the BV measurements, these frequencies are mostly not even reached.

Local hybridization-induced attenuation effects like those discussed in Section 8.3 can occur. In Fig. 10.9(c), the amplitude signal ceases soon after the antenna. At an excitation frequency of $f = 4.08\,\mathrm{GHz}$ (lower dotted line in Fig 10.11), the stop band spans from approximately $\mu_0 H = 68\,\mathrm{mT}$ to $\mu_0 H = 70.6\,\mathrm{mT}$, which is consistent with the simulated effective magnetic field in the stripe, which is expected to be approximately $\mu_0 H_{x,\mathrm{eff}} = 71\,\mathrm{mT}$ or lower. Consequently, the strong hybridization-induced damping prevents the spin wave from reaching the ring.

In Fig. 10.9(d), the DE mode propagates along the stripe and comes to a halt at the left side of the ring. The lower magnetic field limit of the stop band at an excitation frequency

---

[2] The simulation used a grid of $600 \times 1920 \times 4$ and a cell dimension of $50\,\mathrm{nm}$ in all 3 dimensions.

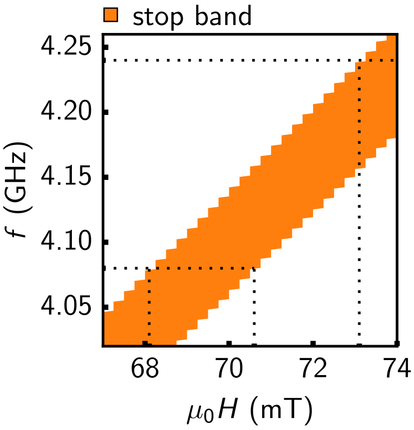

Figure 10.11. Hybridization-induced stop band for DE modes. The dotted lines illustrate the respective field limits of the stop band at $f = 4.08\,\mathrm{GHz}$ (cf. Fig. 10.9(c)) and $f = 4.24\,\mathrm{GHz}$ (cf. Fig. 10.9(d)).

of $f = 4.24\,\mathrm{GHz}$ (upper dotted line in Fig 10.11) is simulated to be approximately $\mu_0 H = 73.1\,\mathrm{mT}$. The corresponding iso-field line of the effective magnetic field in Fig 10.10 (black line) aligns very well with the spin wave's stop position. Note, however, since other spin wave modes have already been scattered within the transition area and since the stop field is not fully reached in the stripe section, some spin waves are not completely damped and may reach the junction section and the region beyond the ring (cf. Fig. 10.9(d)).

Thus, in the DE geometry, transmission across the ring is already hampered by hybridization-induced damping effects rather than mode interaction and scattering within the ring. As shown in Fig 10.11, this happens over a broad range of frequencies, making the DE geometry less suitable for broadband transmission in the first place, particularly for 200 nm thick YIG films.

10.2.2. Transmission Properties

As previously noted, in Figs. 10.9(a) and (b), a strong amplitude signal is detected in the initial stripe section and within the ring. However, beyond the ring, the spin wave signal drops off abruptly, with beam-like features dominating the profile. This suggests that transmission in this regime is primarily governed by the frequency-dependent directionality of caustic-like beams. Transmission may occur if these beams couple into the resonator at the proper angle, enabling them to escape into the stripe region after multiple reflections. However, because these caustic-like beams are spatially more confined, their transmission effects are relatively weak compared to those in the BV geometry (see Fig. 10.1(c)).

Further SNS-MOKE data were acquired at different excitation frequencies to evaluate the transmission properties, analogous to Section 10.1.3. Figs.10.12(a)-(c) present the resulting amplitude signals averaged across sections A, J, and B in the DE geometry (cf. Fig. 10.7).

The amplitudes vary with the excitation frequency. In region A, there is a small peak at $f = 3.44\,\mathrm{GHz}$. The maximum is reached at $f = 3.68\,\mathrm{GHz}$. This excitation frequency lies close to the expected FMR frequency when considering the reduction in the effective magnetic field within the center of the stripe section. The spin wave modes at higher frequencies than the

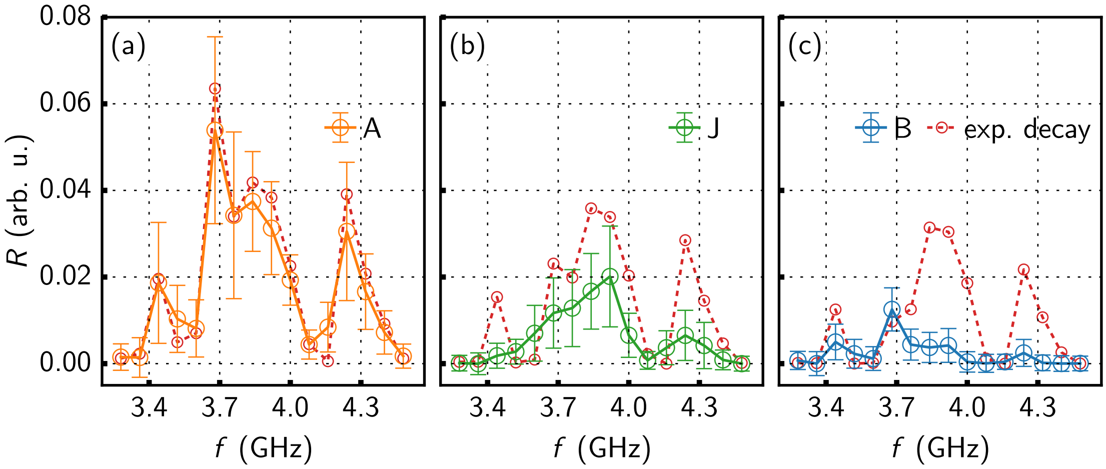

Figure 10.12. Spin wave amplitude averaged across regions (a) A, (b) J, and (c) B as a function of excitation frequency in the DE geometry. The dip in amplitude at 4.08 GHz is attributed to hybridization-induced attenuation.

FMR frequency correspond to DE modes in the stripe region. As the excitation frequency increases, the amplitude in region A decreases, with a pronounced dip at $f = 4.08\,\mathrm{GHz}$. The amplitude then rises, with a local peak at $f = 4.24\,\mathrm{GHz}$, followed by a decrease. The interpolated amplitudes from an exponential fit in the stripe region (cf. Fig. 10.6) show good agreement overall. However, it should be noted that this approach is less straightforward in DE geometry. The pronounced variations in the internal effective magnetic field, particularly as one approaches the ring, lead to local fluctuations in group velocity and, consequently, attenuation length (cf. Eq. (1.23)).

The amplitude dip at $f \approx 4.08\,\mathrm{GHz}$ in Fig. 10.12(a) can be directly attributed to the stop band where the increased damping prevents the DE mode from efficiently reaching region A (cf. Fig. 10.9(c)). Similar arguments can be made for the excitation frequency range from $f = 4\,\mathrm{GHz}$ to $f = 4.24\,\mathrm{GHz}$ for regions J and B, where hybridization with the first PSSW significantly influences the spin wave propagation, as discussed earlier.

In region J, the amplitude increases and reaches a maximum at $f = 3.92\,\mathrm{GHz}$. There is a dip at $f = 4.08\,\mathrm{GHz}$, followed by a small local peak at $f = 4.24\,\mathrm{GHz}$. Notably, the expected amplitude based on an exponential decay model deviates significantly at $f = 4.24$,GHz.

In region B, a small peak is observed at $f = 3.44\,\mathrm{GHz}$, with a maximum at $f = 3.68\,\mathrm{GHz}$, both aligning with the exponential decay model. Beyond this, the amplitude signal is almost non-existent, with a stark discrepancy between the measured amplitude and the expected exponential decay. DE modes typically have longer attenuation lengths than BV modes due to their higher group velocities (cf. Eq. (1.23)). Therefore, the strong decay observed is contrary to expectation. Between $f = 4\,\mathrm{GHz}$ and $f = 4.24\,\mathrm{GHz}$, hybridization-induced damping is evident, but the range from $f = 3.72\,\mathrm{GHz}$ to $f = 4\,\mathrm{GHz}$ cannot be explained by hybridization or exponential decay.

Fig. 10.13 shows FT data calculated from the cyan-colored contour in Figs. 10.9(a) and (b) at excitation frequencies of $f = 3.84$,GHz and $f = 3.92$,GHz, respectively. Similar to the BV geometry, multiple spin wave modes appear in the ring, governed by the anisotropic dispersion relation and the inhomogeneous internal magnetic field distribution. The spin wave modes exhibit a discretized behavior and show reasonable agreement with the ring's eigenmodes. This suggests that transmission suppression in this frequency range is caused by scattering and interference at the ring section, similar to the BV case.

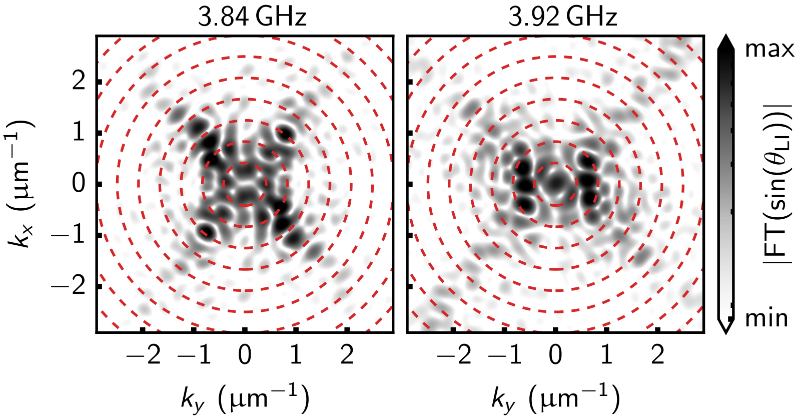

Figure 10.13. FT data extracted from ring section compared to ring eigenmodes. The FT data was calculated within the dashed cyan-colored contour in Figs. 10.9(a) and (b). Red dashed circles illustrate the ring eigenmodes across the width. For better contrast, the FT data is displayed on a logarithmic scale.

Fig. 10.14 presents the transmission parameter $R_\mathrm{B}/R_\mathrm{A}$, which reflects the behavior discussed above. Transmission is suppressed in the frequency range from $f = 3.72\,\mathrm{GHz}$ to $f = 4\,\mathrm{GHz}$ due to mode scattering and interference, while the band from $f = 4\,\mathrm{GHz}$ to $f = 4.24\,\mathrm{GHz}$ is affected by hybridization.

To conclude, spin wave propagation in the DE geometry is less frequency-selective and generally stronger attenuated across the structure compared to the BV case, with caustic spin wave beams partially playing a role in mediating the transmission across the ring.

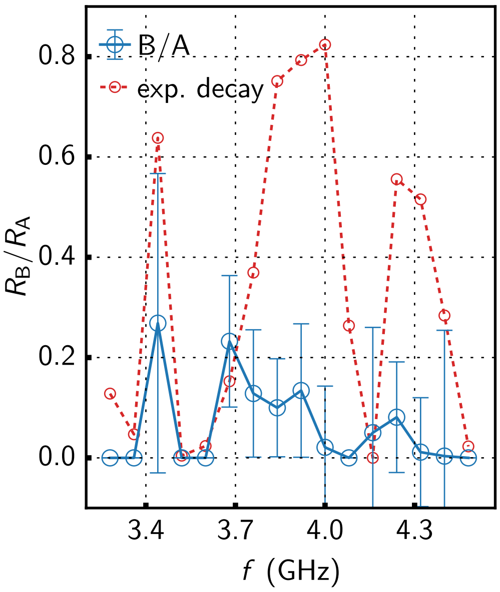

Figure 10.14. Transmission parameter $R_\mathrm{B}/R_\mathrm{A}$ in the DE geometry. Experimental values with error bars exceeding 0.35 were set to zero, and no error bar is shown for better visualization.

Summary

This thesis investigated spin wave propagation in 200 nm thick yttrium iron garnet (YIG) films, which provide a great magnonic playground due to their low magnetic damping. The primary experimental focus was on the investigation of spin wave caustics, the hybridization of propagating spin wave modes with perpendicular standing spin waves (PSSWs) in trapezoidal waveguides, and spin wave propagation in ring-shaped waveguides.

The first set of experiments studied the properties of caustic spin wave beams (CSWBs), which emerge due to anisotropies in the spin wave dispersion relation. These anisotropies can give rise to stationary group velocity directions at certain points on the iso-frequency curve. A Python-based toolkit was developed to systematically analyze beam properties such as beam direction, wavenumber, and wavefront angle as a function of frequency and magnetic field. Using time-resolved Kerr microscopy (TR-MOKE), the theoretical predictions were tested in the low-frequency pocket, a region in frequency and magnetic field space where the predicted caustic points exhibit relatively low wavenumbers. Half-ring microstrip antennas and YIG antidots were used to excite a wide angular portion of the iso-frequency curve, providing access to the caustic points. The observed spin wave beam properties showed good agreement with theoretical predictions, suggesting that they were indeed CSWBs, and demonstrating the ability to tailor spin wave beams.

In addition, the reflection of CSWBs at the edges of a magnonic waveguide was investigated as a function of the external magnetic field and its angle. The reflection experiments showed that the reflection efficiency varied with the external magnetic field, and the spin wave beams could be steered by adjusting angle of the external magnetic field. Moreover, the reflections did not follow Snell's law for spin waves. In particular, the incoming angle was not equal to the outgoing angle with respect to the reflection interface, as the position of the caustic points on the iso-frequency curve determined the reflection behavior.

In the second set of experiments, the hybridization of Damon-Eshbach-like spin wave modes with perpendicular standing spin waves (PSSWs) in trapezoidal magnonic waveguides was investigated. This hybridization, marked by an anticrossing in the spin wave dispersion relation, leads to significant attenuation of spin wave propagation. Micromagnetic simulations revealed that the effective magnetic field gradually decreases along the center of the waveguide due to geometry-induced demagnetizing effects. TR-MOKE experiments demonstrated that the combination of mode hybridization and the geometry-induced inhomogeneous magnetic field distribution allows for continuous control over the spin wave propagation distance by adjusting the external magnetic field. The hybridization regime is accessed locally at different points along the waveguide. Altering the waveguide geometry further influenced the sensitivity of this effect. Building on these results, all-electrical vector network analyzer (VNA) spin wave spectroscopy further demonstrated the ability to control electrical transmission between microstrip antennas positioned along the trapezoid waveguide.

The third set of experiments investigated spin wave propagation in a ring-shaped magnonic waveguide connected to a stripe section, focusing on frequency-dependent transmission. Super-Nyquist sampling MOKE (SNS-MOKE) was used to study spin wave behavior in both Backward-Volume (BV) and Damon-Eshbach (DE) configurations. In the stripe section, mostly one spin wave mode was present, while in the ring section, multiple modes emerged and were quantized due to the finite width of the waveguide. Demagnetizing effects near and within the ring section further impacted spin wave propagation. Frequency-dependent transmission across the ring structure was found, with a particular sharp frequency selectivity in the BV configuration. A simple exponential decay of spin wave amplitude could not explain transmission suppression at various frequencies. Instead, the transmission properties were likely influenced by complex interference and scattering of spin wave modes within the ring section. Additionally, in the DE configuration, transmission was further suppressed over a specific frequency range due to hybridization effects with PSSWs.

The findings from these experiments provide valuable insights into spin wave manipulation. Caustic beams, with their high amplitude and tunability, show great promise for focused energy transfer. Control over hybridization effects enables localized tuning of spin wave attenuation and propagation distance, which is particularly useful for magnonic logic gates. Furthermore, the behavior of spin waves in ring structures demonstrates their potential for frequency-selective filtering. Overall, this thesis lays a solid foundation for advancing magnonic applications and demonstrates the versatility of spin wave manipulation through beam shaping, hybridization control, and frequency filtering.

Appendix

A. Extraction of Beam Parameters

A.1. Explanation and Example

The following shows a detailed guide on how the beam parameters were extracted in the simulations and experiments in part II.

The values of $\theta_{\mathrm{v,e}}$, k_{e}, and φ_{e} in the experiments are determined through image processing and fitting analysis. All the errors are calculated via a bootstrapping procedure. This involves normally distributed random data generated from the standard deviation of the residual of an initial fit, subsequently adding this random data to the original data, and then repeating the fit and parameter calculation 100 times. Twice the standard deviation of the resulting parameters is used as the error bar for the fit parameters.

An exemplary analysis is conducted for experimentally obtained beams (cf. Section 6.1) under $f = 1.44\,\mathrm{GHz}$ and $\mu_0 H = 5\,\mathrm{mT}$, excited by the half-ring antenna (see Fig. A.1(a)). First, the beam direction is evaluated. To this end, distinct edges are identified in the Kerr image using a so-called Canny edge detection algorithm [191] with suitable hysteresis thresholding. Essentially, this results in a set of lines representing the beam wavefronts. The two beam branches are fitted separately with a linear model as illustrated in Fig. A.1(b), yielding a beam direction of $(119.0 \pm 1.2)^\circ$ for beam I and $(115.7 \pm 1.4)^\circ$ for beam II. Note that all angular values are projected to the first quadrant of the iso-frequency curve.

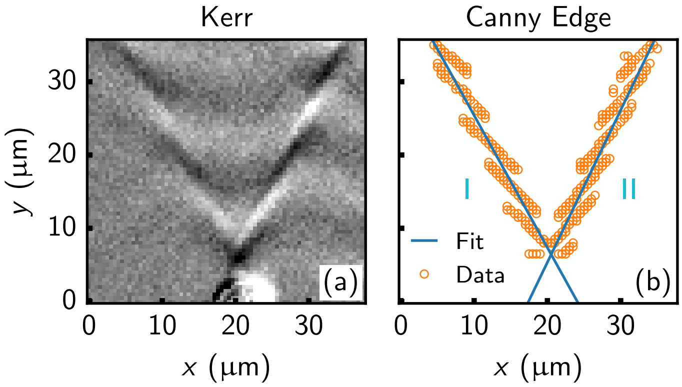

Figure A.1. Image processing and fitting to extract beam direction. A Canny Edge detection algorithm is applied on the Kerr image in (a), and the resulting edge points are fitted in (b).

Next, the wavefront angle and wavenumber are specified. Each beam is subjected to a mask centered around the previously found straight-line fits. Note that the sharpness of the mask is determined by eye to best isolate the beams. The contours of the masks are sketched in the Kerr image in Fig. A.2. Each isolated beam is then rotated to align with the x-axis.

This data is subsequently fitted individually with a 2D plane wave model of the form:

$$f(x,y) = A \cdot \sin\left(kx \cdot \cos\left(\varphi_{\mathrm{fit}}\right) + ky \cdot \sin\left(\varphi_{\mathrm{fit}}\right) + \delta\right) \cdot \mathrm{e}^{-\frac{x}{L_{\mathrm{att}}} \cdot \cos\left(\varphi_{\mathrm{fit}}\right) - \frac{y}{L_{\mathrm{att}}} \cdot \sin\left(\varphi_{\mathrm{fit}}\right)}. \tag{A.1}$$

In this model, x and y are the coordinates, A represents the amplitude, k is the wavenumber, φ_{fit} is the wavefront angle of the rotated data, δ is the phase, and L_{att} represents the attenuation length.

A set of data and fits is displayed in Fig. A.2. The wavefront angles are obtained by projecting the fit angle φ_{fit} back to the beam direction. Thus for the given example, the fitting procedure yields $k_{\mathrm{I}} = (1.04 \pm 0.07)\ \mu\mathrm{m}^{-1}$, and $\varphi_{\mathrm{I}} = (52.4 \pm 1.9)^{\circ}$, and $k_{\mathrm{II}} = (1.07 \pm 0.09)\ \mu\mathrm{m}^{-1}$, and $\varphi_{\mathrm{II}} = (48.9 \pm 2.1)^{\circ}$. Regarding the apparent wavenumber, k_{app} was extracted from a sinusoidal one-dimensional fit of each line of the rotated beams, resulting in $k_{\mathrm{I,app}} = (0.41 \pm 0.01)^{\circ}$ and $k_{\mathrm{II,app}} = (0.43 \pm 0.04)^{\circ}$.

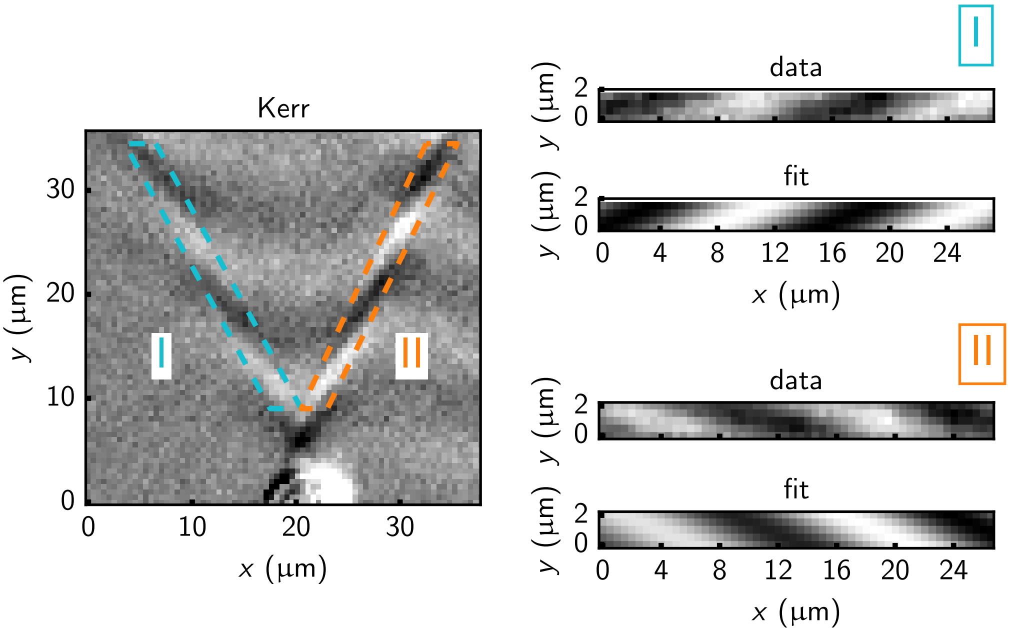

Figure A.2. Extraction of wavenumber and wavefront angle. Each beam, I and II, is isolated and fitted separately.

In Sections 4.5 and 6.1, two beams are always analyzed, yielding two sets of error bars and means for $\theta_{\mathrm{v,e}}$, k_{e}, and φ_{e} for any experimental value. As in those sections, the focus is on the general caustic properties, the means of the two beams are combined to yield $\theta_{\mathrm{v,e}} = (117.4 \pm 2.1)^{\circ}$, $k_{\mathrm{e}} = (1.06 \pm 0.08)\ \mu\mathrm{m}^{-1}$, $\varphi_{\mathrm{e}} = (50.7 \pm 2.6)^{\circ}$, and $k_{\mathrm{e,app}} = (0.42 \pm 0.03)\ \mu\mathrm{m}^{-1}$. Thus, the error bars eventually shown in these two sections not only measure the fit quality but also consider the deviation in experimental parameters between the two caustic branches. In the reflection experiments discussed in Section 6.4, the beam parameters are shown individually unless stated otherwise.

Note that in the Kerr images from the experiments using antidots as scatter sources, difficulties were encountered in identifying the beam direction due to the strong plane wave background. To resolve this, an additional FT filter was applied: specific portions of the data were set to 0 zero in reciprocal space, and the images were transformed back to real space, eliminating the plane waves. An example of unfiltered and filtered Kerr images is provided in Fig. A.3. Subsequently, the extraction procedure was conducted on twin beams, which were emitted from the 5 µm antidot (antidot in the middle) and oriented in different forward directions.

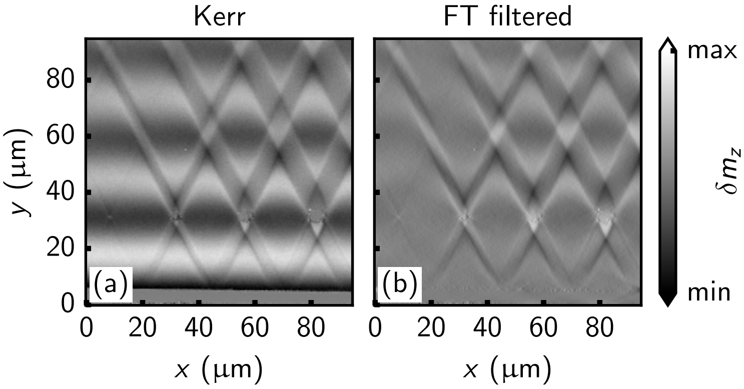

Figure A.3. (a) Kerr map for antidot geometry under $f = 1.44\,\text{GHz}$, $\mu_0 H = 5\,\text{mT}$. (b) FT filtered image.

Similarly, in Section 6.4, solely applying the Canny edge detection and fitting the beam direction with a straight line proved challenging. The presence of edges and the intersections of beams at these edges introduced additional points that did not correspond to the actual beam. This issue was addressed by using an initial linear estimate for each beam and only including points within a specified distance from this estimate in the linear fit model. This approach ensured a more accurate identification of the isolated beams.

A.2. Test of Procedure

Further considerations were made to naively assess the accuracy of the presented procedure and better understand the error bars. A 2D beam array with predefined properties of $\theta_\text{v} = 115.05°$, $k = 1.11\,\mu\text{m}^{-1}$, $\varphi = 51.29°$ and a sharpness of 2.5 µm was generated computationally. Gaussian-distributed random noise was added to this array, followed by the 2D wave fitting procedure. This procedure was repeated for different noise levels. The noise level was defined as the ratio between the standard deviation of the added Gaussian distribution and the plane wave amplitude.

The results in Figs. A.4(a)-(b) show that the mean fit parameters accurately reproduce the initial k and φ values, although the error bars increase with increasing noise level. The green line in Fig. A.4(c) further illustrates the trend of the error bars for φ.

These findings were compared to the noise levels of the experimental data. Here, only spin wave beam II is considered; hence, the deviation in fit parameters between the two beams is neglected. The resulting data points (red triangles) represent the error bars at the respective noise level of the experimental data. Mostly, the experimental error bars are in reasonable agreement with the simulated ones. Analogous analysis was carried out on the effect of beam sharpness and beam direction on the accuracy of the fitting procedure. The values of k and φ were reasonably restored, and only a significant effect on the error bars was found.

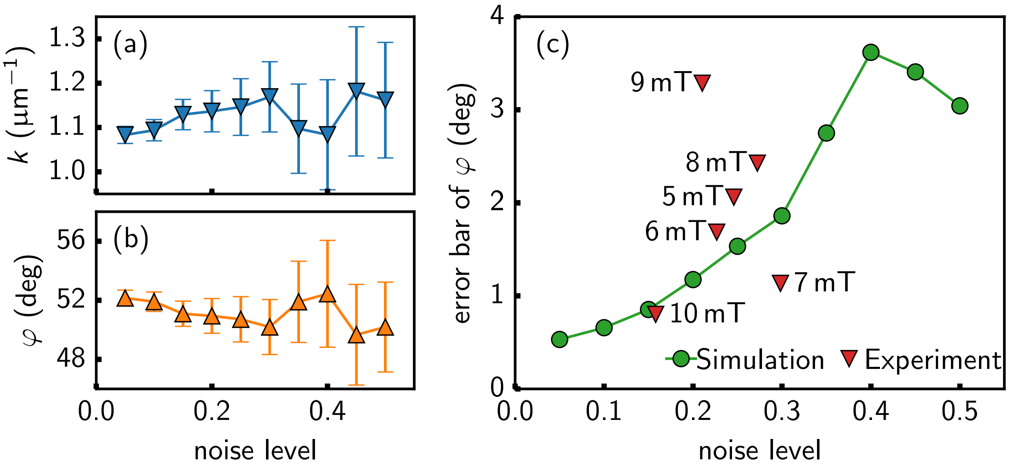

Figure A.4. Test of fitting procedure. (a) Fitted wavenumbers and (b) wavefront angles at different noise levels. (c) Behavior of the error bars with increasing noise level. The simulated error bar size (blue curve) increases with the noise level. Red triangles show experimental error bars for respective external magnetic field values.

B. Extraction of External Magnetic Field Angle from FT Data

Instead of extracting the external magnetic field angle from the deviation in the caustic beam direction, in Section 6.4 a different approach was applied. An offset of the external magnetic field direction effectively corresponds to a rotation of the iso-frequency curve in the experimental frame of reference. Thus, the external magnetic field angle should possibly be extracted from the FT data.

For this purpose, a function $\Omega(k_x, \alpha; f, H)$ was defined, which takes a k_x as an input and aims to find the corresponding k_y at the given rotation α on the slowness at the given frequency f and given applied field H. To be more specific, $\Omega(k_x, \alpha; f, H)$ first fully reconstructs the iso-frequency curve over the entire angular range for the given frequency and magnetic field as described in Ref. [26]. The algorithm effectively yields arrays of $k_{x,\mathrm{rec}}$ and $k_{y,\mathrm{rec}}$ which correspond to the iso-frequency curve. This set of wavenumbers is then rotated by the angle α using the transformation:

$$\begin{pmatrix} k_{x,\mathrm{rot}} \\ k_{y,\mathrm{rot}} \end{pmatrix} = \begin{pmatrix} \cos(\alpha) & -\sin(\alpha) \\ \sin(\alpha) & \cos(\alpha) \end{pmatrix} \begin{pmatrix} k_{x,\mathrm{rec}} \\ k_{y,\mathrm{rec}} \end{pmatrix}. \tag{B.1}$$

From the rotated $k_{x,\mathrm{rot}}$ the value closest to the input k_x is extracted and the corresponding k_y is returned by the function $\Omega(k_x, \alpha; f, H)$. This procedure allows for the extraction of the corresponding k_y for each input k_x at an arbitrary field angle.

To extract the external magnetic field angle from the FT data, a local peak detection is first applied to the FT image, yielding the coordinates of the experimental iso-frequency curve. The experimental iso-frequency curve then undergoes a fitting procedure with the function $\Omega(k_x, \alpha; f, H)$ to determine the external magnetic field angle α_H. The standard deviation of the fit serves as the error bars, providing a measure of the fit's accuracy. Note that for the fitting procedure, only the portions of the FT data and $\Omega(k_x, \alpha; f, H)$ with $k_y > 0$ were considered to avoid ambiguities. An example of a fitting procedure is illustrated in Figs. B.1(a)-(c).

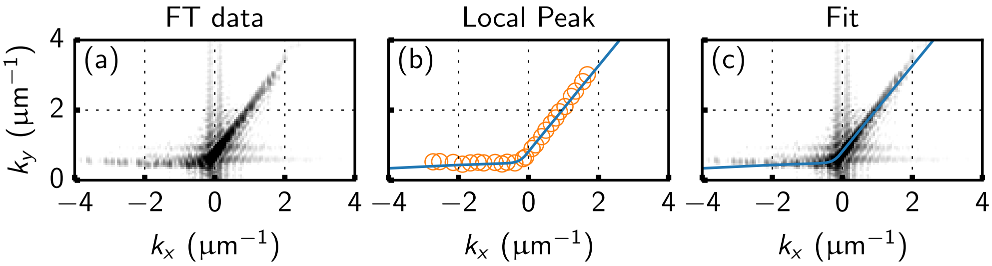

Figure B.1. Extraction of the external magnetic field angle from the FT data. (a) FT data obtained from the Kerr map. (b) Orange points correspond to the points extracted from FT data using local peak detection, while the blue curve represents the iso-frequency curve obtained from the fitting procedure using the function $\Omega(k_x, \alpha; f, H)$. An angle $\alpha_H = (26.6 \pm 1.1)^\circ$ was determined in this example. (c) FT data overlaid with the fitted iso-frequency curve.

C. Analysis of the Phase Shift in Caustic Spin Wave Beam Reflection Experiments

In the following, an attempt is made to analyze the phase shift of CSWBs upon reflection at the magnonic waveguide edges, as discussed in Section 6.4.1. However, this analysis is complicated by several experimental uncertainties, as detailed at the end of Section 6.4.1.

Neglecting the attenuation length, an incoming caustic spin wave beam may be described by a 2D plane wave of the form:

$$\Psi_{\mathrm{c,in}} = A_{\mathrm{c,in}} \cdot \sin\left(k_{\mathrm{c,in}} x \cdot \cos\left(\varphi_{\mathrm{c,in}}\right) + k_{\mathrm{c,in}} y \cdot \sin\left(\varphi_{\mathrm{c,in}}\right) + \delta_{\mathrm{c,in}}\right), \tag{C.1}$$

and an outgoing caustic spin wave beam by:

$$\Psi_{\mathrm{c,out}} = A_{\mathrm{c,out}} \cdot \sin\left(k_{\mathrm{c,out}} x \cdot \cos\left(-\varphi_{\mathrm{c,out}}\right) + k_{\mathrm{c,out}} y \cdot \sin\left(-\varphi_{\mathrm{c,out}}\right) + \delta_{\mathrm{c,out}}\right)). \tag{C.2}$$

Here, $A_{\mathrm{c,in}}$ and $A_{\mathrm{c,out}}$ denote the wave amplitudes, and $\delta_{\mathrm{c,in}}$ and $\delta_{\mathrm{c,out}}$ represent arbitrary phases. The subscript "c" refers to the parameters of the carrier wave of the beam. The negative sign in front of $\varphi_{\mathrm{c,out}}$ indicates that, upon reflection at the edge, the k_y component changes sign.

From Eqs. (C.1) and (C.2), the phase difference upon reflection at a specific point (x_0, y_0) in space can be calculated as:

$$\begin{aligned} \Delta\phi_{\mathrm{c}} = \Big| & \left[k_{\mathrm{c,in}} \cos\left(\varphi_{\mathrm{c,in}}\right) - k_{\mathrm{c,out}} \cos\left(\varphi_{\mathrm{c,out}}\right)\right] \cdot x_0 \\ & + \left[k_{\mathrm{c,in}} \sin\left(\varphi_{\mathrm{c,in}}\right) + k_{\mathrm{c,out}} \sin\left(\varphi_{\mathrm{c,out}}\right)\right] \cdot y_0 \\ & + \delta_{\mathrm{c,in}} - \delta_{\mathrm{c,out}} \Big|. \end{aligned} \tag{C.3}$$

Instead of considering the 2D plane wave model, the phase shift can also be interpreted in terms of the apparent wavelength (cf. Section 4.2) along the beam direction s. Here, the incoming and outgoing waves are modeled by:

$$\Psi_{\mathrm{app,in}} = A_{\mathrm{app,in}} \cdot \sin(k_{\mathrm{app,in}} s + \delta_{\mathrm{app,in}}), \tag{C.4}$$

$$\Psi_{\mathrm{app,out}} = A_{\mathrm{app,out}} \cdot \sin(k_{\mathrm{app,out}} s + \delta_{\mathrm{app,out}}), \tag{C.5}$$

where the subscript "app" denotes the apparent beam parameters, namely wavenumber and arbitrary phase. The resulting phase shift is then expressed as:

$$\Delta\phi_{\mathrm{app}} = (k_{\mathrm{app,in}} - k_{\mathrm{app,out}}) s + \delta_{\mathrm{app,in}} - \delta_{\mathrm{app,out}}. \tag{C.6}$$

Given that the carrier wave and the apparent wave of the beam are expected to exhibit the same magnitude at a particular edge point, the condition $\Delta\phi_{\mathrm{c}} = \Delta\phi_{\mathrm{app}}$ should hold at the edge, indicating that both approaches are theoretically equivalent and should yield consistent results.

With the theoretical framework established, we can now turn our attention to the analysis of the experimental data. Fig C.1(a) presents the experimentally acquired CSWB reflection at the upper edge of the magnonic waveguide under an external magnetic field of $\mu_0 H = 5\,\mathrm{mT}$ (cf. 6.12(e)). The dashed cyan and red contours indicate the extracted beams. The edge of the waveguide, identified using a Laplacian of Gaussian (LoG) filter applied to the topographic map, is marked by a dashed orange line. A detailed explanation of the LoG edge detection procedure can be found in Appendix D. The bold orange segment in the figure highlights the coordinates where the beams reflect, determined by the overlap of the incoming and outgoing beam contours.

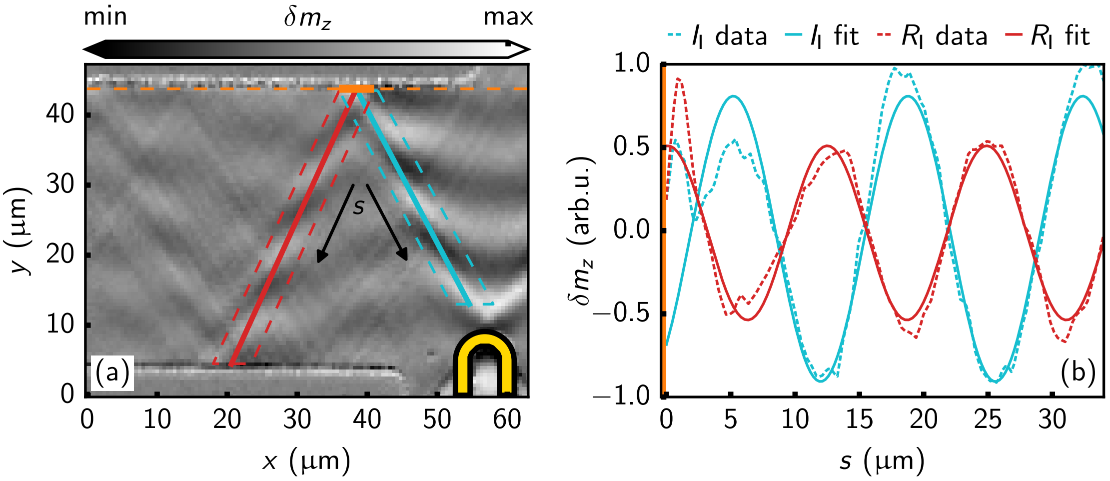

Figure C.1. Phase shift upon reflection at $\mu_0 H = 5\,\mathrm{mT}$. (a) Kerr map illustrating beams I_I (dashed cyan contour) and R_I (dashed red contour). The orange dashed line represents the position of the edge as extracted from the topography. The bold orange segment highlights the coordinates of the reflection site, which are considered in the analysis. (b) Profiles and apparent wavelength fits along the cyan and red lines in (a), with s representing the direction along the beams. The position at $0\,\mu\mathrm{m}$ corresponds to the reflection edge point. A phase shift between the incoming and reflected apparent wave is observed.

Figure C.1(b) illustrates the phase shift between the incoming beam I_I and the reflected beam R_I by displaying their line profiles (dotted lines) and corresponding apparent wavenumber fits (solid lines) along the cyan and red lines, respectively, as indicated in Figure C.1(a). The fits were applied to portions of the beams away from the edge where the beams intersect. The fit data clearly shows a phase shift between the apparent waves of I_I and R_I at the reflection edge ($s = 0\,\mu\mathrm{m}$).

The phase shift in terms of $\Delta\phi_\mathrm{app}$ can be calculated for each point across the line where the beams reflect, yielding an average phase shift. Fig C.2(a) presents the averaged phase shift for CSWBs under various external magnetic field strengths with the phase shift represented within the interval $-\pi$ to π. Additionally, the phase shift $\Delta\phi_c$, derived from the carrier wave parameters[1], is shown in Fig C.2(b). Both approaches yield comparable results, with most data points falling within the error bars.

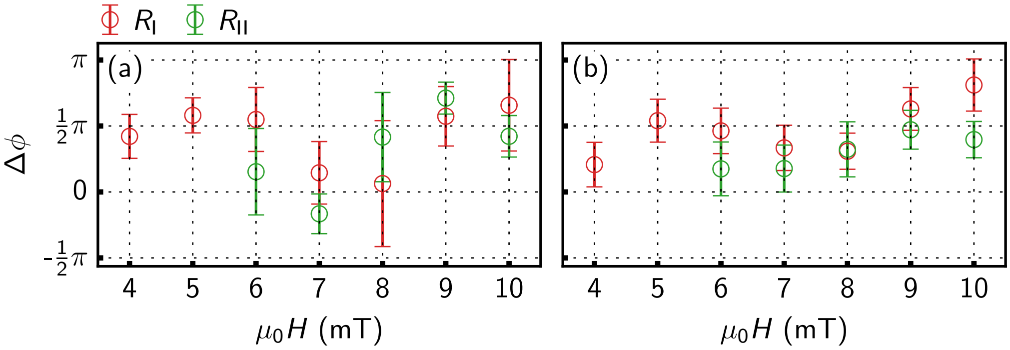

Figure C.2. (a) Phase difference extracted from apparent wavenumber fit. (b) Phase difference extracted from 2D plane wave fits of the beams. Error bars include uncertainty in edge position and fit parameters.

The phase shift observed upon reflection of the CSWBs varies with the external magnetic field, although no definitive trend is apparent. The phase shift ranges from close to 0 to close π, with π corresponding to fully pinned boundary states and 0 indicating totally unpinned boundary conditions at the reflection edge [56]. This could imply that the boundaries at the reflection interface exhibit mixed or partially pinned conditions, potentially due to the imperfect YIG boundary (cf. AFM images in Section 8.5). Additionally, the phase shifts at the lower edge of the waveguide generally fall within the error bars of those observed at the upper edge, indicating similar pinning conditions at both edges. However, as previously noted, the observed phase shift could also just be an artifact of the experimental limitations, such as the finite Wwdth of the CSWBs, misalignments of the reflection edge, and multiple wavenumbers contributing to the beam.

---

[1] Note that here, L_{att} was considered in the fitting parameters as opposed to the apparent wavelength approach where it is cumbersome to assign an attenuation length.

D. Edge Detection from a Topographic Image

Fig. D.1(a) shows a typical topographic image from Section 6.4, where a magnonic waveguide is located on the left of the half-ring antenna. Fig. D.1(b) shows a line profile across the dotted orange line in Fig. D.1(a). To determine the edges of the waveguide, the edge positions were identified seperately with a Laplacian of Gaussian (LoG) edge detection method [192, 193]. The LoG filter process involves first applying a Gaussian filter to smooth the data, followed by the application of the Laplace operator. A more detailed description of edge detection processes can be found in Ref. [193].

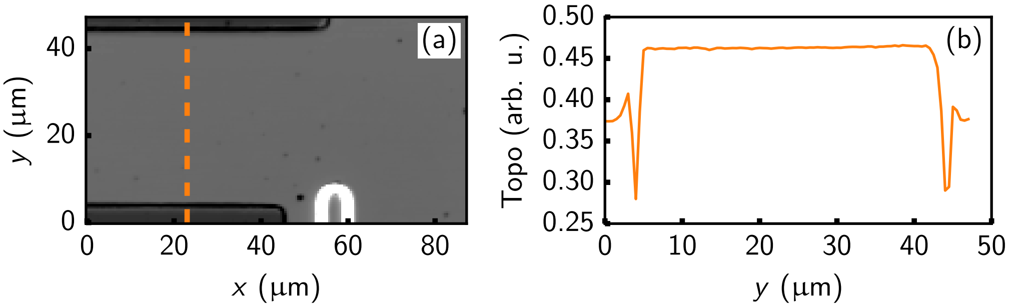

Figure D.1. (a) Optically acquired topographic map of typical sample. (b) Line profile across the dotted orange line in (a).

In Fig. D.1(b), at the edges, a transition from low to high amplitude or vice versa is observed. However, a distinct minimum is observed at each edge. As the AFM data in a similar system in Section 8.5 shows no such sharp features, the minimum presumably stems from diffraction and scattering processes at the edges.

Fig. D.2(a) shows the first edge from the line profile in Fig. D.1(b). Fig. D.2(b) displays data obtained by applying the LoG filter to the profile in Fig. D.2(a). The physical edge of the system is assumed to lie at the midpoint of the transition from the minimum to the maximum, corresponding to the point of maximal slope. By applying the LoG filter to the line profile, which essentially results in the second derivative of the line profile, the edges should be located at the zero-crossing of the LoG-processed data.

However, due to the limited pixel size of the recorded topographic images (typically with a step size of 0.5 µm), the zero-crossing is determined by further fitting of the LoG-processed data with a Ricker wavelet function, or "Mexican hat" wavelet function, given by [193]:

$$f_{\text{Ricker}}(x) = A\left(1 - \frac{(x-x_0)^2}{2\sigma^2}\right) \mathrm{e}^{-\frac{(x-x_0)^2}{2\sigma^2}}, \tag{D.1}$$

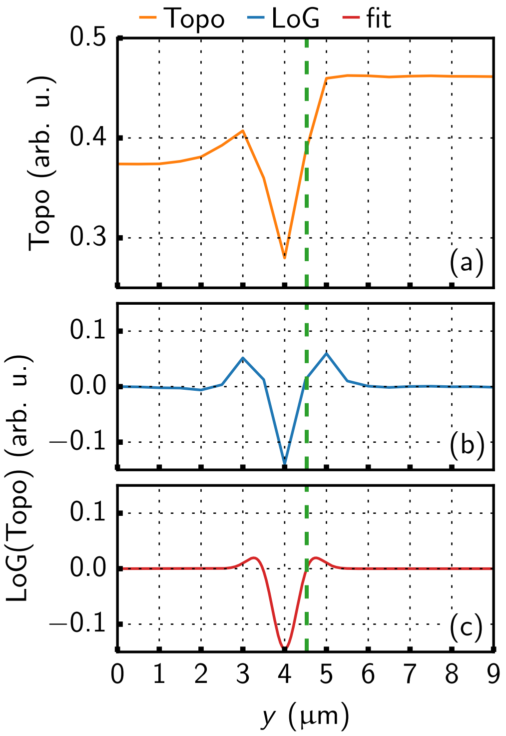

Figure D.2. Edge detection with Laplacian of Gaussian (LoG) filter. (a) Profile of the first edge from Fig. D.1(b). (b) Data obtained by applying the LoG filter to the edge profile. (c) Fit of the LoG-processed data with the Ricker wavelet function. The green dashed line represents the zero-crossing of the fitted LoG-filtered data, corresponding to the edge in the topographic line profile.

where A describes the amplitude, x_0 is the center position of the wavelet, and σ is the standard deviation that determines the width of the wavelet.

The corresponding Ricker fit is shown in Fig. D.2(c). From this fit, the zero-crossing corresponding to the edge in the topographic image is extracted. The green vertical line in Figs. D.2(a)-(c) illustrates the extracted edge position, which in this example is determined to be 4.47 ± 0.01 µm. In an analogous approach, the position of the upper edge is determined.

The edge detection process can be repeated for each line profile across the waveguide width. The distance between the two detected edges then gives the nominal waveguide width, which in this case is found to be $w_{\mathrm{wg}} = (39.18 \pm 0.10), \mu\mathrm{m}$.

Bibliography

[1] B. Flebus et al., "The 2024 magnonics roadmap", J. Phys.: Condens. Matter **36**, 363501 (2024).

[2] A. A. Serga, A. V. Chumak, and B. Hillebrands, "YIG magnonics", J. Phys. D: Appl. Phys. **43**, 264002 (2010).

[3] M. Krawczyk and D. Grundler, "Review and prospects of magnonic crystals and devices with reprogrammable band structure", J. Phys.: Condens. Matter **26**, 123202 (2014).

[4] A. V. Chumak, V. I. Vasyuchka, A. A. Serga, and B. Hillebrands, "Magnon spintronics", Nat. Phys. **11**, 453–461 (2015).

[5] A. Barman et al., "The 2021 magnonics roadmap", J. Phys.: Condens. Matter **33**, 413001 (2021).

[6] A. V. Chumak et al., "Advances in magnetics roadmap on spin-wave computing", IEEE Trans. Magn. **58**, 1–72 (2022).

[7] F. Bloch, "Zur theorie des ferromagnetismus", Z. Phys. **61**, 206–219 (1930).

[8] T. Holstein and H. Primakoff, "Field dependence of the intrinsic domain magnetization of a ferromagnet", Phys. Rev. **58**, 1098–1113 (1940).

[9] F. J. Dyson, "General theory of spin-wave interactions", Phys. Rev. **102**, 1217–1230 (1956).

[10] C. Herring and C. Kittel, "On the theory of spin waves in ferromagnetic media", Phys. Rev. **81**, 869–880 (1951).

[11] C. Kittel, "Interaction of spin waves and ultrasonic waves in ferromagnetic crystals", Phys. Rev. **110**, 836–841 (1958).

[12] B. N. Brockhouse, "Scattering of neutrons by spin waves in magnetite", Phys. Rev. **106**, 859–864 (1957).

[13] H. Yu, O. d'Allivy Kelly, V. Cros, R. Bernard, P. Bortolotti, A. Anane, F. Brandl, F. Heimbach, and D. Grundler, "Approaching soft x-ray wavelengths in nanomagnet-based microwave technology", Nat Commun **7**, `10.1038/ncomms11255` (2016).

[14] G. Gubbiotti, S. Tacchi, M. Madami, G. Carlotti, A. O. Adeyeye, and M. Kostylev, "Brillouin light scattering studies of planar metallic magnonic crystals", J. Phys. D: Appl. Phys. **43**, 264003 (2010).

[15] Z. K. Wang, V. L. Zhang, H. S. Lim, S. C. Ng, M. H. Kuok, S. Jain, and A. O. Adeyeye, "Nanostructured magnonic crystals with size-tunable bandgaps", ACS Nano **4**, 643–648 (2010).

[16] M. A. Morozova, S. V. Grishin, A. V. Sadovnikov, D. V. Romanenko, Y. P. Sharaevskii, and S. A. Nikitov, “Band gap control in a line-defect magnonic crystal waveguide”, Appl. Phys. Lett. **107**, 242402 (2015).

[17] A. J. E. Kreil, H. Y. Musiienko-Shmarova, S. Eggert, A. A. Serga, B. Hillebrands, D. A. Bozhko, A. Pomyalov, and V. S. L’vov, “Tunable space-time crystal in room-temperature magnetodielectrics”, Phys. Rev. B **100**, `10.1103/physrevb.100.020406` (2019).

[18] F. Lisiecki et al., “Reprogrammability and scalability of magnonic fibonacci quasicrystals”, Phys. Rev. Applied **11**, `10.1103/physrevapplied.11.054003` (2019).

[19] K.-S. Lee and S.-K. Kim, “Conceptual design of spin wave logic gates based on a mach–zehnder-type spin wave interferometer for universal logic functions”, J. Appl. Phys. **104**, 053909 (2008).

[20] T. Goto, T. Yoshimoto, B. Iwamoto, K. Shimada, C. A. Ross, K. Sekiguchi, A. B. Granovsky, Y. Nakamura, H. Uchida, and M. Inoue, “Three port logic gate using forward volume spin wave interference in a thin yttrium iron garnet film”, Sci. Rep. **9**, `10.1038/s41598-019-52889-w` (2019).

[21] H. Qin, R. B. Holländer, L. Flajšman, F. Hermann, R. Dreyer, G. Woltersdorf, and S. van Dijken, “Nanoscale magnonic fabry-pérot resonator for low-loss spin-wave manipulation”, Nat Commun **12**, `10.1038/s41467-021-22520-6` (2021).

[22] Q. Wang et al., “A magnonic directional coupler for integrated magnonic half-adders”, Nature Electronics **3**, 765–774 (2020).

[23] Á. Papp, W. Porod, and G. Csaba, “Nanoscale neural network using non-linear spin-wave interference”, Nat Commun **12**, `10.1038/s41467-021-26711-z` (2021).

[24] A. Papp, G. Csaba, and W. Porod, “Characterization of nonlinear spin-wave interference by reservoir-computing metrics”, Appl. Phys. Lett. **119**, `10.1063/5.0048982` (2021).

[25] L. Körber, C. Heins, T. Hula, J.-V. Kim, S. Thlang, H. Schultheiß, and K. Schultheiß, *Data publication: pattern recognition in reciprocal space with a magnon-scattering reservoir*, 2023.

[26] A. Wartelle, F. Vilsmeier, T. Taniguchi, and C. H. Back, “Caustic spin wave beams in soft thin films: properties and classification”, Phys. Rev. B **107**, `10.1103/physrevb.107.144431` (2023).

[27] R. Gieniusz, H. Ulrichs, V. D. Bessonov, U. Guzowska, A. I. Stognii, and A. Maziewski, “Single antidot as a passive way to create caustic spin-wave beams in yttrium iron garnet films”, Appl. Phys. Lett. **102**, `10.1063/1.4795293` (2013).

[28] J.-V. Kim, R. L. Stamps, and R. E. Camley, “Spin wave power flow and caustics in ultrathin ferromagnets with the dzyaloshinskii-moriya interaction”, Phys. Rev. Lett. **117**, `10.1103/physrevlett.117.197204` (2016).

[29] M. Madami, Y. Khivintsev, G. Gubbiotti, G. Dudko, A. Kozhevnikov, V. Sakharov, A. Stal'makhov, A. Khitun, and Y. Filimonov, "Nonreciprocity of backward volume spin wave beams excited by the curved focusing transducer", Appl. Phys. Lett. **113**, `10.1063/1.5050347` (2018).

[30] Y. Shiota, S. Funada, R. Hisatomi, T. Moriyama, and T. Ono, "Imaging of caustic-like spin wave beams using optical heterodyne detection", Appl. Phys. Lett. **116**, `10.1063/5.0010410` (2020).

[31] I. Bertelli, J. J. Carmiggelt, T. Yu, B. G. Simon, C. C. Pothoven, G. E. W. Bauer, Y. M. Blanter, J. Aarts, and T. van der Sar, "Magnetic resonance imaging of spin-wave transport and interference in a magnetic insulator", Sci. Adv. **6**, `10.1126/sciadv.abd3556` (2020).

[32] S. Muralidhar, R. Khymyn, A. Awad, A. Alemán, D. Hanstorp, and J. Åkerman, "Femtosecond laser pulse driven caustic spin wave beams", Phys. Rev. Lett. **126**, `10.1103/physrevlett.126.037204` (2021).

[33] R. A. Gallardo, P. Alvarado-Seguel, A. Kákay, J. Lindner, and P. Landeros, "Spin-wave focusing induced by dipole-dipole interaction in synthetic antiferromagnets", Phys. Rev. B **104**, `10.1103/physrevb.104.174417` (2021).

[34] C. Riedel, T. Taniguchi, L. Körber, A. Kákay, and C. H. Back, "Hybridization-induced spin-wave transmission stop band within a 1d diffraction grating", Advanced Physics Research **2**, `10.1002/apxr.202200104` (2023).

[35] U. Makartsou, M. Gołebiewski, U. Guzowska, A. Stognij, R. Gieniusz, and M. Krawczyk, "Spin-wave self-imaging: experimental and numerical demonstration of caustic and talbot-like diffraction patterns", Appl. Phys. Lett. **124**, `10.1063/5.0195099` (2024).

[36] Y. Wang, W. Yan, N. Kuznetsov, L. Flajšman, H. Qin, and S. van Dijken, "Spin-wave diffraction, caustic beam emission, and talbot carpets in a yttrium iron garnet film with magnonic fabry-perot resonator gratings", Phys. Rev. Applied **22**, `10.1103/physrevapplied.22.014038` (2024).

[37] A. V. Vashkovskii, A. V. Stal'makhov, and D. G. Shakhnazaryan, "Formation, reflection, and refraction of magnetostatic wave beams", Soviet Physics Journal **31**, 908–915 (1988).

[38] V. N. Krivoruchko and A. S. Savchenko, "Controlled refraction and focusing of spin waves determined by the aharonov-casher effect", Phys. Rev. B **109**, `10.1103/physrevb.109.184437` (2024).

[39] D. Wagle et al., *Shaping non-reciprocal caustic spin-wave beams*, 2024.

[40] O. Büttner, M. Bauer, S. O. Demokritov, B. Hillebrands, Y. S. Kivshar, V. Grimalsky, Y. Rapoport, and A. N. Slavin, "Linear and nonlinear diffraction of dipolar spin waves in yttrium iron garnet films observed by space- and time-resolved brillouin light scattering", Phys. Rev. B **61**, 11576–11587 (2000).

[41] R. Khomeriki, "Self-focusing magnetostatic beams in thin magnetic films", Eur. Phys. J. B **41**, 219–222 (2004).

[42] V. Veerakumar and R. E. Camley, "Magnon focusing in thin ferromagnetic films", Phys. Rev. B **74**, `10.1103/physrevb.74.214401` (2006).

[43] V. E. Demidov, S. O. Demokritov, D. Birt, B. O'Gorman, M. Tsoi, and X. Li, "Radiation of spin waves from the open end of a microscopic magnetic-film waveguide", Phys. Rev. B **80**, `10.1103/physrevb.80.014429` (2009).

[44] T. Schneider, A. A. Serga, A. V. Chumak, C. W. Sandweg, S. Trudel, S. Wolff, M. P. Kostylev, V. S. Tiberkevich, A. N. Slavin, and B. Hillebrands, "Nondiffractive subwavelength wave beams in a medium with externally controlled anisotropy", Phys. Rev. Lett. **104**, `10.1103/physrevlett.104.197203` (2010).

[45] M. P. Kostylev, A. A. Serga, and B. Hillebrands, "Radiation of caustic beams from a collapsing bullet", Phys. Rev. Lett. **106**, `10.1103/physrevlett.106.134101` (2011).

[46] T. Sebastian, T. Brächer, P. Pirro, A. A. Serga, B. Hillebrands, T. Kubota, H. Naganuma, M. Oogane, and Y. Ando, "Nonlinear emission of spin-wave caustics from an edge mode of a microstructured $Co_2Mn_{0.6}Fe_{0.4}Si$ waveguide", Phys. Rev. Lett. **110**, `10.1103/physrevlett.110.067201` (2013).

[47] F. Heussner, A. A. Serga, T. Brächer, B. Hillebrands, and P. Pirro, "A switchable spin-wave signal splitter for magnonic networks", Appl. Phys. Lett. **111**, `10.1063/1.4987007` (2017).

[48] F. Heussner, M. Nabinger, T. Fischer, T. Brächer, A. A. Serga, B. Hillebrands, and P. Pirro, "Frequency-division multiplexing in magnonic logic networks based on caustic-like spin-wave beams", physica status solidi (RRL) – Rapid Research Letters **12**, 1800409 (2018).

[49] F. Heussner et al., "Experimental realization of a passive gigahertz frequency-division demultiplexer for magnonic logic networks", physica status solidi (RRL) – Rapid Research Letters **14**, 1900695 (2020).

[50] S. A. Odintsov, E. N. Beginin, S. E. Sheshukova, and A. V. Sadovnikov, "Reconfigurable lateral spin-wave transport in a ring magnonic microwaveguide", JETP Lett. **110**, 430–435 (2019).

[51] S. Odintsov, S. Sheshukova, S. Nikitov, and A. Sadovnikov, "Lateral and vertical spin-wave transport in a multimode magnonic ring coupler", Phys. Rev. Applied **22**, `10.1103/physrevapplied.22.014042` (2024).

[52] Q. Wang, A. Hamadeh, R. Verba, V. Lomakin, M. Mohseni, B. Hillebrands, A. V. Chumak, and P. Pirro, "A nonlinear magnonic nano-ring resonator", npj Comput. Mater. **6**, `10.1038/s41524-020-00465-6` (2020).

[53] J. H. E. Griffiths, "Anomalous high-frequency resistance of ferromagnetic metals", Nature **158**, 670–671 (1946).

[54] W. A. Yager and R. M. Bozorth, "Ferromagnetic resonance at microwave frequencies", Phys. Rev. **72**, 80–81 (1947).

[55] C. Kittel, “On the theory of ferromagnetic resonance absorption”, Phys. Rev. **73**, 155–161 (1948).

[56] J. Stigloher, “Reflection and refraction of spin waves”, PhD thesis (Universität Regensburg, 2018).

[57] W. Brown, *Magnetostatic principles in ferromagnetism*, Selected topics in solid state physics (North-Holland Publishing Company, 1962).

[58] L. R. Walker, “Magnetostatic modes in ferromagnetic resonance”, Phys. Rev. **105**, 390–399 (1957).

[59] J. R. Eshbach and R. W. Damon, “Surface magnetostatic modes and surface spin waves”, Phys. Rev. **118**, 1208–1210 (1960).

[60] R. Damon and J. Eshbach, “Magnetostatic modes of a ferromagnet slab”, J. Phys. Chem. Solids **19**, 308–320 (1961).

[61] B. Hillebrands and K. Ounadjela, eds., *Spin dynamics in confined magnetic structures II* (Springer Berlin Heidelberg, 2003).

[62] G. Bertotti, I. D. Mayergoyz, and C. Serpico, “Basic equations for magnetization dynamics”, in *Nonlinear magnetization dynamics in nanosystems* (Elsevier, 2009), pp. 21–34.

[63] T. N. G. Meier, “Static and dynamic properties of chiral magnetic textures in systems with broken inversion symmetry”, en, PhD thesis (Universität Regensburg, 2018).

[64] J. M. D. Coey, *Magnetism and magnetic materials* (Cambridge University Press, 2010).

[65] S. Blundell, *Magnetism in condensed matter*, Oxford Master Series in Condensed Matter Physics (OUP Oxford, 2001).

[66] A. Vansteenkiste, J. Leliaert, M. Dvornik, M. Helsen, F. Garcia-Sanchez, and B. V. Waeyenberge, “The design and verification of MuMax3”, AIP Advances **4**, 107133 (2014).

[67] G. S. Abo, Y.-K. Hong, J. Park, J. Lee, W. Lee, and B.-C. Choi, “Definition of magnetic exchange length”, IEEE Transactions on Magnetics **49**, 4937–4939 (2013).

[68] L. D. Landau and E. Lifshitz, “On the theory of the dispersion of magnetic permeability in ferromagnetic bodies”, Phys. Z. Sowjet. **8**, 153 (1935).

[69] Y. Henry, O. Gladii, and M. Bailleul, *Propagating spin-wave normal modes: a dynamic matrix approach using plane-wave demagnetizating tensors*, 2016.

[70] B. A. Kalinikos and A. N. Slavin, “Theory of dipole-exchange spin wave spectrum for ferromagnetic films with mixed exchange boundary conditions”, J. Phys. C: Solid State Phys. **19**, 7013–7033 (1986).

[71] G. Rado and J. Weertman, “Spin-wave resonance in a ferromagnetic metal”, J. Phys. Chem. Solids **11**, 315–333 (1959).

[72] R. F. Soohoo, “General exchange boundary condition and surface anisotropy energy of a ferromagnet”, Phys. Rev. **131**, 594–601 (1963).

[73] A. Prabhakar and D. D. Stancil, *Spin waves-theory and applications* (Springer US, 2009).

[74] H. Puszkarski, “Theory of surface states in spin wave resonance”, Prog. Surf. Sci. **9**, 191–247 (1979).

[75] A. A. Semenov, S. F. Karmanenko, V. E. Demidov, B. A. Kalinikos, G. Srinivasan, A. N. Slavin, and J. V. Mantese, “Ferrite-ferroelectric layered structures for electrically and magnetically tunable microwave resonators”, Appl. Phys. Lett. **88**, `10.1063/1.2166489` (2006).

[76] M. Collet et al., “Spin-wave propagation in ultra-thin yig based waveguides”, Appl. Phys. Lett. **110**, `10.1063/1.4976708` (2017).

[77] K. J. Harte, “Theory of magnetization ripple in ferromagnetic films”, J. Appl. Phys. **39**, 1503–1524 (1968).

[78] E. H. Lock, “The properties of isofrequency dependences and the laws of geometrical optics”, Phys.-Uspekhi **51**, 375 (2008).

[79] H. S. Körner, “Time-resolved kerr microscopy of spin waves propagating in magnetic nanostructures”, PhD thesis (2019).

[80] L. Körber, “Spin waves in curved magnetic shells”, PhD thesis (Sachsische Landesbibliothek, Staats- und Universitatsbibliothek Dresden, 2023).

[81] M. Kostylev, “Non-reciprocity of dipole-exchange spin waves in thin ferromagnetic films”, J. Appl. Phys. **113**, `10.1063/1.4789962` (2013).

[82] L. Körber, A. Hempel, A. Otto, R. Gallardo, Y. Henry, J. Lindner, and A. Kákay, *Finite-element dynamic-matrix approach for propagating spin waves: extension to mono- and multilayers of arbitrary spacing and thickness*, 2022.

[83] M. van Kampen, C. Jozsa, J. T. Kohlhepp, P. LeClair, L. Lagae, W. J. M. de Jonge, and B. Koopmans, “All-optical probe of coherent spin waves”, Phys. Rev. Lett. **88**, `10.1103/physrevlett.88.227201` (2002).

[84] A. Kirilyuk, A. V. Kimel, and T. Rasing, “Ultrafast optical manipulation of magnetic order”, Rev. Mod. Phys. **82**, 2731–2784 (2010).

[85] Y. Hashimoto et al., “All-optical observation and reconstruction of spin wave dispersion”, Nat Commun **8**, `10.1038/ncomms15859` (2017).

[86] S. O. Demokritov, V. E. Demidov, O. Dzyapko, G. A. Melkov, A. A. Serga, B. Hillebrands, and A. N. Slavin, “Bose–einstein condensation of quasi-equilibrium magnons at room temperature under pumping”, Nature **443**, 430–433 (2006).

[87] T. Brächer, P. Pirro, T. Meyer, F. Heussner, B. Lägel, A. A. Serga, and B. Hillebrands, “Parallel parametric amplification of coherently excited propagating spin waves in a microscopic ni81fe19 waveguide”, Appl. Phys. Lett. **104**, `10.1063/1.4878848` (2014).

[88] V. Lauer et al., “Spin-transfer torque based damping control of parametrically excited spin waves in a magnetic insulator”, Appl. Phys. Lett. **108**, `10.1063/1.4939268` (2016).

[89] T. Brächer, P. Pirro, and B. Hillebrands, “Parallel pumping for magnon spintronics: amplification and manipulation of magnon spin currents on the micron-scale”, Phys. Rep. **699**, 1–34 (2017).

[90] V. E. Demidov, S. Urazhdin, and S. O. Demokritov, “Direct observation and mapping of spin waves emitted by spin-torque nano-oscillators”, Nat. Mater. **9**, 984–988 (2010).

[91] M. Madami, S. Bonetti, G. Consolo, S. Tacchi, G. Carlotti, G. Gubbiotti, F. B. Mancoff, M. A. Yar, and J. Åkerman, “Direct observation of a propagating spin wave induced by spin-transfer torque”, Nat. Nanotechnology **6**, 635–638 (2011).

[92] S. M. Mohseni et al., “Spin torque–generated magnetic droplet solitons”, Science **339**, 1295–1298 (2013).

[93] S. Urazhdin, V. E. Demidov, H. Ulrichs, T. Kendziorczyk, T. Kuhn, J. Leuthold, G. Wilde, and S. O. Demokritov, “Nanomagnonic devices based on the spin-transfer torque”, Nat. Nanotechnology **9**, 509–513 (2014).

[94] L. J. Cornelissen, J. Liu, R. A. Duine, J. B. Youssef, and B. J. van Wees, “Long-distance transport of magnon spin information in a magnetic insulator at room temperature”, Nat. Phys. **11**, 1022–1026 (2015).

[95] G. Talmelli, F. Ciubotaru, K. Garello, X. Sun, M. Heyns, I. P. Radu, C. Adelmann, and T. Devolder, “Spin-wave emission by spin-orbit-torque antennas”, Phys. Rev. Applied **10**, `10.1103/physrevapplied.10.044060` (2018).

[96] S. Wintz, V. Tiberkevich, M. Weigand, J. Raabe, J. Lindner, A. Erbe, A. Slavin, and J. Fassbender, “Magnetic vortex cores as tunable spin-wave emitters”, Nat. Nanotechnology **11**, 948–953 (2016).

[97] M. Voto, L. Lopez-Diaz, and E. Martinez, “Pinned domain wall oscillator as a tuneable direct current spin wave emitter”, Sci. Rep. **7**, `10.1038/s41598-017-13806-1` (2017).

[98] A. Ganguly and D. Webb, “Microstrip excitation of magnetostatic surface waves: theory and experiment”, IEEE Transactions on Microwave Theory and Techniques **23**, 998–1006 (1975).

[99] T. Schneider, A. A. Serga, T. Neumann, B. Hillebrands, and M. P. Kostylev, “Phase reciprocity of spin-wave excitation by a microstrip antenna”, Phys. Rev. B **77**, `10.1103/physrevb.77.214411` (2008).

[100] V. E. Demidov, M. P. Kostylev, K. Rott, P. Krzysteczko, G. Reiss, and S. O. Demokritov, “Excitation of microwaveguide modes by a stripe antenna”, Appl. Phys. Lett. **95**, `10.1063/1.3231875` (2009).

[101] A. V. Chumak, A. A. Serga, and B. Hillebrands, “Magnonic crystals for data processing”, J. Phys. D: Appl. Phys. **50**, 244001 (2017).

[102] A. Gurevich and G. Melkov, *Magnetization oscillations and waves* (CRC Press, 1996).

[103] M. Obstbaum, “Inverse spin hall effect in metallic heterostructures”, PhD thesis (2016).

[104] Y. Ding, T. J. Klemmer, and T. M. Crawford, “A coplanar waveguide permeameter for studying high-frequency properties of soft magnetic materials”, J. Appl. Phys. **96**, 2969–2972 (2004).

[105] M. A. W. Schoen, J. M. Shaw, H. T. Nembach, M. Weiler, and T. J. Silva, “Radiative damping in waveguide-based ferromagnetic resonance measured via analysis of perpendicular standing spin waves in sputtered permalloy films”, Phys. Rev. B **92**, `10.1103/physrevb.92.184417` (2015).

[106] T. Devolder, *Theory of propagating spin wave spectroscopy using inductive antennas: conditions for unidirectional energy flow*, 2023.

[107] O. Büttner, M. Bauer, A. Rueff, S. Demokritov, B. Hillebrands, A. Slavin, M. Kostylev, and B. Kalinikos, “Space- and time-resolved brillouin light scattering from nonlinear spin-wave packets”, Ultrasonics **38**, 443–449 (2000).

[108] S. Demokritov, “Brillouin light scattering studies of confined spin waves: linear and nonlinear confinement”, Phys. Rep. **348**, 441–489 (2001).

[109] F. Bencivenga, A. Battistoni, D. Fioretto, A. Gessini, J. R. Sandercock, and C. Masciovecchio, “A high resolution ultraviolet brillouin scattering set-up”, Rev. Sci. Instrum. **83**, `10.1063/1.4756690` (2012).

[110] T. Sebastian, K. Schultheiss, B. Obry, B. Hillebrands, and H. Schultheiss, “Micro-focused brillouin light scattering: imaging spin waves at the nanoscale”, Front. Phys. **3**, `10.3389/fphy.2015.00035` (2015).

[111] M. R. Freeman and W. K. Hiebert, “Stroboscopic microscopy of magnetic dynamics”, in *Topics in applied physics* (Springer Berlin Heidelberg), pp. 93–126.

[112] J. P. Park, P. Eames, D. M. Engebretson, J. Berezovsky, and P. A. Crowell, “Spatially resolved dynamics of localized spin-wave modes in ferromagnetic wires”, Phys. Rev. Lett. **89**, `10.1103/physrevlett.89.277201` (2002).

[113] Z. Liu, F. Giesen, X. Zhu, R. D. Sydora, and M. R. Freeman, “Spin wave dynamics and the determination of intrinsic damping in locally excited permalloy thin films”, Phys. Rev. Lett. **98**, `10.1103/physrevlett.98.087201` (2007).

[114] K. Perzlmaier, G. Woltersdorf, and C. H. Back, “Observation of the propagation and interference of spin waves in ferromagnetic thin films”, Phys. Rev. B **77**, `10.1103/physrevb.77.054425` (2008).

[115] H. G. Bauer, J.-Y. Chauleau, G. Woltersdorf, and C. H. Back, “Coupling of spinwave modes in wire structures”, Appl. Phys. Lett. **104**, 102404 (2014).

[116] C. Riedel, “Local control and manipulation of propagating spin waves studied by time-resolved kerr microscopy”, en, PhD thesis (Technische Universität München, 2023), p. 135.

[117] Y. Acremann, J. P. Strachan, V. Chembrolu, S. D. Andrews, T. Tyliszczak, J. A. Katine, M. J. Carey, B. M. Clemens, H. C. Siegmann, and J. Stöhr, “Time-resolved imaging of spin transfer switching: beyond the macrospin concept”, Phys. Rev. Lett. **96**, `10.1103/physrevlett.96.217202` (2006).

[118] M. Bolte et al., “Time-resolved x-ray microscopy of spin-torque-induced magnetic vortex gyration”, Phys. Rev. Lett. **100**, `10.1103/physrevlett.100.176601` (2008).

[119] M. Baumgartner et al., “Spatially and time-resolved magnetization dynamics driven by spin–orbit torques”, Nat. Nanotechnology **12**, 980–986 (2017).

[120] N. Träger, F. Groß, J. Förster, K. Baumgaertl, H. Stoll, M. Weigand, G. Schütz, D. Grundler, and J. Gräfe, “Single shot acquisition of spatially resolved spin wave dispersion relations using x-ray microscopy”, Sci. Rep. **10**, `10.1038/s41598-020-74785-4` (2020).

[121] M. Bailleul, D. Olligs, and C. Fermon, “Propagating spin wave spectroscopy in a permalloy film: a quantitative analysis”, Appl. Phys. Lett. **83**, 972–974 (2003).

[122] V. Vlaminck and M. Bailleul, “Current-induced spin-wave doppler shift”, Science **322**, 410–413 (2008).

[123] F. Ciubotaru, T. Devolder, M. Manfrini, C. Adelmann, and I. P. Radu, “All electrical propagating spin wave spectroscopy with broadband wavevector capability”, Appl. Phys. Lett. **109**, `10.1063/1.4955030` (2016).

[124] T. Devolder, G. Talmelli, S. M. Ngom, F. Ciubotaru, C. Adelmann, and C. Chappert, “Measuring the dispersion relations of spin wave bands using time-of-flight spectroscopy”, Phys. Rev. B **103**, `10.1103/physrevb.103.214431` (2021).

[125] C. Weiss, M. Bailleul, and M. Kostylev, “Excitation and reception of magnetostatic surface spin waves in thin conducting ferromagnetic films by coplanar microwave antennas. part i: theory”, J. Magn. Magn. Mater. **565**, 170103 (2023).

[126] M. J. Donahue and D. G. Porter, *Oommf user’s guide, version 1.0* (1999).

[127] L. Körber, G. Quasebarth, A. Hempel, F. Zahn, A. Otto, E. Westphal, R. Hertel, and A. Kakay, *Tetrax: finite-element micromagnetic-modeling package*, 2022.

[128] M. Grimsditch, L. Giovannini, F. Montoncello, F. Nizzoli, G. K. Leaf, and H. G. Kaper, “Magnetic normal modes in ferromagnetic nanoparticles: a dynamical matrix approach”, Phys. Rev. B **70**, `10.1103/physrevb.70.054409` (2004).

[129] W. Rave, R. Schäfer, and A. Hubert, “Quantitative observation of magnetic domains with the magneto-optical kerr effect”, J. Magn. Magn. Mater. **65**, 7–14 (1987).

[130] R. Schäfer, “Magneto-optical domain studies in coupled magnetic multilayers”, J. Magn. Magn. Mater. **148**, 226–231 (1995).

[131] Z. Q. Qiu and S. D. Bader, “Surface magneto-optic kerr effect”, Rev. Sci. Instrum. **71**, 1243–1255 (2000).

[132] D. A. Allwood, G. Xiong, M. D. Cooke, and R. P. Cowburn, “Magneto-optical kerr effect analysis of magnetic nanostructures”, J. Phys. D: Appl. Phys. **36**, 2175–2182 (2003).

[133] I. V. Soldatov and R. Schäfer, “Advanced MOKE magnetometry in wide-field kerr-microscopy”, J. Appl. Phys. **122**, `10.1063/1.5003719` (2017).

[134] R. Dreyer, N. Liebing, E. R. J. Edwards, A. Müller, and G. Woltersdorf, “Spin wave localization and guiding by magnon band structure engineering in yttrium iron garnet”, `10.48550/ARXIV.1803.04943` (2018).

[135] M. M. Decker, “Spin current induced control of magnetization dynamics”, `10.5283/EPUB.37166` (2018).

[136] *Principles of lock-in detectionand the state of the art*, tech. rep. (Zurich Instruments, 2016).

[137] R. Dreyer, A. F. Schäffer, H. G. Bauer, N. Liebing, J. Berakdar, and G. Woltersdorf, “Imaging and phase-locking of non-linear spin waves”, Nat Commun **13**, `10.1038/s41467-022-32224-0` (2022).

[138] V. E. Demidov and S. O. Demokritov, “Magnonic waveguides studied by microfocus brillouin light scattering”, IEEE Trans. Magn. **51**, 1–15 (2015).

[139] T. Brächer, O. Boulle, G. Gaudin, and P. Pirro, “Creation of unidirectional spin-wave emitters by utilizing interfacial dzyaloshinskii-moriya interaction”, Phys. Rev. B **95**, `10.1103/physrevb.95.064429` (2017).

[140] A. V. Chumak, *Fundamentals of magnon-based computing*, 2019.

[141] Y. A. Kravtsov and Y. I. Orlov, *Caustics, catastrophes and wave fields* (Springer Berlin, Heidelberg, 1993).

[142] S. D. M. White and M. Vogelsberger, “Dark matter caustics”, Mon. Not. R. Astron Soc. **392**, 281–286 (2009).

[143] D. Davydov and S. Troitsky, “Testing universal dark-matter caustic rings with galactic rotation curves”, Phys. Lett. B **839**, 137798 (2023).

[144] B. Taylor, H. J. Maris, and C. Elbaum, “Phonon focusing in solids”, Phys. Rev. Lett. **23**, 416–419 (1969).

[145] A. G. Every, “Effects of first-order spatial dispersion on phonon focusing: application to quartz”, Phys. Rev. B **36**, 1448–1456 (1987).

[146] I. Epstein and A. Arie, “Arbitrary bending plasmonic light waves”, Phys. Rev. Lett. **112**, `10.1103/physrevlett.112.023903` (2014).

[147] X. Shi, X. Lin, F. Gao, H. Xu, Z. Yang, and B. Zhang, “Caustic graphene plasmons with kelvin angle”, Phys. Rev. B **92**, `10.1103/physrevb.92.081404` (2015).

[148] J. Spector, H. L. Stormer, K. W. Baldwin, L. N. Pfeiffer, and K. W. West, “Electron focusing in two-dimensional systems by means of an electrostatic lens”, Appl. Phys. Lett. **56**, 1290–1292 (1990).

[149] V. V. Cheianov, V. Fal’ko, and B. L. Altshuler, “The focusing of electron flow and a veselago lens in graphene p-n junctions”, Science **315**, 1252–1255 (2007).

[150] J. Cserti, A. Pályi, and C. Péterfalvi, “Caustics due to a negative refractive index in circular graphene p-n junctions”, Phys. Rev. Lett. **99**, `10.1103/physrevlett.99.246801` (2007).

[151] Y. Kravtsov and Y. Orlov, *Geometrical optics of inhomogeneous media*, Springer Series on Wave Phenomena (Springer Berlin, Heidelberg, 1990).

[152] H. J. Maris, “Enhancement of heat pulses in crystals due to elastic anisotropy”, The Journal of the Acoustical Society of America **50**, 812–818 (1971).

[153] G. A. Northrop and J. P. Wolfe, “Ballistic phonon imaging in germanium”, Phys. Rev. B **22**, 6196–6212 (1980).

[154] W. Eisenmenger and A. Kaplianskii, *Nonequilibrium phonons in nonmetallic crystals*, Modern problems in condensed matter sciences (North-Holland, 1986).

[155] V. Vlaminck, L. Temdie, V. Castel, M. B. Jungfleisch, D. Stoeffler, Y. Henry, and M. Bailleul, “Spin wave diffraction model for perpendicularly magnetized films”, J. Appl. Phys. **133**, `10.1063/5.0128666` (2023).

[156] E. Jakubisova-Liskova, S. Visnovsky, H. Chang, and M. Wu, “Optical spectroscopy of sputtered nanometer-thick yttrium iron garnet films”, J. Appl. Phys. **117**, `10.1063/1.4906526` (2015).

[157] H. J. Eichler and J. Eichler, *Laser: bauformen, strahlführung, anwendungen* (Springer Berlin Heidelberg, 2015).

[158] F. B. Mushenok, R. Dost, C. S. Davies, D. A. Allwood, B. J. Inkson, G. Hrkac, and V. V. Kruglyak, “Broadband conversion of microwaves into propagating spin waves in patterned magnetic structures”, Appl. Phys. Lett. **111**, `10.1063/1.4995991` (2017).

[159] F. Goedsche, “Reflection and refraction of spin waves”, Phys. Status Solidi B **39**, `10.1002/pssb.19700390143` (1970).

[160] W. Yu, J. Lan, R. Wu, and J. Xiao, “Magnetic snell’s law and spin-wave fiber with dzyaloshinskii-moriya interaction”, Phys. Rev. B **94**, `10.1103/physrevb.94.140410` (2016).

[161] Y. I. Gorobets and S. A. Reshetnyak, “Reflection and refraction of spin waves in uniaxial magnets in the geometrical-optics approximation”, Tech. Phys. **43**, 188–191 (1998).

[162] D.-E. Jeong, D.-S. Han, and S.-K. Kim, “Refractive index and snell’s law for dipole-exchange spin waves in restricted geometry”, SPIN **01**, 27–31 (2011).

[163] R. Gieniusz, V. D. Bessonov, U. Guzowska, A. I. Stognii, and A. Maziewski, “An antidot array as an edge for total non-reflection of spin waves in yttrium iron garnet films”, Appl. Phys. Lett. **104**, `10.1063/1.4867026` (2014).

[164] J. Stigloher et al., “Snell’s law for spin waves”, Phys. Rev. Lett. **117**, `10.1103/physrevlett.117.037204` (2016).

[165] S.-K. Kim, S. Choi, K.-S. Lee, D.-S. Han, D.-E. Jung, and Y.-S. Choi, “Negative refraction of dipole-exchange spin waves through a magnetic twin interface in restricted geometry”, Appl. Phys. Lett. **92**, `10.1063/1.2936294` (2008).

[166] S. A. Reshetnyak, “Refraction of surface spin waves in spatially inhomogeneous ferrodielectrics with biaxial magnetic anisotropy”, Phys. Solid State **46**, 1061–1067 (2004).

[167] P. Gruszecki, J. Romero-Vivas, Y. S. Dadoenkova, N. N. Dadoenkova, I. L. Lyubchanskii, and M. Krawczyk, “Goos-hänchen effect and bending of spin wave beams in thin magnetic films”, Appl. Phys. Lett. **105**, `10.1063/1.4904342` (2014).

[168] P. Gruszecki, Y. S. Dadoenkova, N. N. Dadoenkova, I. L. Lyubchanskii, J. Romero-Vivas, K. Y. Guslienko, and M. Krawczyk, “Influence of magnetic surface anisotropy on spin wave reflection from the edge of ferromagnetic film”, Phys. Rev. B **92**, `10.1103/physrevb.92.054427` (2015).

[169] P. Gruszecki, M. Mailyan, O. Gorobets, and M. Krawczyk, “Goos-hänchen shift of a spin-wave beam transmitted through anisotropic interface between two ferromagnets”, Phys. Rev. B **95**, `10.1103/physrevb.95.014421` (2017).

[170] P. Gruszecki, K. Y. Guslienko, I. L. Lyubchanskii, and M. Krawczyk, “Inelastic spin-wave beam scattering by edge-localized spin waves in a ferromagnetic thin film”, Phys. Rev. Applied **17**, `10.1103/physrevapplied.17.044038` (2022).

[171] P. Gruszecki, M. Kasprzak, A. E. Serebryannikov, M. Krawczyk, and W. Śmigaj, “Microwave excitation of spin wave beams in thin ferromagnetic films”, Sci. Rep. **6**, `10.1038/srep22367` (2016).

[172] H. S. Körner, J. Stigloher, and C. H. Back, “Excitation and tailoring of diffractive spin-wave beams in nife using nonuniform microwave antennas”, Phys. Rev. B **96**, `10.1103/physrevb.96.100401` (2017).

[173] L. Temdie, V. Castel, V. Vlaminck, M. Jungfleisch, R. Bernard, H. Majjad, D. Stoeffler, Y. Henry, and M. Bailleul, “Probing spin wave diffraction patterns of curved antennas”, Phys. Rev. Applied **21**, `10.1103/physrevapplied.21.014032` (2024).

[174] L. Temdie, V. Castel, C. Dubs, G. Pradhan, J. Solano, H. Majjad, R. Bernard, Y. Henry, M. Bailleul, and V. Vlaminck, “High wave vector non-reciprocal spin wave beams”, AIP Adv. **13**, `10.1063/9.0000535` (2023).

[175] A. Martyshkin, S. Sheshukova, F. Ogrin, E. Lock, D. Romanenko, S. Nikitov, and A. Sadovnikov, “Nonreciprocal spin-wave beam transport in a metallized t-shaped magnonic junction”, Phys. Rev. Applied **22**, `10.1103/physrevapplied.22.014037` (2024).

[176] F. Vilsmeier, C. Riedel, and C. H. Back, “Spatial control of hybridization-induced spin-wave transmission stop band”, Appl. Phys. Lett. **124**, `10.1063/5.0188193` (2024).

[177] K. Artmann, “Berechnung der seitenversetzung des totalreflektierten strahles”, Ann. Phys. (Berlin) **437**, 87–102 (1948).

[178] H. K. V. Lotsch, “Reflection and refraction of a beam of light at a plane interface”, Journal of the Optical Society of America **58**, 551 (1968).

[179] K. Y. Bliokh and A. Aiello, “Goos–hänchen and imbert–fedorov beam shifts: an overview”, Journal of Optics **15**, 014001 (2013).

[180] J. Stigloher, T. Taniguchi, H. S. Körner, M. Decker, T. Moriyama, T. Ono, and C. H. Back, “Observation of a goos-hänchen-like phase shift for magnetostatic spin waves”, Phys. Rev. Lett. **121**, `10.1103/physrevlett.121.137201` (2018).

[181] B. Lenk, H. Ulrichs, F. Garbs, and M. Münzenberg, "The building blocks of magnonics", Phys. Rep. **507**, 107–136 (2011).

[182] J. Jorzick, S. O. Demokritov, B. Hillebrands, M. Bailleul, C. Fermon, K. Y. Guslienko, A. N. Slavin, D. V. Berkov, and N. L. Gorn, "Spin wave wells in nonellipsoidal micrometer size magnetic elements", Phys. Rev. Lett. **88**, `10.1103/physrevlett.88.047204` (2002).

[183] J. Topp, J. Podbielski, D. Heitmann, and D. Grundler, "Internal spin-wave confinement in magnetic nanowires due to zig-zag shaped magnetization", Phys. Rev. B **78**, `10.1103/physrevb.78.024431` (2008).

[184] V. E. Demidov, S. O. Demokritov, K. Rott, P. Krzysteczko, and G. Reiss, "Mode interference and periodic self-focusing of spin waves in permalloy microstripes", Phys. Rev. B **77**, `10.1103/physrevb.77.064406` (2008).

[185] X. Xing, Y. Yu, S. Li, and X. Huang, "How do spin waves pass through a bend?", Sci. Rep. **3**, `10.1038/srep02958` (2013).

[186] A. V. Chumak, A. A. Serga, B. Hillebrands, and M. P. Kostylev, "Scattering of backward spin waves in a one-dimensional magnonic crystal", Appl. Phys. Lett. **93**, `10.1063/1.2963027` (2008).

[187] K.-S. Lee, D.-S. Han, and S.-K. Kim, "Physical origin and generic control of magnonic band gaps of dipole-exchange spin waves in width-modulated nanostrip waveguides", Phys. Rev. Lett. **102**, `10.1103/physrevlett.102.127202` (2009).

[188] S.-K. Kim, K.-S. Lee, and D.-S. Han, "A gigahertz-range spin-wave filter composed of width-modulated nanostrip magnonic-crystal waveguides", Appl. Phys. Lett. **95**, `10.1063/1.3186782` (2009).

[189] M. Iwaba and K. Sekiguchi, "Spin-wave enhancement using feedback-ring structure", Jpn. J. Appl. Phys. **62**, 103001 (2023).

[190] D. G. Rabus, *Integrated ring resonators* (Springer Berlin Heidelberg, 2007).

[191] J. Canny, "A computational approach to edge detection", IEEE_J_PAMI **PAMI-8**, 679–698 (1986).

[192] D. Marr and E. Hildreth, "Theory of edge detection", Proceedings of the Royal Society of London. Series B. Biological Sciences **207**, 187–217 (1980).

[193] R. Gonzalez and R. Woods, *Digital image processing*, Addison-Wesley world student series (Pearson, 2017).

List of Abbreviations

BLS	Brillouin light scattering
BV	Backward-Volume
CPW	Coplanar waveguide
CSWB	Caustic spin wave beam
CW	Continuous wave
DE	Damon-Eshbach
DMI	Dzyaloshinskii–Moriya interaction
FEM	Finite-element method
FMR	Ferromagnetic resonance
FT	Fourier-transformed
FV	Forward-Volume
GH	Goos-Hänchen
GGG	Gadolinium gallium garnet
KS	Kalinikos and Slavin
LLG	Landau-Lifshitz-Gilbert
LoG	Laplacian of Gaussian
MOKE	Magneto-optical Kerr effect
PSSW	Perpendicular standing spin waves
SNS-MOKE	Super-Nyquist sampling MOKE
SW	Spin wave
TR-MOKE	Time-resolved magneto-optical Kerr effect
VNA	Vector Network Analyzer
YIG	Yttrium ion garnet

List of Publications

Main Publications

F. Vilsmeier, C.Riedel, and C. H. Back, ”Spatial control of hybridization-induced spin-wave transmission stop band”, Appl. Phys. Lett. **124**, 10.1063/5.0188193 (2024).

A. Wartelle, **F. Vilsmeier**, T. Taniguchi, and C. H. Back, ”Caustic spin wave beams in soft thin films: properties and classification”, Phys. Rev. B. **107**, 10.1103/physrevb.107.144431 (2023).

Contributions to Publications and Preprints

T. Taniguchi, J. Sahliger, **F. Vilsmeier**, and C. H. Back, ”Width-mode order dependent spin wave conversion in an in-plane magnetized microscale T-shaped YIG magnonic splitter”, J. Appl. Phys. **135**, 10.1063/5.0218351 (2024).

C. Lüthi, L. Colombo, **F. Vilsmeier**, and C. H. Back, ”Comparative analysis of spin wave imaging using nitrogen vacancy centers and time resolved magneto-optical measurements”, arXiv:2405.02014 (2024).

Manuscript in Preparation

F. Vilsmeier, T. Taniguchi, M. Lindner, and C. H. Back, ”Spin wave propagation in a ring-shaped magnonic waveguide”.

Acknowledgements

In the most important chapter of this thesis, I want to express my gratitude to the following persons:

First of all, I want to thank my supervisor, Prof. Dr. Christian Back, for giving me the chance to do my PhD in his group. I truly appreciated the open and friendly environment he created, where conversations could easily shift from research to topics like basketball and biking. Thank you for all the support and the opportunities you've provided!
I also want to thank Dr. Christian Riedel for his invaluable help and input, both in the lab and beyond. From proof-reading to fruitful scientific discussions and guidance, your support was instrumental in shaping this thesis. The pricey investment in a bottle of wine is not forgotten. I hope the world will appreciate it.
I would like to thank Dr. Alexis Wartelle for his valuable discussions and explanations, particularly regarding spin wave caustics. His support, along with the development of the simulation code and model for caustics, was essential to the progress of this work.
I want to say "Dankeschön" to Dr. Takuya Taniguchi for all his help, insightful discussions, and everything I've learned from him—including how to roll sushi properly.
A special thank you to my office mate, Dr. Thomas Meier, for his constant help and for creating such a comfortable and enjoyable atmosphere. From invaluable lab support and discussions to many memorable "Mhmh" moments, I've learned a lot and truly enjoyed and appreciated it all.
I would also like to thank my brother Johannes (and Okabe-Ito) for his input on color-blind-friendly color palettes and his help with proof-reading.
Lastly, a big thank you to all the current and former members of the chair for making the working atmosphere so enjoyable. It was, indeed, maxiiiiiiiiiiimal fun.